Centennial-millennial scale variations in West Antarctic Ice Sheet discharge and their relationship to climate and ocean changes during the late Holocene

by

Frida Snilstveit Hoem

MASTER THESIS IN GEOLOGY
Field of study: Marine geology and paleoclimate

Department of Earth Science

University of Bergen

June 2017

Abstract

The West Antarctic Ice Sheet (WAIS) may be highly sensitive to future warming and to ocean driven changes in subsurface melting. Understanding this sensitivity is critical as WAIS dynamics are a major source of uncertainty in sea level rise and regional climate projections. Although there is increasing evidence that WAIS discharge has varied on centennial to multi-millennial timescales since the last glacial period, little is known about its most recent (late Holocene) behavior. This period is particularly important as a baseline for delineating natural and anthropogenic driving forces and to understand coupling between climate, ocean circulation, and WAIS discharge.

Here we present high-resolution records of WAIS discharge together with co-registered signals of surface and deep ocean physical property changes in a multicore taken from the southern flank of the North Scotia Sea Ridge (53° 31.813 S; 44° 42.143 W at 2750m water depth) spanning the past 4200 years. The site is situated just south-east of the polar front beyond the reach of seasonal sea ice, confining any occurrence of ice-rafted debris (IRD) to iceberg sources, mostly originating from WAIS. The IRD record from core GS08-151-02MC provides centennially resolved record of iceberg supply from which we infer WAIS dynamics and variability. Oxygen and carbon isotopic composition of benthic (*U. peregrina)* and planktic (*N. pachyderma* (s)) foraminifera give (regional) information on past polar deep water and surface water temperatures, circulation and nutrients. The local surface water hydrography appears relatively stable over the past 4200 years with the planktic $\delta^{18}O$ signal indicating centennial-millennial scale changes of typically ≤1°C (Δ0.22‰) and notably smaller in amplitude than the regional warming observed over the past century. The lack of correlation between surface water physical properties and IRD in the downcore records, suggests that IRD does not reflect iceberg survival, but rather changes in the supply (WAIS dynamics) or routing. Consistent with this interpretation, IRD covaries with climate on the Antarctic Peninsula (from James Ross Island ice core) over the past 4200 years with cooler conditions and lower amounts of IRD over much of the past two millennia, and both records indicate a recovery with warming and increased IRD prior to industrialization. This relationship is consistent with the hypothesis that climate and specifically ocean temperatures and circulation were important for modulating the WAIS discharge rates over the past few millennia.

Acknowledgments

First of all I would like to tribute my gratitude to my main supervisor Ulysses Ninnemann for being the main source for guidance, assistance and discussion. Throughout this process, Ule has enthusiastically shared his knowledge, especially in paleoclimate, paleoceanography and the importance of critical thinking. I am also immensely thankful to co-supervisors Helga (Kikki) Kleiven and Nil Irvali. I thank Kikki for her wealth of knowledge and being a true role model when it comes to being passionate about science and sharing it to the public and Nil for her kindness and expertise in microfossils with great tips and tricks which greatly aided the foraminiferal picking process.

Great gratitude is also directed to University of Bergen, the Bjerknes Centre for Climate Research and the "Paleoceanographic and climatic variability on decadal to millennial timescales across the Drake Passage" (PALEODRAKE) project for financing laboratory- and fieldwork. I also thank the officers, crew, and scientists aboard the IPY PALEODRAKE cruise for their hard work at sea.

A very special thank you goes to Rune Egil Søraas for technical support in the stable isotope laboratory, FARLAB. He was a true joy to work with, always positive and smiling. Furthermore, I would like to thank Willem van der Bilt for interesting discussions and supplementary data, and Eirik Vinje Galaasen for lessons in the Ocean Data View program.

I also thank my supervisors for the opportunity to attend the EGU conference in Vienna in April 2017, and to Sunniva Rutledal for great company. At the EGU conference, I got to present my work and receive feedback from a broad scientific audience. The interesting presentations and reflective discussions with fellow students and scientists was very inspiring and motivational to go on in academia.

Finally yet importantly, thanks are given to my fellow students and friends at the Department of Earth Science, who have made the five years of studying so fun, educational and memorable. Big appreciations must also be awarded to my family for unconditional support and motivation.

Bergen, 1. June 2017

Frida Snilstveit Hoem

Contents

1 Introduction

This thesis has been supervised by Professor Dr. Ulysses S. Ninnemann, Associate Professor Dr. Helga (Kikki) F. Kleiven and Researcher Dr. Nil Irvali from the Department of Earth Science and Bjerknes Centre for Climate Research (BCCR) at the University of Bergen (UoB).

1.1 Project

This study is a follow up of the International Polar Year (IPY). The IPY-year (2007-2008) aimed to bring together the world to accelerate a wide range of physical, biological and social research topics with full and equal coverage of both the Arctic and the Antarctic regions. The broader goal was to strengthen the polar research, which is expensive and challenging. The coordinated international effort represented by the IPY produce results that are several times as valuable as the individual contributions of the nations involved. One of the Norwegian contributions to the IPY is the "Paleoceanographic and climatic variability on decadal to millennial timescales across the Drake Passage" (PALEODRAKE) project. The PALEODRAKE project was funded by the IPY and the Norwegian Research Council and was a logistic "add-on" to the Institute of Marine Research's wide-ranging research cruise with the Norwegian *R/V G.O. Sars* to the Southern Ocean (Drake Passage) in 2008 (January-March). The primary objective for the PALEODRAKE project was to reconstruct the magnitude and expression of natural climate variability in the region of the Drake Passage and Scotia Sea in order to better understand the coupling between climate, Antarctic water mass properties, and circumpolar circulation on decadal to millennial timescales.

1.2 Motivation

The historical observational period is too short to assess the nature and impact of changes in ocean circulation and properties associated with climate perturbations in the past. The available records from the Southern Ocean illustrate the potential for reconstructing past changes in ocean circulation, Antarctic ice and climate but few provide high resolution

evidence of recent conditions and variability just prior to anthropogenic warming. Centennial scale records from the late Holocene are necessary in order to define the baseline natural variability in the climate, ocean and ice systems. Not only will this provide the basis for delineating anthropogenic from natural variability, but it will also provide insights into the coupling between climate, ocean circulation, and ice sheet variability.

The Antarctic ice sheet discharge and its relationship to climate and ocean circulation is crucially important for several reasons. The largest uncertainty in future projections for sea level rise, arises from the dynamics of the West Antarctic ice sheet. In addition to sea level, the West Antarctic ice sheet decay could have other far ranging impacts on, for example, sea-ice growth and its effect on the albedo, global deep-ocean ventilation, and the evolution of Southern Ocean ecosystem and carbon sequestration. Yet, relatively little is known about the interactions between wind, ocean, and ice and the driving mechanism behind past natural variability in these systems. Antarctica has warmed significantly over the past 50 years, with the Antarctic Peninsula and parts of west Antarctica displaying the most rapid temperature increases in the Southern Hemisphere.

This thesis aims to improve our understanding of climate - ocean - ice sheet linkages during the past four and a half millennia; providing crucial context for better understanding ongoing changes in the region as well as inter-hemispheric linkages and potential future changes and their impacts.

Specifically, the objectives of this thesis are to:

- Reconstruct iceberg activity (IRD) to monitor centennial to millennial ice-sheet dynamics and variability over the past ~4200 years
- Reconstruct surface and deep ocean physical properties (Temperature and salinity, using $\delta^{18}O$ of planktic and benthic foraminifera) to resolve any climate variability and establish the regional baseline of natural variability.
- Evaluate potential forcing mechanisms for iceberg activity and ice sheet dynamics by comparing IRD records to in situ and regional climate records.

2 Background

Climate change research is a multidisciplinary field which has gained increased popularity and recognition over the recent decades. Studying paleoclimate records, meaning the study of changes in climate spanning the scale of Earth's history, is of great importance as it allows us to obtain a better understanding of the various drivers, mechanisms and patterns of past climate variability. Paleoclimate archives help contributes to elucidate the underlying dynamics in the climate systems and possibly predict rapid climate changes in the future. Building an understanding of the rate and scale of natural climate variability also provides a context for identifying any climate changes that are outside of, in scale or character, to the natural climate variability and thus may be attributed to anthropogenic (man-made) influences.

Paleoceanography is the study of the past history of ocean circulation, temperature, salinity, density, productivity, and chemical variations. A central research goal in Paleoceanography is to interpret the role of the ocean processes in climate change and for the global environment in the past, present and future. Clues about the interior circulation of the ocean are provided by distribution of water masses, each defined by a set of physical and biochemical properties, such as temperature, salinity, dissolved oxygen and nutrient concentration. The water mass properties are formed in the surface mixed layer where they are determined through the exchange of heat, moisture and dissolved gases with the atmosphere and/or ice, as well as biogeochemical processes (Williams & Follows, 2011). Valuable information of water mass properties is preserved in the form of microfossil assemblages, organic matter, and the elemental and isotopic composition in calcareous shells and sediments. Marine sediments can also provide information about climate. Whereas continental depositional environments are often affected by local or regional factors (e.g. Biological, chemical and mechanical weathering), marine sediment records from the open ocean tend to be representative for conditions over large spatial scales and in some cases have the ability to monitor basin to global scale circulations systems. In addition, ocean deposits are nearly continuous, with a robust age stratigraphy that spans almost 170 million years of Earth's history (Wefer et al., 1999). For example, detailed lithological and stratigraphic studies have made it possible to correlate ice-rafted sediment layers to glaciations of the Northern and Southern Hemispheres (Hodell et al.,

2001; Hodell et al., 2010). Furthermore, the paleoceanographic research community has gained insight into ocean behavior on timescales ranging from tectonic (million of years) to decadal (El Nino) through for instance coring by the International Ocean Discovery Program (IODP) (e.g Tiedemann et al., 1994). However, there is a miss balance between the sampling of the Northern versus the Southern Hemisphere (SH), the latter being due to difficult logistics and costly expedition planning. The IPY-year (2007-2008) brought together the research world to accelerate the research in high latitudes. The new high-resolution proxy records of GS08-151-02MC, which was cored during the Norwegian IPY PALEODRAKE expedition, aims to further quantify climate variability and resolve its impact on the (West) Antarctic ice sheet, contributing as a piece to the big puzzle unravelling the climate dynamics in the Southern polar region.

2.1 The global climate system

The Earth's climate system consists of the atmosphere, hydrosphere, cryosphere, biosphere and the land surface. These five components constantly interact with each other on different time scales. Each component exhibit different response times and changes may be annual, seasonal or take thousands to millions of years, resulting in a highly complex system. The atmosphere is the fastest responder in the climate system, whilst the deep ocean and ice sheets are the slowest responders, aside from solid earth and tectonic changes, and may lag behind the climate forcing (W. F. Ruddiman, 2008). Climate is the large-scale and long term average of weather conditions, such as temperature and precipitation, wind, atmospheric pressure, etc., measured over decades (normally ≥30 years) for a particular area (Cronin, 2009).

Several external and internal factors cause and drive changes in the climate system. The big drivers are tectonic processes, changes in the Earth's orbit around the sun and variability in the strength of the sun. Anthropogenic forcing induced by human activities can also be viewed as a contributor. These *forcings* will cause a *response* in the climate system where changing interactions between the different components can lead to positive or negative feedbacks. Positive feedbacks are processes that amplify the initial change, while negative feedbacks suppress the initial change (Ruddiman, 2008).

Evidence from climate archives suggest that variation in incoming insolation due to orbital cycles, the so-called Milankovitch theory, is the main mechanism that drives the waxing and waning of ice sheets (Hays et al., 1976; Tiedemann et al., 1994). The global ocean circulation is an important component of the climatic system, and Broecker and Denton (1989) proposed that the Quarternary glacial-interglacial cycles were dominated by abrupt reorganization of the ocean - atmosphere system, since the orbital forcing alone is not sufficient to account for the observed temperature and ice-extent response and climatic changes on shorter time scale.

2.1.1 Global thermohaline ocean circulation

The exchange of warm surface water and cold deep water on the planet is carried out by the enormous ocean conveyor belt system called the thermohaline (overturning) circulation (THC) (Figure 2.1). This strong contributor to the heat budget of the Earth is driven by fluxes of heat (thermo) and freshwater (haline) across the sea surface. In effect, warm, saline surface water flows into high latitudes of the Northern Hemisphere (NH) where it cools and sinks to depth. These bottom waters then flow southward at depth through the Atlantic Ocean, until they reach the Southern Ocean where they mix with the rest of the world`s ocean waters.

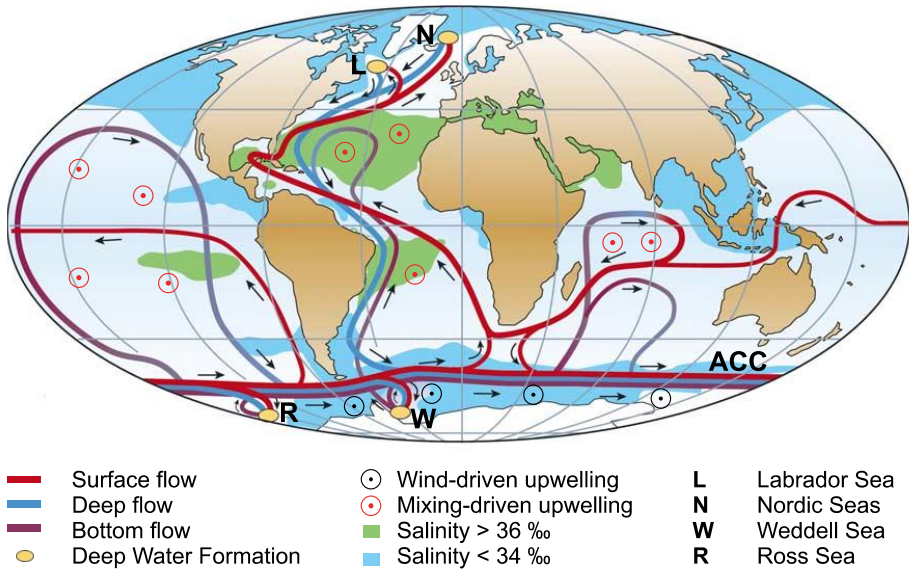

Figure 2.1: Simplified sketch of the global thermohaline circulation system. Modified after (Rahmstorf, 2006)

Using paleoceanographic evidence, Broecker and Denton (1989) suggested that the THC might undergo abrupt changes and played a key role in triggering the large and abrupt global climate changes that punctuated the last period of glaciation. Evaporation, precipitation, sea-ice formation and glacial melting all control the density of sea water, which in turn drive the THC (Kuhlbrodt et al., 2007). Ocean-atmosphere coupled models with forced CO_2 levels, similar to those we may face towards the end of the century, show a drastic weakening of the THC due to freshening of seawater in the high latitudes (Manabe & Stouffer, 1997). The response in the Southern Hemisphere to the slowdown of the THC, known as the bipolar seesaw (Broecker, 1998), is much smaller than observed in the Northern Hemisphere. Generally there is a small warming in the Southern Hemisphere (Stocker & Wright, 1991). However, the origin of thermohaline instability itself has not yet been established. Thus the ultimate global climate effects of THC variability are not known for certain and these questions are at the heart of understanding abrupt climate variability.

2.1.2 Global climate of the mid to late Holocene

The global climate of the mid to late Holocene has been relatively stable when compared to the large-scale changes occurring between glacial and interglacial periods. However, Holocene records from both hemispheres exhibit long-term orbital climate trends. Denton and Karlén (1973) correlated atmospheric C^{14} variations measured from tree rings with Holocene glacier and tree-line fluctuations over the last 7000 yr. Their results showed a pattern with early-mid Holocene peak and glacier contractions around 6000 yr BP, known as the hypsithermal, followed by cooling and glacier expansion, neoglaciation, between 5800-4900 and 3300-2400 yr BP, and again glacier recession 2400-1250 and 1050-460 yr BP. Hodell's (2001) record of abrupt cooling of Antarctic surface waters, and sea ice expansion in the South Atlantic Sector of the Southern Ocean at 5000 yr BP, is consistent with the cooler neoglaciation peaking at 2500 yr BP.

Superimposed on long term orbital trends there is higher frequency variability on a range of timescales from millennial to decadal. The largest of these climatic perturbation in the Holocene is known as the 8.2 kyr event, with weakened overturning circulation forced by a large freshwater outburst to the North Atlantic Ocean (Ellison et al., 2006; Kleiven et al.,

2008). The Little Ice Age (LIA), lasting from about 650 – 150 yr BP, was the latest of a series of centennial scale oscillations in the climate (Wanner et al., 2008). The LIA is thought to be driven by lower summer insolation in the NH, due to orbital forcing, coincided with solar insolation minima and several strong tropical volcanic eruptions (Mann et al., 2009). There remains controversy about changes in the ocean heat transport during the LIA at high northern latitudes, and possible additional implications for climates of the Southern Hemisphere (Wanner et al., 2008). Broecker (2000) argues for a bipolar seesaw -type redistribution of heat between the hemispheres during the LIA, while Orsi et al., (2012) argues against this based on evidence of cooling from ice core record at West Antarctic Ice Sheet (WAIS) divide. However, one location is insufficient to determine the hemispheric response and the role of the bipolar seesaw (THC) in the LIA remains equivocal due to a paucity of Southern Hemisphere climate records spanning the LIA.

2.2 Regional climate

The Southern Ocean is a relatively "unexplored" part of the global ocean and not well understood. The lack of instrumental data from the Southern Ocean, especially prior to the 1950s, limits our understanding of climate changes in this region. Thus, paleoclimate reconstructions from the ocean and the ice sheets provide valuable insight into the Southern Hemisphere climate and ocean variability. The Southern Ocean represents the most important junction in the global ocean circulation system (Figure 2.2) mixing all three northern-source deep water from Indian, Pacific and Atlantic oceans (IDW, PDW, NADW) that move southward and upwell in the Southern Ocean, and controlling the exchange of nutrients, salt and heat in the worlds oceans. The Antarctic Circumpolar Current (ACC), the largest current system in the world, transports around 110-144 Sv (1 Sv = 10^6 m^3 s^{-1}) of water eastward around the Antarctic continent (Grose et al., 1995); connecting the Atlantic, the Indian and the Pacific Ocean.

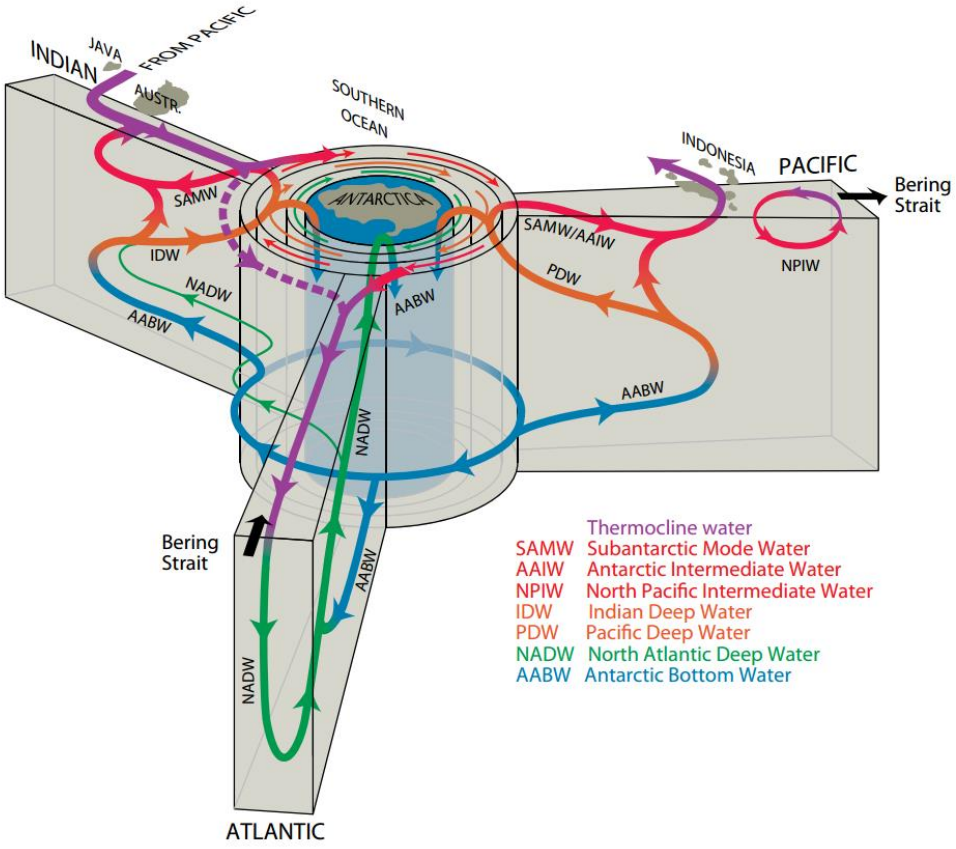

Figure 2.2: Schematic of the overturning circulation from a Southern Ocean perspective, revised from Talley (2011).

The opening of Drake Passage, at or near the Eocene-Oligocene boundary (~34 MA ago), established the full circumpolar oceanic flow around the Antarctic continent and led to changes in global circulation and climate, and the rapid expansion of the Antarctic ice sheet (Kennett, 1977). The ACC is essentially driven by the strong southern westerly winds (SWW) that result from the pressure gradient at the Earth's surface between the subtropical high pressure and low pressure at 60-65°S, which forces air to move eastwards under the influence of the Coriolis effect (Rintoul et al., 2001). The Southern Hemisphere Annular Mode (SAM), the changing position of the SWW belt, is the primary pattern of climate variability in the Southern Hemisphere (Marshall, 2003). During positive phase of SAM, atmospheric pressures over Antarctica are relatively low compared to the mid-latitudes, making the SWW band contract towards Antarctica (Figure 2.3).

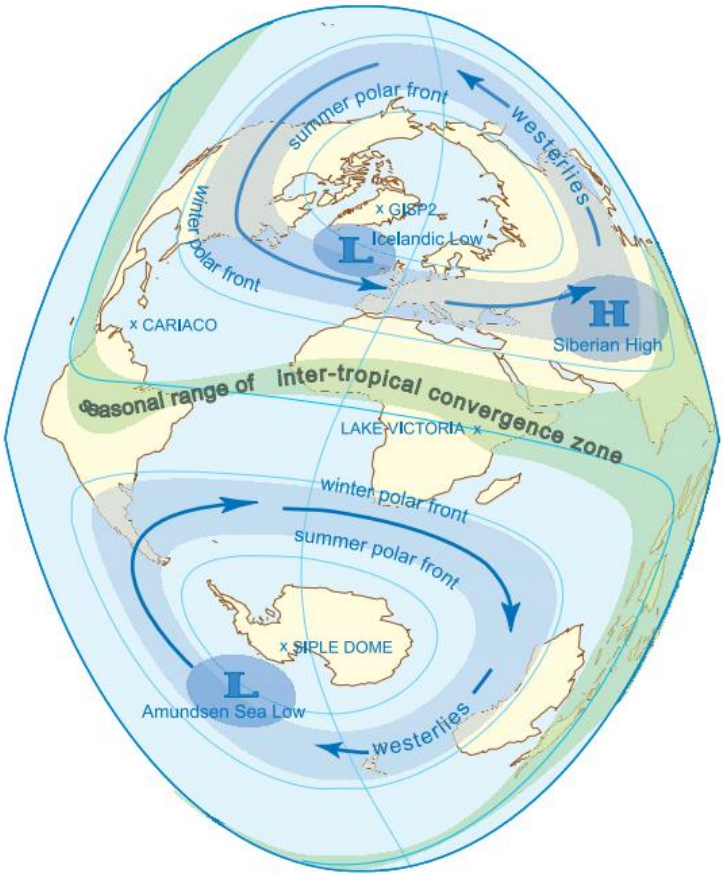

Figure 2.3 Northern and Southern Hemisphere atmospheric circulation (Wanner et al., 2008)

The SAM influences upwelling of deep water around Antarctica. If the westerlies are situated far away from Antarctica (negative SAM), they are poorly aligned with the ACC and less upwelling of deep water will take place; hence less CO_2 will degas to the atmosphere. When the westerlies (positive SAM) are positioned close to the pole, more upwelling and CO_2 degassing will occur because the winds are better aligned with the ACC (Toggweiler et al., 2006).

The Southern Ocean is also a significant sink for atmospheric carbon and important to the global carbon cycle, contributing ~10% of the ocean's total carbon sequestration through a mixture of chemical and biologically driven processes (Ciais et al., 2013).

The most important greenhouse gases in Earth´s atmosphere are water vapor and carbon dioxide. The burning of fossil fuels has led to increased emissions of CO_2 in the past few centuries, and as a consequence the atmospheric CO_2 level have increased from 280 ppm in preindustrial times to 407 ppm today (NOAA, 2017). The SWW driven upwelling of

deep water in the Southern Ocean around Antarctica helps regulate the exchange of CO_2 between the deep sea and the atmosphere. Research have shown that atmospheric CO_2 closely follows the rise in east Antarctic temperatures indicating that changes in the Southern Ocean potentially controls deglacial CO_2 release (Monnin et al., 2001).

2.2.1 Regional climate of the mid to late Holocene

Sediment cores from the Atlantic sector of the Southern Ocean show warm and ice free Holocene conditions (at ~50°S) until around 6000-5000 yr BP (Hodell et al., 2001), coincident with the timing of a mid-Holocene climatic optimum (hypsithermal) documented in palaeoclimate records from the Antarctic continent and Palmer Deep (Masson et al., 2000; Domack et al., 2001). The mid Holocene warm period was followed by a marine neoglacial cool period that lasted at least until ~2000 yr BP, with evidence for extended winter sea ice cover, glacial expansion and increased IRD. The late Holocene exhibit warming with sea ice retreat in the Atlantic sector (Nielsen et al., 2004). The marine-inferred mid-Holocene climate optimum is out of phase with some of the ice core and terrestrial records suggesting a regional heteregeoneity in climate evolution (Hodell et al., 2001).

The El Niño Southern Oscillation (ENSO) is a phenomenon impacting temperatures and upwelling along the South American west coast and the strength of the Walker Circulation i.e. the large-scale atmospheric circulation over the Pacific Ocean driven by the temperature contrast between the west and the east Pacific. This influences nearly the whole SH and the last 5000 years have been characterized by increased ENSO activity (Wanner et al., 2008). Interannual rainfall variability, in central Chile and possibly South Georgia, is strongly related to ENSO (Lamy et al., 2001).

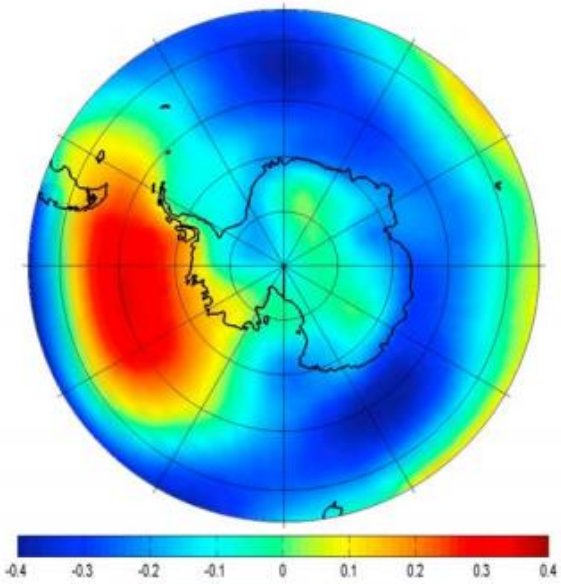

Figure 2.3: shows the loading pattern of the El Niño –Southern Oscillation phenomenon over Antarctica and the Southern Ocean, defined as the correlation of the Southern Oscillation Index with surface atmospheric pressure (Mayewski et al., 2008).

The opposing climate east and west of the Antarctic Peninsula, commonly referred to as the Antarctic dipole (Figure 2.3), could be explained by the late Holocene maximum in El Niño events. This teleconnection between Antarctica and Southern Hemisphere variability (ENSO) have been shown in atmospheric and oceanic parameters (temperature, sea-level pressure, and sea-ice extent) (e.g Smith& Stearns et al., 1993).

2.2.2 Recent climate change in the region

Today the warming of the cold glaciated Antarctica is slower then the warming over the equator, leading to a higher heat gradient and consequently there has been a significant trend toward the positive phase of the SAM in recent decades (Abram et al., 2014). The trend towards high positive SAM is suggested by modelling studies to be predominantly a response to anthropogenic forcing, such as the increase in greenhouse gases and more importantly the development of the Antarctic stratospheric ozone hole (Thompson et al., 2011), resulting in increased westerlies closer to Antarctica (Marshall et al., 2006). The Southern Ocean, and in particular the ACC which has migrated southward, has warmed more rapidly than the global ocean over recent decades implying that this region may be especially sensitive to climate perturbation (Gille, 2008). The implications that this warming and contraction of SWW have on climate is amongst other reduction of CO_2 sink

in the Southern Ocean (Mayewski et al., 2009), ozone depletion over the Antarctic continent, subsurface melting of ice sheets, accelerated ice sheet flow and sea level rise.

In the period of instrumental records (the last 50 years) has the Antarctic Peninsula warmed by 2.94°C, which is significantly more than the global average of 0.52°C (based on the Goddard Institute for Space Studies data from Hansen (2010)). The temperatures are now the highest for 1800 years (Mulvaney et al., 2012). The largest warming trends occur on the western and northern parts of the Antarctic Peninsula (Turner et al., 2009). Based on data from satellites and automated weather stations, West Antarctica has warmed by about 0.1°C/decade, especially in winter and spring. Ice core data from the Siple Dome suggest that this warming began around 1800 AD (Turner et al., 2009).

2.3 The West Antarctic ice sheet

The Antarctic ice sheet covering an area of 13.6 × 106 km^2 (Drewry, 1983) with a mass of 25.4 × 10^6 km^3, account for about 90% of the global ice volume(Lythe & Vaughan, 2001). The Antarctic Ice Sheet represents the largest potential source of future sea-level rise: if all of its ice melted, sea level would rise by about 60 m (Vaughan et al., 2013).
Extensive satellite monitoring began in the 1990s and, within a decade, evidence emerged that the ice sheet had already started to speed up, retreat and destabilize. NASA's Ice, Cloud and land Elevation (ICESat) mission revealed major mass loss from Antarctica's ice shelves (Pritchard et al., 2012) and grounded ice sheet (Shepherd et al., 2012) by estimating the change in ice height with time and converting that to mass. This Ice Sheet Mass Balance Exercise (IMBIE; Shepherd et al. (2012)) showed mass loss from the Antarctic Ice Sheet of 1350 Gt (gigatonnes) of ice between 1992 and 2011 (1 Gt = 1000 million tonnes), equivalent to an increase in sea level of 3.75 mm or 0.00375 m. The loss over this period (1992-2011) is mainly due to increased ice discharge into the ocean in two rapidly changing regions: West Antarctica (–65 ± 26 Gt per year) and the Antarctic Peninsula : (–20 ± 14 Gt per year)(Shepherd et al., 2012) (Figure 2.4 b). It is also worth noting that mass losses in the Northern Peninsula are caused by ongoing acceleration, not by a change in snowfall because snowfall increased in 1980–2004. (Rignot et al., 2008)

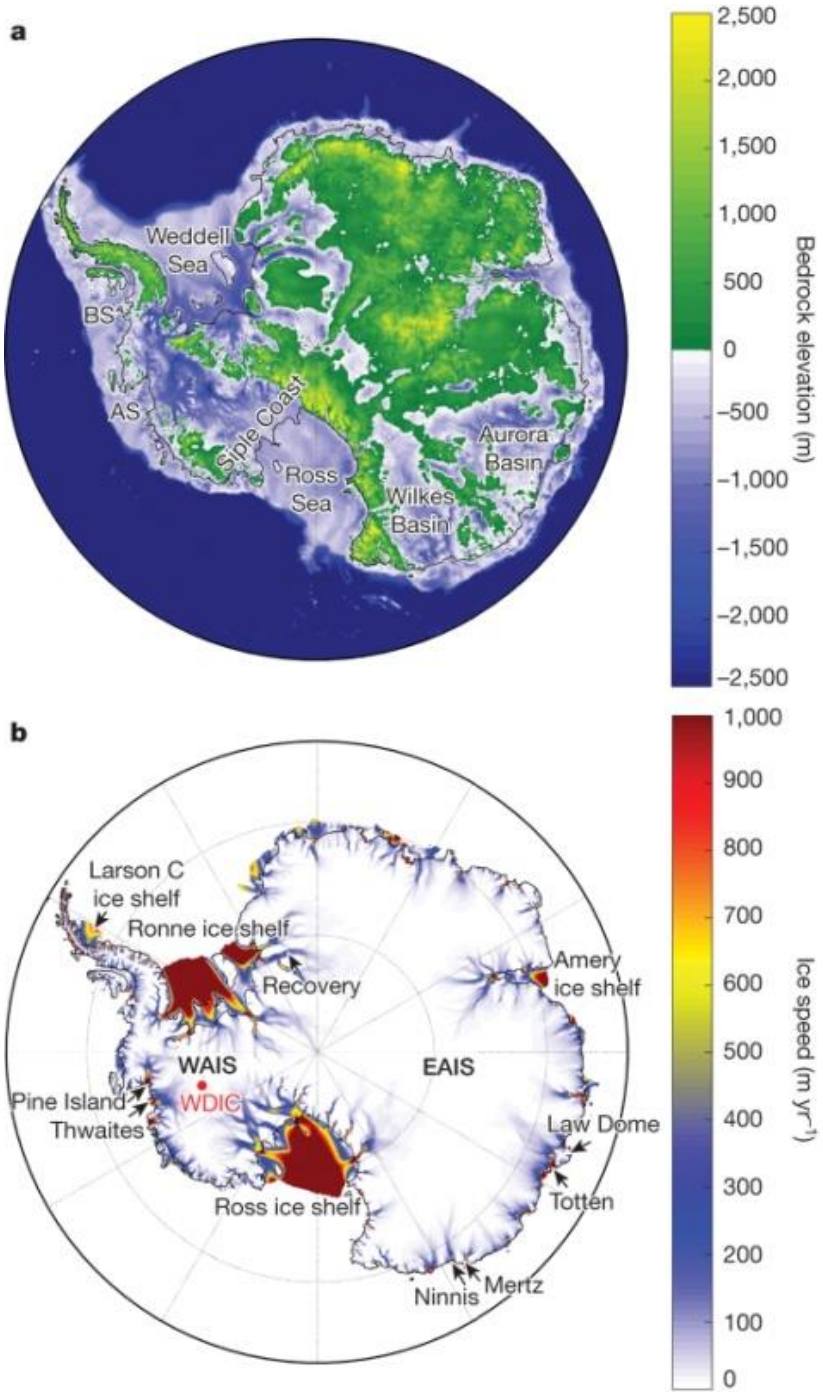

Figure 2.4: a) Bedrock elevation from Bedmap 2. b) Show model surface ice speeds (from numerical ice-sheet model), grounding lines (black lines), the location of major ice streams, outlet glaciers and buttressing ice shelves relative to the underlying topography (a). Figures by DeConto and Pollard (2016) with topography and ice thickness data from Fretwell et al. (2013)

The west Antarctic ice sheet (WAIS) is one of the most dynamic climate systems on Earth. Here the cryosphere, interacts with the atmosphere, hydrosphere and lithosphere in one of the coldest regions in the world. The region has responded to climate variability on a

range of timescales. The ANDRILL project revealed evidence of some 74 cycles of ice sheet buildup and retreat during a 6-million-year stretch starting in the Miocene Epoch some 20 million years ago (Schiermeier, 2008).

The WAIS is marine based (Figure 2.4 a), meaning that its grounding line is beneath the sea surface, some places at about 1000-1200 m below sea level, on a bed with locally reverse slopes. Such a configuration with grounding beds deepening inland, is associated with ice sheets prone to rapid grounding-line retreat and ice-sheet instability (Ross et al., 2012). Thus, the ocean – ice sheet interaction can amplify even small subsurface ocean temperature changes. One of the largest uncertainties when it comes to predicting sea level rise is the iceberg calving rate —the rate at which marine terminating glaciers will discharge ice into the ocean. A new study by Cook et al. (2016) has found that ocean warming is the primary cause of retreat of glaciers on the western Antarctic Peninsula, and this region is currently one of the largest contributors to global sea level rise. There is a high uncertainty coming from the possible instability of the West Antarctic Ice Sheet. According to theoretical (Weertman, 1974; Schoof, 2007) and recent modeling result (e.g. Favier et al., 2014; Joughin et al., 2014; DeConto & Pollard, 2016), this region could be subject to marine ice sheet instability (MISI) (Figure 2.5), which could lead to considerable and rapid ice discharge from Antarctica.

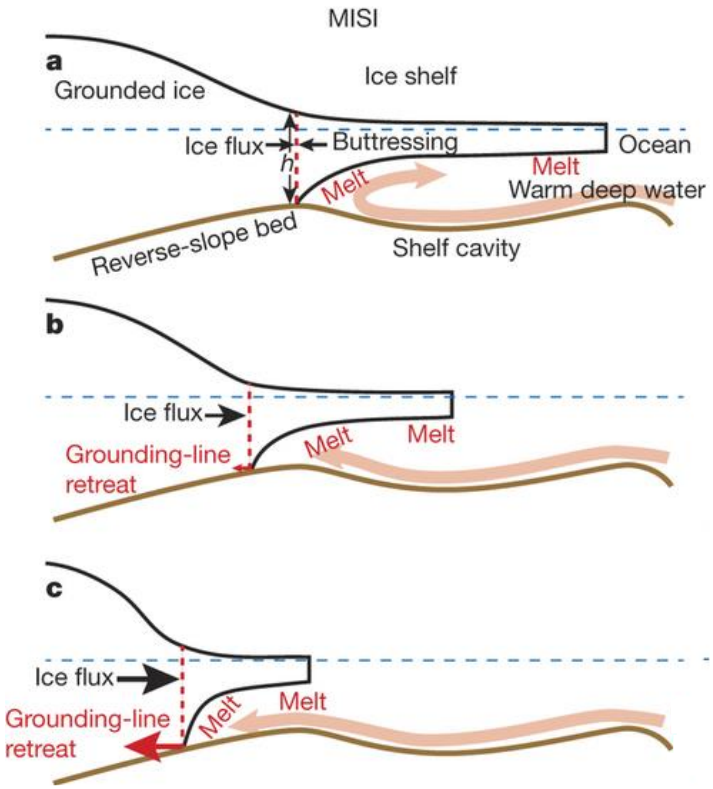

Figure 2.5: Shows typical west Antarctic marine ice sheet instability (MISI) (a-c) with advection of warm deep water into the shelf cavity of marine-terminating ice-sheet on a reversed slope, with a buttressing ice shelf (Rignot et al., 2008)

2.3.1 Ice shelves

Ice shelves, the floating extension of the ice sheet, assists in holding back the flow of the ice sheet. Ice shelves, and their buttressing effect, may be highly sensitive to ocean forcing. Satellite images have shown high rates of iceberg calving from Antarctic ice shelves that have had basal melt-induced thinning (Liu et al., 2015). A possible reason for the thinning is the incursion of warm CDW penetrating deeply into cavities below the ice shelves (Jacobs et al., 2011) melting the base of ice shelves (Figure 2.6).

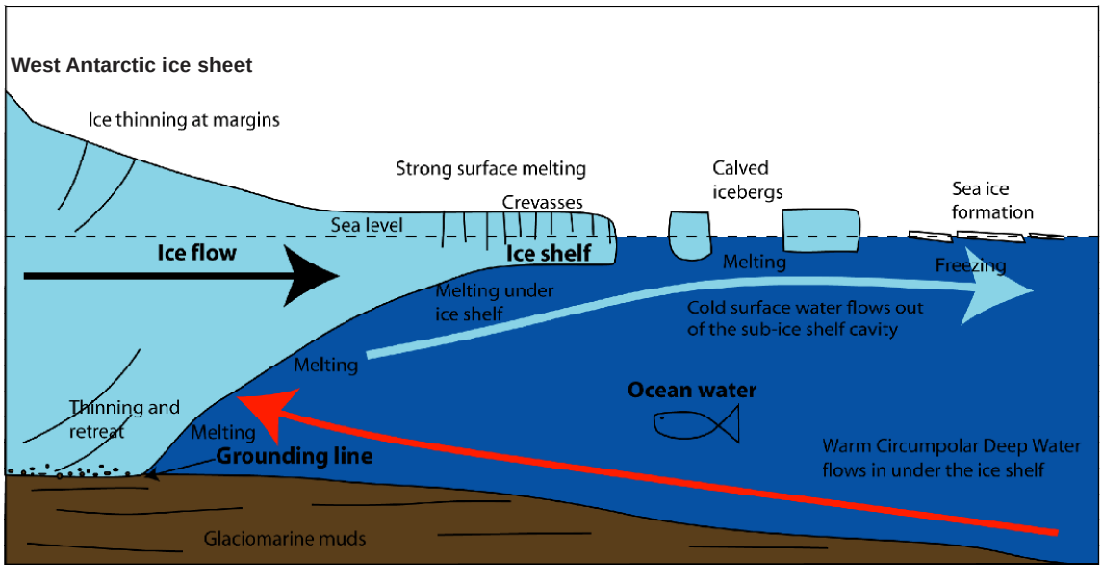

Figure 2.6: Simplified schematic figure of Ice shelf with sub-shelf melting, grounding line retreat and increase ice flow.

Increased basal melt has led to thinning of the ice shelf and reduced restraints on the flow of grounded ice sheets upstream. All of this has led to inland migration of the grounding line (boundary between the floating ice shelf and physically grounded ice on the bed rock). Loss of ice can also results from warm air being brought over the Peninsula by the stronger westerlies forced by changes in the SAM, driven ultimately by the development of the ozone hole (Thompson et al., 2011), and ice-shelf retreat resulting from increased fracturing via melt-water infilling of pre-existing crevasses (Scambos et al., 2003). Both the east and west coast of the Antarctic Peninsula is currently an area of concern with several unstable ice shelves: The Larsen Ice Shelf is situated along the northeastern coast of the Antarctic Peninsula, one of the fastest-warming places on the planet. In the past three decades, two large sections of the ice shelf (Larsen A and B) have collapsed (Domack et al., 2005). A third section (Larsen C) seems like it may be on a similar trajectory, with a new iceberg poised to break away soon (NASA earth Observatory, 2016)(Figure 2.7).

Following the disintegration of East Antarctic Peninsula's Larsen A and B ice shelves in 1995 and 2002, Larsen A and B glaciers experienced an abrupt acceleration (300% on average). The associated mass loss increased from 3±1 in 1996 and 2000, to 31±9 Gt yr−1 in 2006 (Rignot, 2006). It is not yet totally clear which of the basal lubrication of glaciers and loss in buttressing effect process exerts the most control on ice sheet flow. However, most glacier equilibrium lines in the eastern Peninsula are close to grounding lines

(Morris & Vaughan, 2003), thus surface melt should not be a major factor in the glacier acceleration because it is mostly occurring on the ice shelves (Rignot et al., 2004).

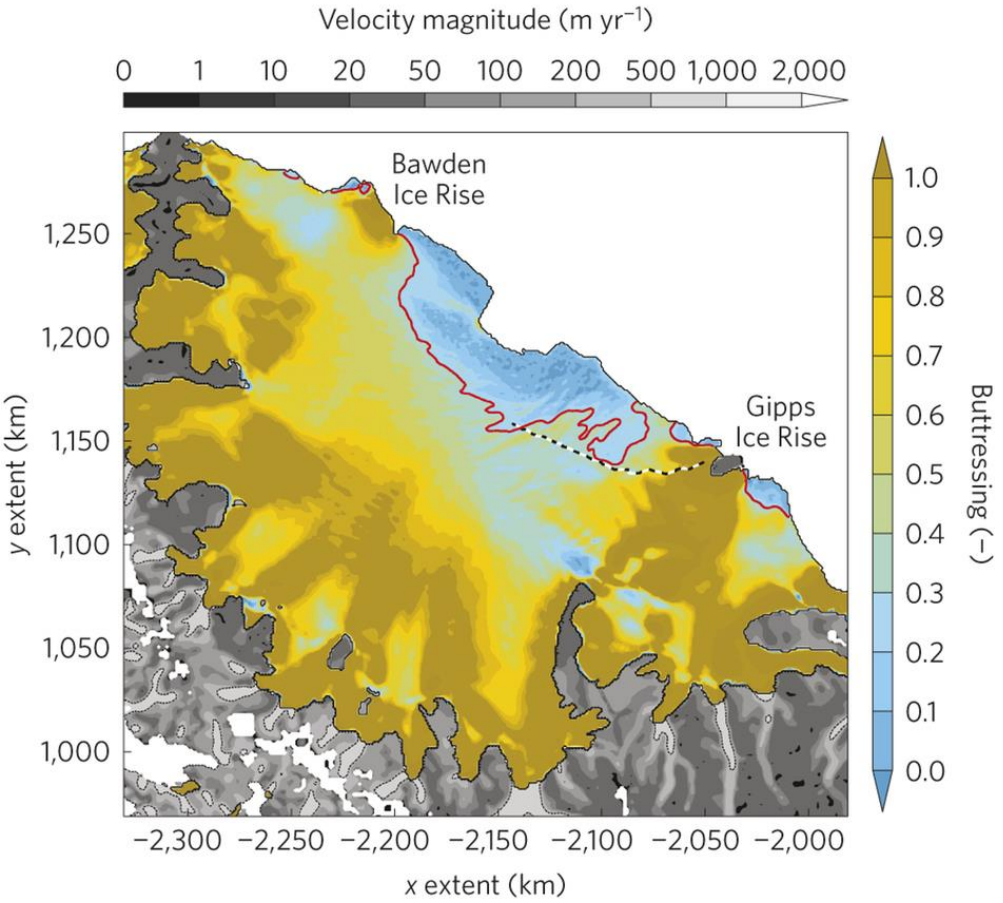

Figure 2.7: Buttressing provided by Larsen C ice shelf, Antarctic Peninsula, based on a model simulation (Elmer/Ice). Buttressing values range between 0 (no buttressing) and 1 (high buttressing). The red contour shows the buttressing=0.3 isocline. Observed ice velocity is also shown (Fürst et al., 2016).

2.3.2 Icebergs

Icebergs forms through calving at ice shelves and glacier tongues in coastal areas where glaciers terminate in the ocean (Figure 2.6). Iceberg meltwater, turbulent advection and input terrigenous debris creating localized nutrient and iron (Fe) rich environment associated with icebergs, alter water column structure and chemical properties, increase sea ice production (Mazur et al., 2017), and acts as hotspots for biological activity (Smith et al., 2007) and enhanced carbon uptake (Smith et al., 2011).

2.3.3 Sea ice

Hypotheses, models and observations suggest that the Antarctic sea ice plays an important role in the state and variability of regional and global climate through the ice albedo feedback, its insulating effect on air-sea exchange, and impact on deep water formation and fresh water budgets (e.g. Fletcher, 1969; Curry et al., 1995; Rind et al., 1995). The sensitive sea ice is the first to melt in a warming climate, creating a positive feedback because of the reduced albedo. Satellite-based sea ice record (1979–2013) shows that over the recent decades, sea ice has increased in the SH, as opposed to the significant decrease in sea ice over the Arctic Ocean. A study (Bintanja et al., 2013) found that the subsurface ocean warming of ice-shelves creating basal melt, increased freshwater runoff, is responsible for an increase of sea ice in the winter months. The meltwater from the WAIS reduces the salinity and density of Southern Ocean surface waters, inhibiting the heat exchange between the cold surface and the underlying warmer water, and thus sustain Antarctic sea ice (Manabe et al., 1991). As a result has the sea ice surrounding Antarctica expanded (Turner & Overland, 2009) with maximum extent in 2015, in contrast to Arctic sea ice, which reach a minimum in 2012 (NSIDC, 2017). Another study (Yuan, 2004) show strong covariability between sea ice and El Niño–Southern Oscillation (ENSO), suggesting a teleconnection between the strengthening of the polar front jet leading to more storms, warmer conditions and less sea ice in the southern Bellingshausen and western Weddell Seas (west AP) but colder conditions and more sea ice in the Amundsen and Ross Seas (east AP) (Stammerjohn et al., 2008). The opposing effects on the eastern and western side of the Antarctic Peninsula during ENSO events are referred to as the Antarctic Dipole (Figure 2.3).

This year (2017), sea ice extent contracted to 2.28 million of square kilometres on February 13th, according to daily data from the US National Snow and Ice Data Center (NSIDC, 2017), which is smaller than the previous low in 1997. This turn of events could be an anomaly and not in line with the current trend. More local (or less understood large) scale processes should be investigated to understand recent Antarctic sea ice variability (Liu et al., 2004).

3 Study area

The sediment core GS08-151-02MC-A used in this study was cored on the North Scotia ridge in the Scotia Sea, east of the Drake Passage. The core position of 53° 31.813 S; 44° 42.143 W at 2750m depth is just south of the Polar Front, at CDW depths (maximum NADW influence) (Figure 3.1).

3.1 Geographic and bathymetric setting

The Scotia Sea is situated in the southwestern Atlantic Ocean sector of the Southern Ocean, and developed coeval with the opening of Drake Passage, which started in the Late Paleogene (Lawver et al., 1992). It consists of a series of back-arc basins formed over the last 30 Ma on the boundary between the Antarctic Plate and the South American Plate (Figure 3.1 inset; Barker et al., (1991)). The Scotia Sea is bound on the north, east and south by the Scotia Ridge, an elongate arc of islands, including Falkland Islands, South Georgia, South Sandwich Island the South Orkney Islands, and the South Shetland Islands and submarine ridges. The North Scotia ridge is discontinuous, only rising above sea level a couple of places (e.g. Shag rock and South Georgia). The constriction of the Drake Passage and the bathymetry of the Scotia Ridge strongly affect ocean circulation resulting in significant mixing and vertical circulation associated with interaction of wind stress, flow and bathymetry. The topographical and bathymetric restraints on wind patterns and ocean circulation in the Southern Ocean help sustain the Antarctic sea ice (Nghiem et al., 2006) and the positions of frontal systems (Talley, 2011).

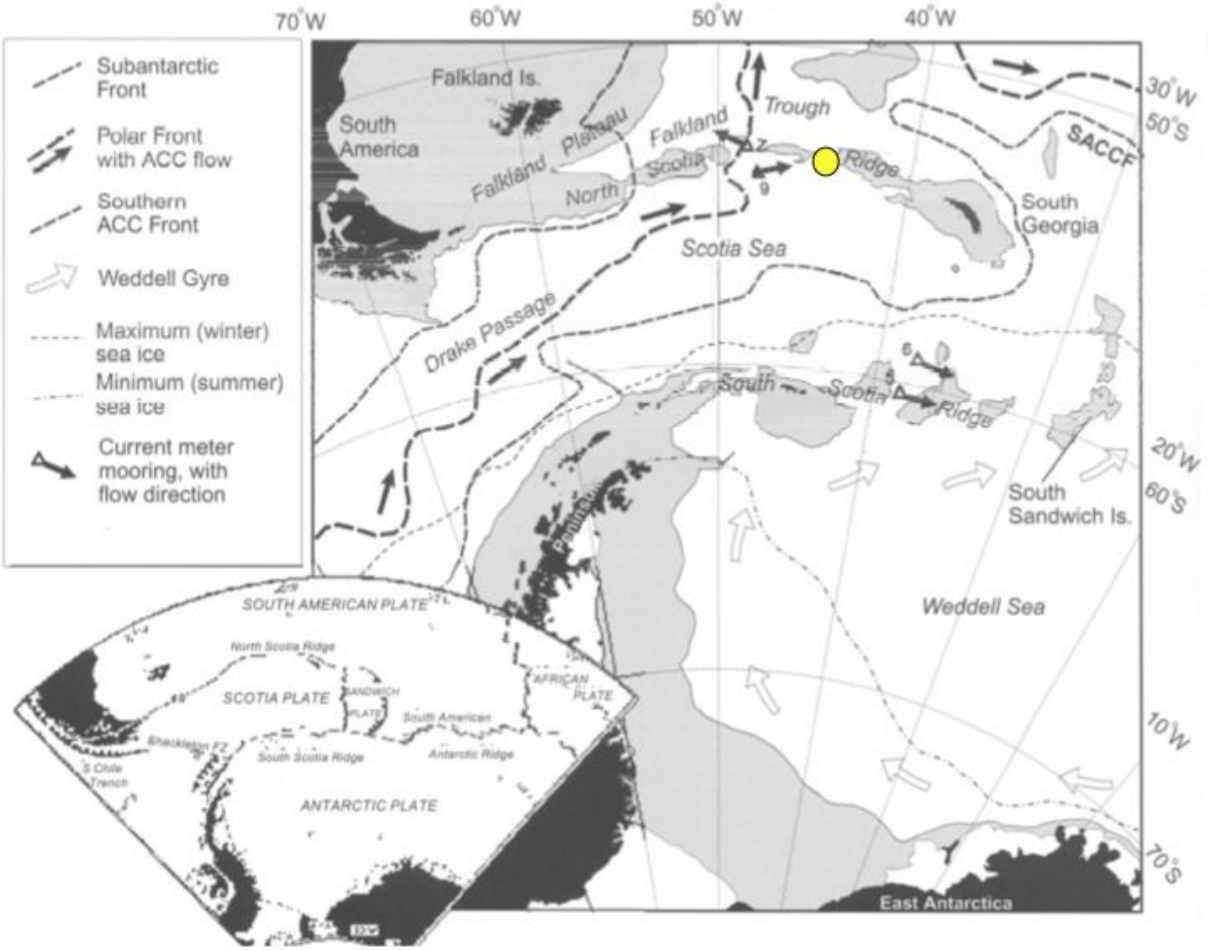

Figure 3.1: Map of the Scotia Sea with bathymetric features, tectonic plates and oceanographic feature. The location of core GS08-151-02MC-A is denoted by yellow dot. The shaded gray areas are shallower than 2000m. The figure is modified after Pudsey and Howe (2002), with oceanographic fronts defined by Orsi et al., (1995).

3.2 Oceanographic setting

This subchapter will describe the water masses, ocean circulation and frontal systems in the study region.

3.2.1 Ocean water masses

The physical properties and composition of ocean water masses are determined through the exchange of heat, moisture and dissolved gases with the atmosphere and/or ice, as well as biogeochemical processes. Thus, the relative physical properties, nutrient

concentration and ^{14}C ages of these water masses can be used to distinguish water masses from each other and trace them through the oceans. The different ocean water masses in the Atlantic Ocean have been traced and described in Figure 3.2 and for the global overturning circulation in Figure 2.2.

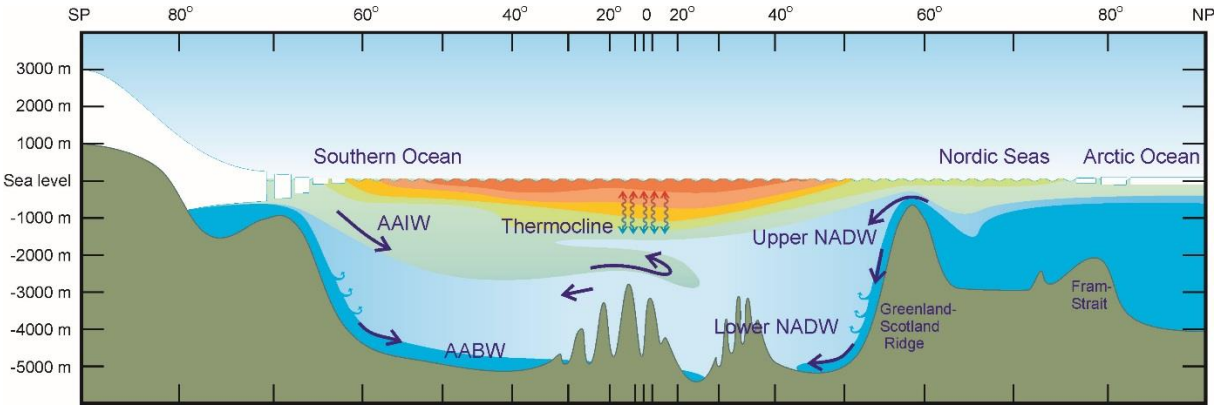

Figure 3.2: Idealized meridional section representing a zonally averaged picture of the Atlantic Ocean (BIAC, 2017, Copyright Ilker Fer, GFI/UIB)

North Atlantic Deep Water (NADW), formed through convection when water flowing northward in the Atlantic Ocean get denser and sinks in the Nordic Seas due to evaporation and brine rejection leading to increased salinity and decreased temperature. NADW has the characteristics of high oxygen content, potential temperature of 2-4 °C, salinity around 35 psu (Smethie et al., 2000) and low nutrients due to high photosynthetic activity in the source area. The high salinity, nutrient-poor NADW flows southward in the western Atlantic where it is continuously enriched with nutrients from sinking organic matter from the surface redissolved in the deep ocean (Broecker, 1992). Antarctic Bottom Water (AABW), formed in the Weddell and Ross seas from surface water cooling in polynias and below ice shelves, is charactherized by being the coldest (−0.8 - 2 °C) densest and most oxygenated of the water mass of the oceans (Talley, 1999). Because AABW is denser than NADW, it sinks underneath NADW and flows northward in the deepest basins of the Atlantic where it is an important driver of deep global ocean ventilation (Talley, 2011) (Figure 3.2 and 2.2).

To show in detail the influences of different water masses in the study area, the core GS08-151-02 location plotted in ocean data view (Schlitzer, 2008) , with present hydrographic

data from Gouretski and Koltermann (2004). This data is part of The World Ocean Circulation Experiment (WOCE) with aim of presenting a high quality data set, which represented the present state of the oceans. Figure 3.5 show how temperature and salinity in the water column of a transect through the South Atlantic Ocean, is used to distinguish NADW and AABW.

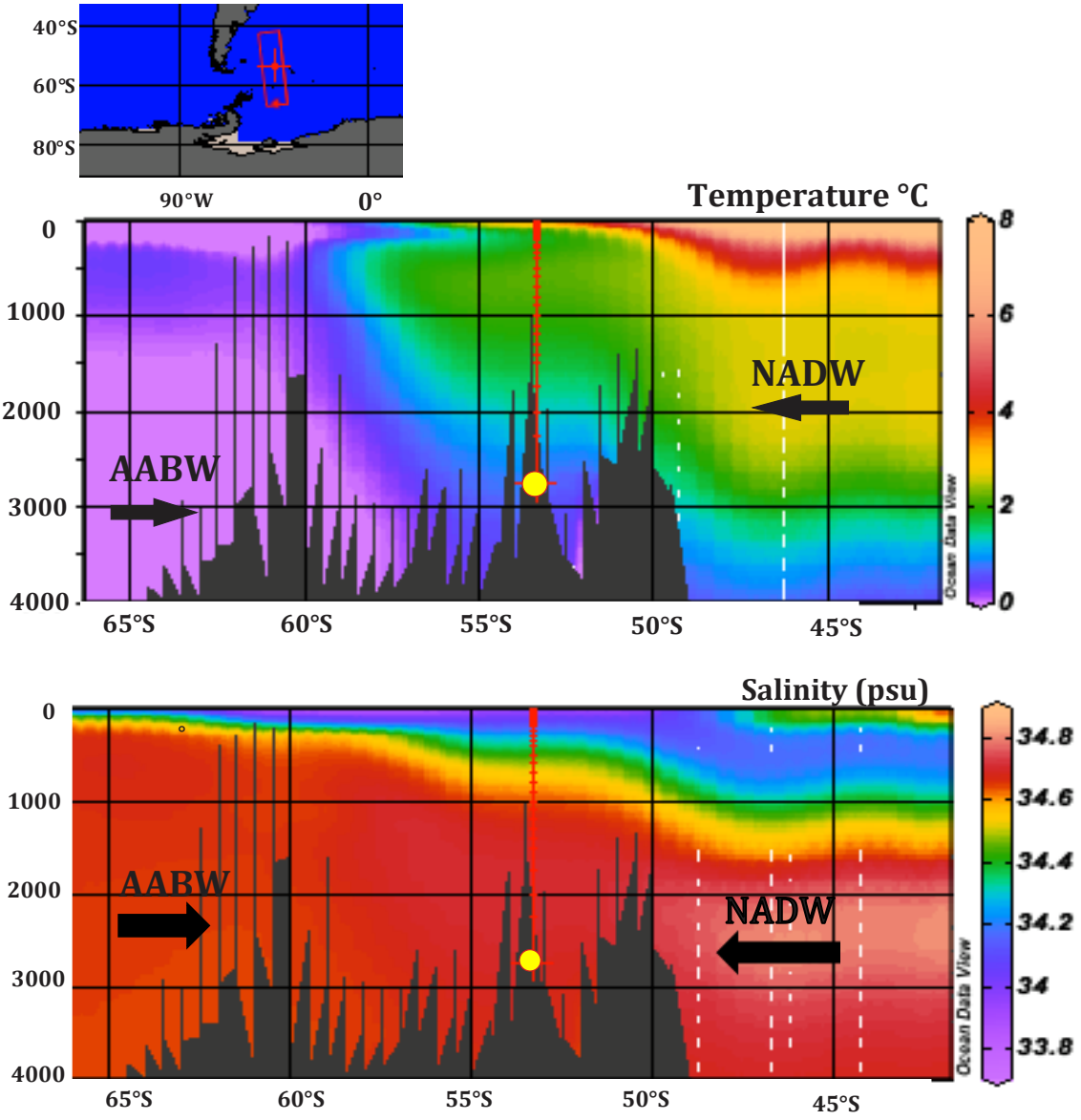

Figure 3.3: North-south profile of the western South Atlantic basin showing temperature (top) and salinity (bottom). Apparent are the two principal water masses of the deep Atlantic: North Atlantic Deep Water (NADW) and Antarctic Bottom Water (AABW), where arrows indicate average flow direction. Note the significant difference in temperature from surface to bottom, and from north to south. Core location of GS08-151-02 is shown as yellow circle. The figure is generated using Ocean Data View (Schlitzer, 2008) with WOCE global hydrographic climatology

data (Gouretski & Koltermann, 2004), based on a yearly average with a slight bias towards the Northern hemisphere summer.

The surface and bottom water masses south of 60° exhibit lower temperature, and thus are interpreted as Antarctic in origin. The intermediate water masses (2500-1000 m depth range) are North Atlantic in origin, evident as plume of higher salinity and temperature entering from the north. NADW is joined by the AABW between 50-60°S in the Southern Atlantic to form a mixed deep water (CDW). Figure 3.3 and 3.4 clearly show the warmer and saltier surface waters of the subtropical regimes further north and relatively cold and fresh surface waters at core site. The red mark illustrating the core location show annual average SST around 2-4°C, and beyond the core location the SST rapidly increases at lower latitudes. The major region for production of Antarctic Bottom Water is the Ross Sea and the Weddell Sea (Gordon, 1971). In the Weddell and Ross Sea are SST below 0°C thus consistent with AABW originating from these areas.

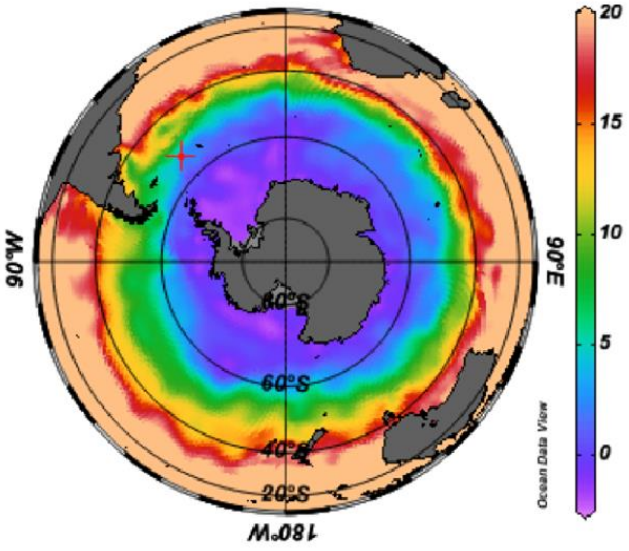

Figure 3.4: Show surface ocean water in SH. The core site shown on map as a red cross. The figure is generated using Ocean data view (Schlitzer, 2008) with WOCE global hydrographic climatology data from Gouretski and Koltermann (2004), based on a yearly average with a slight bias towards the Northern hemisphere summer.

3.2.2 Ocean Circulation in the Southern Ocean

The Southern Ocean is dominated by the eastward flow of the world's strongest current: Antarctic Circumpolar Current (ACC). After the opening of Drake Passage the absence of continental barriers permits the existence of the eastward-flowing ACC, essentially driven

by the south westerly wind (SWW). As a result the surface currents are the strongest, where the wind effect is largest.

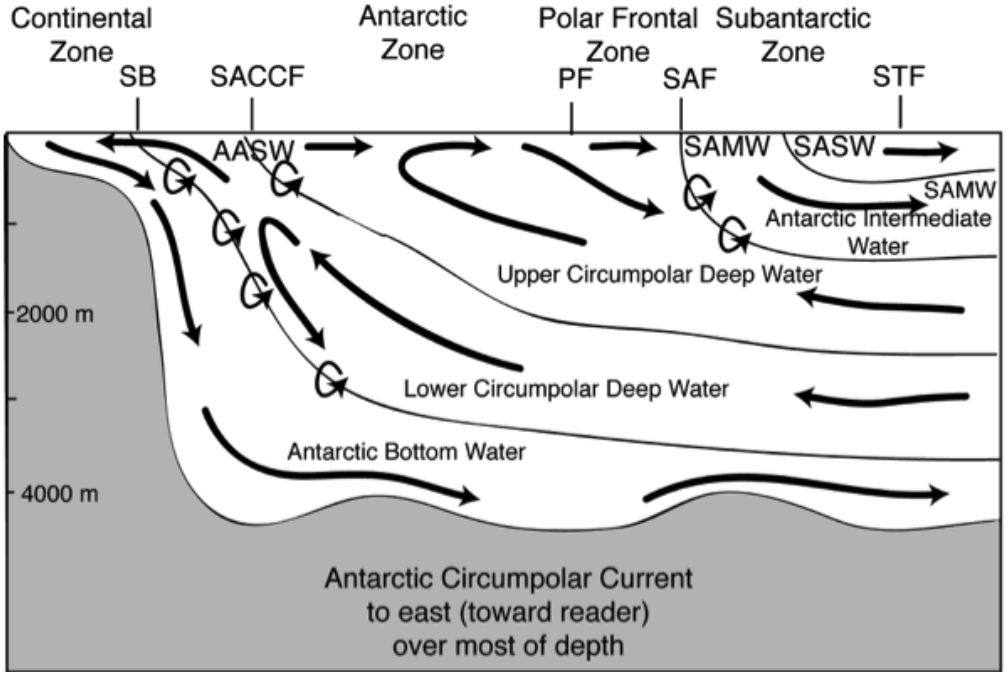

Figure 3.5: A schematic view of the meridional overturning circulation in the Southern Ocean and the layers of the ACC. Modified after Speer et al., (2000)

Figure 3.5 shows the water masses contributing to the ACC. Overlying the Antarctic continental shelf is the Antarctic Surface Water (AASW) in the upper 100–120 m (Hoffmann et al., 1996). The cold Antarctic Intermediate water (AAIW) forms at the Polar front zone located between 50°S and 60°S where the water gets colder and sinks (L. Talley, 1996). Stratified beneath the salinity minimum of the AASW and the permanent pycnocline at 150–200 m, is the relatively warm (>1°C) and saltier (34.64 psu) Circumpolar Deep Water (CDW) (Smith et al., 1999). CDW is the main body of water within the ACC and includes NADW, Indian deep water (IDW) and Pacific deep water (PDW), and also locally-formed dense waters, such as Weddell and Ross Deep Waters, that are not quite dense enough to become AABW (Orsi et al., 1995).

The ACC brings CDW into the Weddell gyre's southern limb near 30°E (Orsi & Whitworth, 1993) and is gradually cooled and freshened by mixing with ambient waters as it flows westward near Antarctica. Along the Gyres path, CDW interacts with dense, relatively saline waters cascading off of the broad glaciated continental shelves of the south-western

and western Weddell Sea, resulting in the production of AABW (Carmack & Foster, 1977), that gets transported down the continental slope and stratified at the ocean bottom. Thus, the ACC and the Weddell gyre, in the Southern Ocean the (Figure 3.1) plays a key role for the global thermohaline circulation being one of the three main regions of deep-water formation of the world ocean (Rahmstorf, 2002).

3.2.3 Frontal systems

Fronts are oceanographic boundaries that separate zones with distinct water mass properties. In the Southern Ocean, three major fronts can be identified: the Southern ACC Front (SACCF), the Polar Front (PF) and the Sub-Antarctic Front (SAF) (Orsi et al., 1995) (Figure 3.6). The ACC flow within these three fronts closely follows the bathymetry; strong (or shallow) bathymetry locks the fronts in place (Talley, 2011).

The southern ACC front was defined as the southern boundary of the upper circumpolar deep water. While the Subtropical Front (STF), interrupted only by South America, marks the northern most extent of subantarctic surface waters (Orsi et al., 1995). The Antarctic Polar Front (PF) situated between the Falkland islands and South Georgia, marks the location where Antarctic surface waters moving northward sink below subantarctic waters (Deacon, 1933).

The core is located north of the SACCF and south of the PF. The mean SST change across the PF over a 7-year period was measured at 1.44°C by satellite across an average width of 43 km (Moore et al., 1999). The core was chosen for its close proximity to the PF, thus recording any movements of the front during the late Holocene. Furthermore, eastward flow within the ACC is concentrated between the SAF and PF (Nowlin Jr & Clifford, 1982) and the center of the SWW is at 55-50°S (Lamy et al., 2010). GS08-151- 02 at 53°S is therefore ideally located to track past changes in both SWW and ACC.

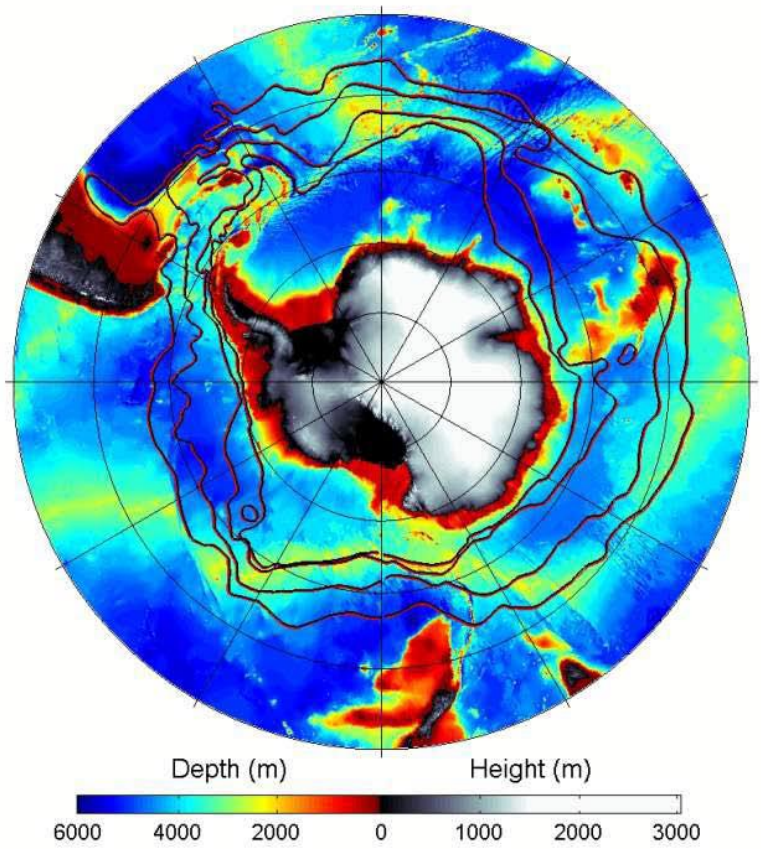

Figure 3.6: The land topography and the bathymetry of the seabed around Antarctica (in metres). Four major oceanic fronts are shown (not labelled), which are (north-to-south): the Sub-Antarctic Front (SAF), the Polar Front (PF), the Southern ACC Front (SACCF) and the Southern Boundary (SB). The Antarctic Circumpolar Current runs between the SAF and the SB. Figure by Turner et al. (2009) using frontal locations adapted from Orsi et al., (1995)

3.2.4 Sediment supply

The mixed biosiliceous-terrigenous sediment supplied to the core site in the Scotia Sea is controlled by the east-flowing ACC with influence from the Weddell Gyre. The sediment has been built-up on the seabed of the northern Scotia Sea since the Early-Middle Miocene, simultaneous with the opening of Drake Passage and the inception of deep-water flow (Howe & Pudsey, 1999). The biogenic sedimentation in the Scotia Sea is also highly controlled by the seasonal occurrence of sea ice. The minimum (early March) and maximum (August-September) sea ice limits together with ocean currents and core location are shown on Figure 3.1 and 4.1 (Pudsey & Howe, 2002).

Icebergs calving off the Antarctic ice sheet is also a major source for terrigenous input. 90% of an iceberg lies below the water, iceberg transport is thus consistently dominated by oceanic currents rather than wind stress (Crepon et al., 1988). Once free, icebergs become entrained in the counterclockwise Antarctic Coastal Current (Figure 3.7), eventually entering the clockwise rotating Weddell gyre that brings water masses and icebergs from west Antarctica westward along the Antarctic coast, northward alongside the Antarctic Peninsula in the western Weddell sea, ending up entrained into the ACC (Echols, 1967). This is the so-called *Iceberg Alley*.

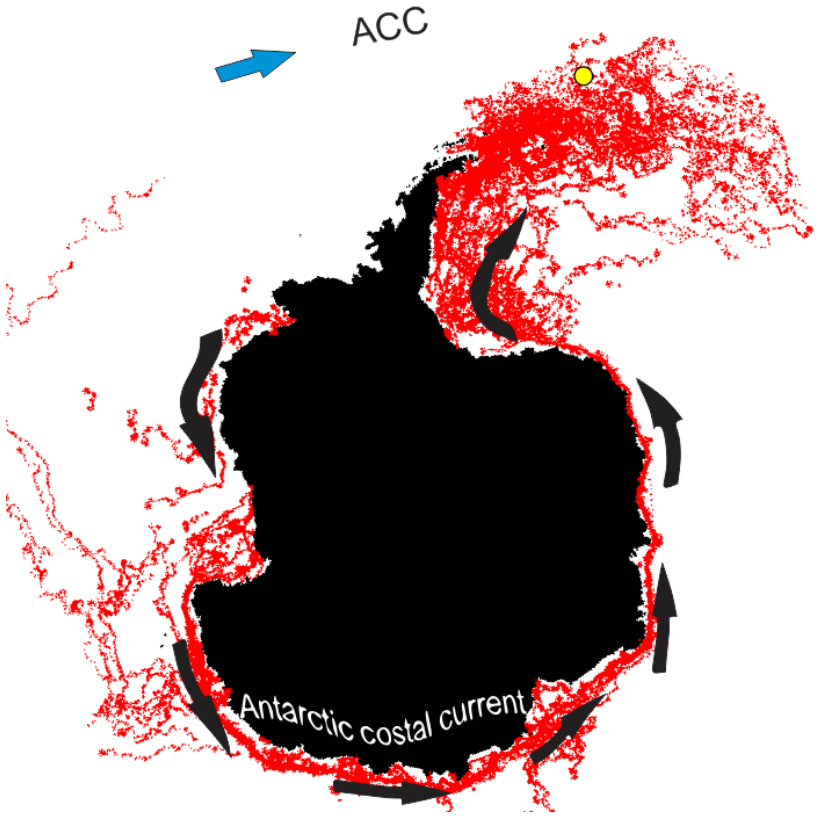

Figure 3.7: The figure shows locations of the circum-Antarctic drift of icebergs (red; ≥5 km in length) calving off the Antarctic ice shelves from 1999 to 2009, and the core location marked as yellow dot the figure is modified after Stuart and Long (2011)

The iceberg trajectory map after Stuart and Long (2011) (Figure 3.7) is based on satellite imagery that detect the icebergs as high-backscatter targets surrounded by the lower-backscatter regions of sea ice and sea water. Icebergs not following this general pattern of the iceberg alley are presumably pushed away from Antarctica by katabatic winds while encapsulated in sea ice.

Sediment mixing can occur as a result of bottom-dwelling burrowing organisms or through the ocean bottom currents or be disturbed and reworked by turbidity flows or other downslope sediment transports, such as slides, slumps or debris flows. CDW (the deepest element of the ACC) is the current that influence sedimentation on the core site (Alejandro H. Orsi et al., 1995). The core showed no evidence for turbidites or sedimentary disturbance (Ninnemann, Pers. Comm. Post-cruise work from the IPY Paleodrake project) and the relatively high sedimentation rate should help to minimize the effect of smoothing of millennial scale events trough bioturbation (Anderson, 2001). Depositional and bottom current processes in the ocean can also modify the grain-size distributions, known as winnowing (Compton & Compton, 1985). Losing their fine fraction to scouring by bottom currents can lead to an overestimation of the amount (%) of IRD making up the sediment (Hemming, 2004).

The core site is ideally placed on the fringes of the main alley of icebergs travelling around Antarctica, in an area of low sediment mixing and outside the limits of maximum sea ice, thus providing an undisrupted, integrated signal of iceberg input.

4 Material, methods and theory

This chapter describes the procedures that were used when the marine sedimentary samples were prepared for stable isotope geochemistry analyses. The theory behind the application of stable isotopes in paleoclimatological studies are introduced and possible sources of errors are highlighted.

4.1 The core GS08-151-02 MC A

The marine sediment core GS08-151-02 was cored onboard the R/V *G.O. Sars* during its 3-month long international polar year (IPY) expedition to Antarctica, as part of the PALEODRAKE project. The aim of the PALEODRAKE project were to reconstruct natural climate variability in the Drake Passage and the Scotia Sea region to elucidate the coupling between climate, Antarctic water mass properties, and circumpolar circulation on decadal to millennial timescales. The 25 cm long multicore GS08-151-02 was recovered from 2750 m water depth east of Shag Rocks (SRP), North Scotia Ridge in the Scotia Sea west of South Georgia Island (53° 31.813 S; 44° 42.143 W) (Figure 4.1). The core site was selected after closely monitoring seismic images from the Topas echo sounder onboard the vessel to find flat areas with thick layers of homogenous sediment cover.

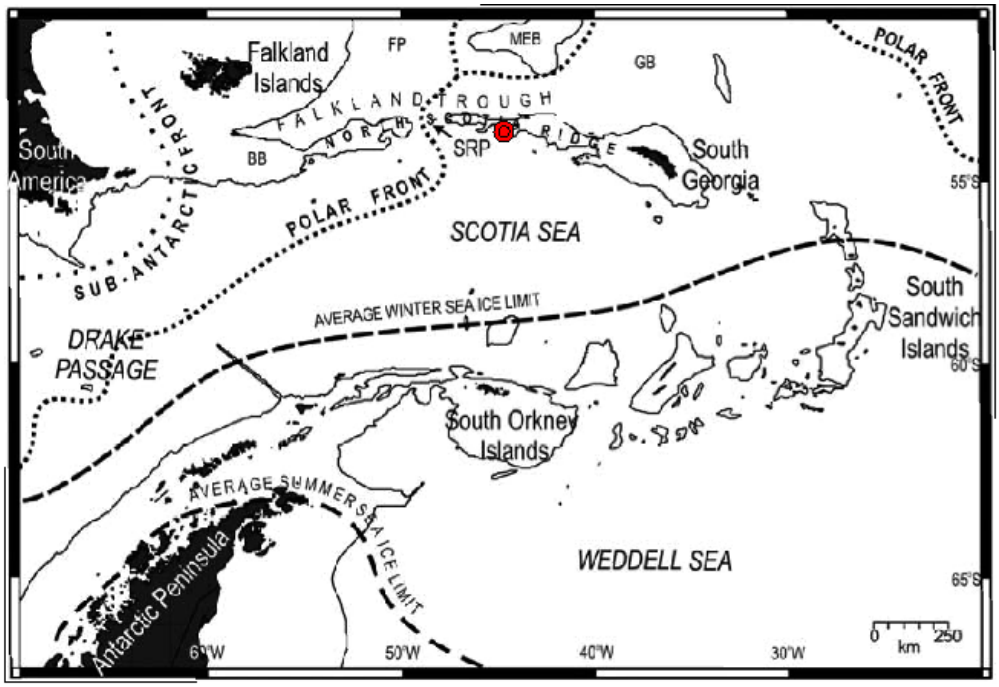

Figure 4.1: Map with the coring station GS08-151-02 (53° 31.813 S; 44° 42.143 W at 2750m depth) marked in red. The figure is modified after (Allen et al., 2005) with frontal positions after (Orsi et al., 1995)

4.1.1 The multicore device

The multicore device is used to recover the undisturbed sediment-water interface. The multicorer used onboard *R/V G.O Sars* is a KC Denmark customized model 72 000 (Figure 4.2). The device is made up of a metal frame with 4 Plexiglas tubes that are 600 mm long and with a diameter of 110/105 mm. When lowered into the sea, water can flow through the tubes and when the metal frame reaches the sea floor, a release mechanism drives the inner part with the tubes slowly down into the sediment column. After the tube is filled with sediment a spring-loaded lid closes on top of each tube, creating a vacuum that holds the sediment in the tube as it is pulled up from the sea floor. Spring-loaded shovels are released under the tubes and cover the ends when the tubes emerge from the sediment to secure the sediment further as the device is raised back onboard. Since the multicorer penetrates the sediment at low speed and without a lock (core catcher) at the end of the tube it is successful in retrieving undisturbed sample of the sediment.

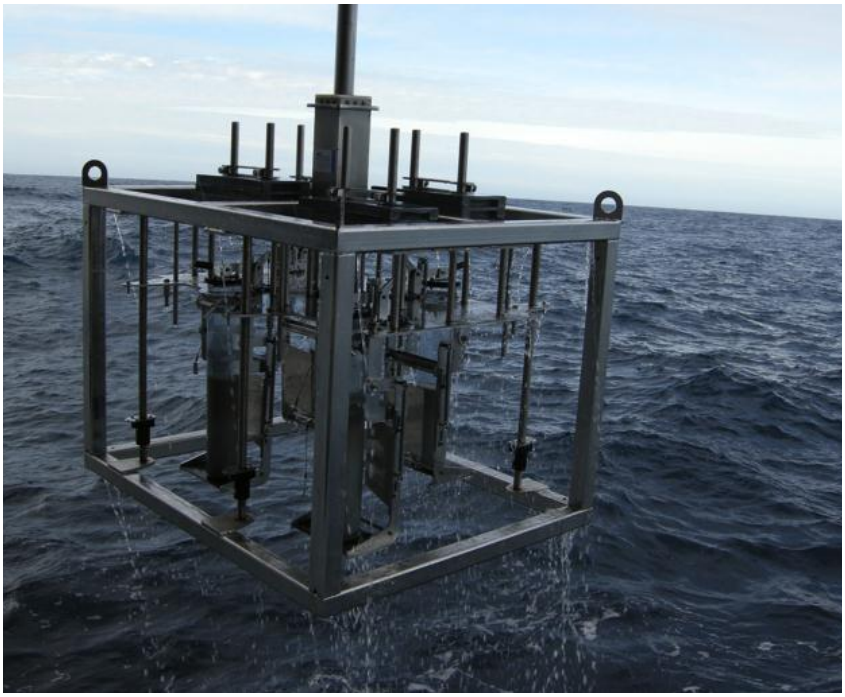

Figure 4.2: picture taken on the PALEODRAKE expedition of the multicore device on board the R/V G.O. Sars Photo: Øyvind Paasche

4.1.2 Core description

The multicore successfully recovered four cores of 25 cm each. On the cruise the cores were capped and stored vertically (top up). MC A core was drained and split in two sections. One archive half was stored and the working half was sampled every 0.5 cm. Visual examination of the core (Figure 4.3) show that the core consists mainly of soft mud with greyish, brown colour. The sediments are high in foraminifera content with no clear colour layering. The top most 1 cm layer consists of diatom fluff. Some foraminifera are visible in the uppermost centimetres.

Figure 4.3: Picture of the capped multicore prior to sampling. Photo: Øyvind Paasche.

4.2 Laboratory methods

The sedimentological preparations of the core were carried out in EARTHLAB and the isotopic measurements were analyzed in the FARLAB (Facility for advanced isotopic research and monitoring of weather, climate, and biogeochemical cycling) both at the Department of Earth Science, University of Bergen. The Accelerator Mass Spectometry (AMS) radiocarbon dating were carried out at the Leibniz Labor für Altersbestimmung und Isotopenforschung in Kiel, Germany (see chapter 5). Careful, accurate and precisely

handling of the samples throughout the process is essential to achieve reliable results and to limit the source of error.

4.2.1 Sample preparation

The working half of GS08-151-02MC A was sampled at 0.5 cm intervals (0-25.5cm) throughout the core. The wet weight was measured before the samples were soaked in distilled water and shaken for 12-24 hours to disperse the sediment. Afterwards the samples were wet-sieved into fractions of >63μm and <63μm and transferred to a drying cabinet (~55°) until all water had evaporated. The dried <63μm fractions were stored in sample bags and >63 μm fractions was poured into 52 individual sample glasses.

4.2.2 Lithic counts

William F. Ruddiman (1977) showed that >63 μm lithic grains are most likely derived by ice rafting and that lithic grains >150 μm definitely are. Hence, prior to counting, the samples were dry sieved on a 0.150 mm mesh, and then the >150μm sample fraction was split in equal parts, using a micro splitter, 7-9 times, until the remaining size was about 400 grains. The IRD grains and foraminifera (benthic and planktic) are counted under a microscope (Figure 4.4). The results are expressed as the percentages of IRD grains (% IRD) relative to total entities (i.e., foraminifera) in each sample and as number of IRD grains per gram sediment. Compared to the sample dry-weight, a weight percentage of IRD can also be calculated.

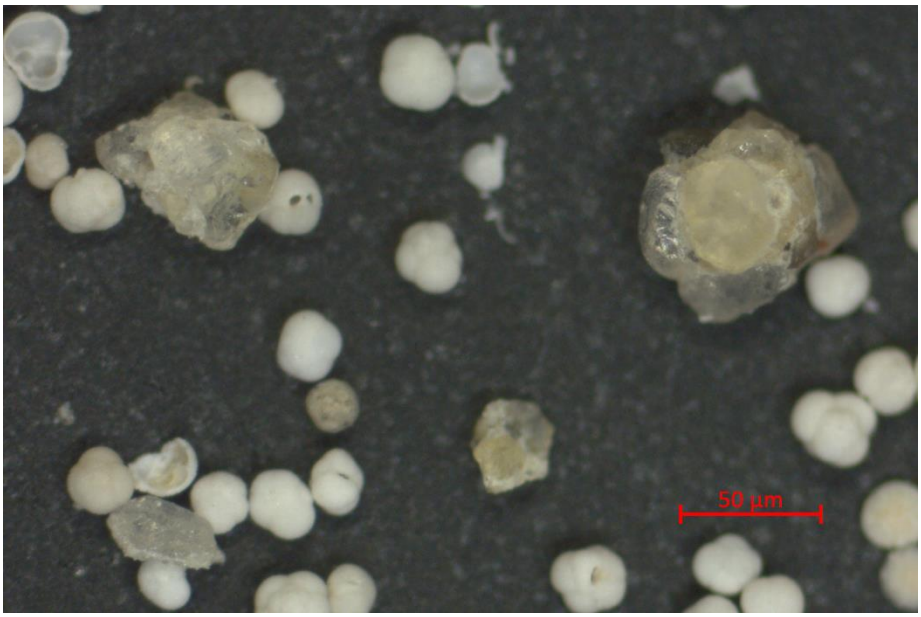

Figure 4.4: Picture of 4 IRD grains accompanied by foraminifera. Scale Bar = 50µm

4.2.3 Picking and selection of foraminifera

Two benthic and one planktic foraminifer species were selected to generate the stable isotope measurements in this study: The benthic foraminifera *Cibicidoides wuellerstorfi* and *Uvigerina peregrina* and the planktic foraminifera *Neogloboquadrina pachyderma* (sinistral). Prior to picking the shells, the samples were dry sieved in fractions; >250 µm, 250-212 µm, 212-63 µm.

Planktic foraminifera vary in size, through their life cycle and their depth habitat in the water column can also change resulting in different isotopic values for different sizes of the same foraminifera (Bijma et al., 1999).). In addition to habitat changes, metabolic effects (e.g. fast growth while juvenile) could also influence the isotopes (primarily carbon isotopes) potentially leading to an increase in $\delta^{13}C$ of planktic foraminifera as a function of size (Berger et al., 1978). Therefore, planktic foraminifera are picked from the same size fraction (212-250µm) to avoid intra-population variance and minimize habitat and metabolic related influences. Size has no impact on the isotopic composition of most benthic foraminifera (Wefer & Berger, 1991), and hence the two benthic species in this study are picked from every size fraction of the sample (>63µm).

The abundance of planktic species was high throughout the core, and about 40 individual shells of N. *pachyderma* (s) were picked for every sample. However, the abundance of the benthic foraminifera species was low in all samples. Some of the samples were even barren of both benthic species. Thus, every specimen of *U*. *peregrina* and *C. wuellerstorfi* found was therefore picked.

4.2.4 Stable isotope sample analyzes

The Isotopic differences between the samples measured in this study are very small as there is only a minor difference (fractionation) in the behavior and distribution of foraminifera-based stable C and O isotopes in marine environments. Hence, careful handling of the sample is undertaken to avoid any isotope fractionation or contamination during chemical and physical treatment.

When preparing the samples for the mass spectrometer measurements, only the most intact and clean planktic foraminifera were selected. The optimal sample weight for the mass spectrometry analyzes on calcareous microfossils is 40-70 μg in FARLAB but the mass spectrometer can obtain reliable results on samples as small as ~ 7 μg. For planktic foraminifera, with habitat in a range of depths in the water column, it is important to establish a population average in a measurement, running several individual shells per analyses. For benthic foraminifera on the other hand, one specimen per measurement enough as long as it exceeds the minimum signal threshold of ~ 7 μg (pers. Comm. U. Ninnemann). The foraminifer shells were weighed in order to find an approximation of how many were needed to meet the optimal weight range. In general, about 6-7 shells of the abundant *N. Pachyderma* (s) provided the optimal mass for analyses (50-60 μg) and for the less abundant benthic species all specimens found were measured whenever possible, usually combing 1-2 individual shells per analyse.

After picking foraminifera from all core samples, the shells were cleaned to remove contaminating material that could be attached to the shells. A few drops of methanol (CH_3OH) were added to each glass vial containing the sample, and afterwards the vials

were transferred to an ultrasonic bath containing de-ionized water for five seconds. The methanol, together with suspended contaminants, was then carefully removed using a syringe. Finally the samples were dried at 50°C in a drying oven before they were placed in the metal carousel ready for the Kiel IV automated carbonate device attached to the Finnigan MAT 253 mass spectrometer. This machine has the capacity to analyze 46 sample vials in one run. Each run usually consists of 38 carbonate samples and 8 standards.

Kinetic fractionation can occur when the foraminifera reacted with phosphoric acid (H_3PO_4) in the Kiel device to produce CO_2, the degree of which depends upon the reaction rate, which in turn is grain size dependent (Shackleton et al., 1974; Waelbroeck et al., 2005). Thus, if the planktic foraminifers are crushed prior to cleaning, there is some concern that this could alter the reaction rate and apparent isotopic signal. In the case that foraminifera are crushed into different sizes this may introduce variability in the results. Because planktic foraminifera were visually clean prior to cleaning I chose to clean and analyze intact planktic foraminifera and avoid introducing variability in the results due to potential differences in grain size and reaction rate.

The benthic specimens were held intact in order to preserve most of the mass during the crushing process. The acidic solution might bubble and transport the foraminifera up the side of the glass, where it can't be measured. Thus, after the mass spectrometry run, all the sample glasses were checked for any residual sample left on the sides of the glass. None of the glasses contained any residual material; all benthic specimens picked were measured (Appendix c).

Due to the overall high abundance of *N. pachyderma* (s), it was possible to measure 40-70 μg twice per 0.5 cm core depth interval in order to obtain a good population average, minimizing the analytical uncertainty (Appendix B), and to help quantify the uncertainty of sample replicates. In general, it was possible to measure a single specimen of *U.peregerina* to give an adequate amount of test material per sample, though the relative scarcity of this species temporally limited analyses to a single or no measurement (Appendix C, column 4). Therefore were my data supplemented by isotopic measurements of *U. peregrina* carried out prior to my labwork (Appendix C, Table column

1-3) (pers. Comm. U. Ninnemann). The sporadic abundance of benthic foraminifera causes the isotopic signal to be based on measurements ranging from one specimen to up to four replicate measurements (Appendix C).

4.2.5 Standards

Analyzing stable isotope ratios is complex work and even with sophisticated mass spectrometry equipment, operational variations (e.g related to sample size) and fractionation during acid digestion can occur. In order to achieve consistent long-term stable analyzes within a laboratory and to be able to compare data sets globally, between different stable isotope laboratories, we apply an international carbonate reference standard. The international standard, and/or an in house 'carbonate standard calibrated to the international standard, is analyzed in the same batch as the carbonate samples. This is the principle of identical treatment (IT): where samples and standards are treated and analyzed using the same methods and possible errors or deviations from the standard(s) and can be accounted and corrected for.

The standard notation when reporting carbon and oxygen isotope measurements in carbonates is called Pee Dee Belemnite (PDB), by definition: $\delta^{18}O = 0$ and $\delta^{13}C = 0$ (Epstein et al., 1953). Since the original PDB standard is used up and no longer available, several international standards have been ran against PDB for comparison (Rohling & Cooke, 1999). Vienna Pee Dee Belemnite (VPDB) is the new reference scale created by the United Nations International Atomic Energy Agency (IAEA)(Clark & Fritz, 1997). The standard defining the isotopic composition of water is the Vienna Standard Mean Ocean Water (VSMOW). For conversion between oxygen isotope ratios from carbonates (reported relative to VPDB) and oxygen isotope ratios from water (reported relative to VSMOW), the initial values are used in the following equation:

$$\delta^{18}O_{VSMOW} = 1.03091 \times \delta^{18}O_{VPDB} + 30.91 \qquad \text{Equation 4.1 (Coplen et al., 1983)}$$

The NBS-18 (National Bureau of Standards), distributed by the National Institute of Standards and Technology (NIST) and the International Atomic Energy Agency (IAEA) is used in every run at FARLAB as a stable isotope reference standard. In addition, the in-house standard Carrera Marble 12 (CM12) is also applied, with a weight range that spans

the weight range of the sample. The latter has values close to the international reference standard NBS-19 which it is calibrated against. The isotopic $\delta^{18}O$ and $\delta^{13}C$ values are calibrated against CM12 and NBS-18 and reported in per mill (‰) difference relative to the VPDB standard reference. The long-term internal precision of analysis of the MAT 253 instrument is determined by the precision of the replicate analyses of the working standards CM12 over a period of months. During the analysis period for the data presented in this thesis the long-term precision was ≤0.06 and ≤0.03‰ 1σ for $\delta^{18}O$ and $\delta^{13}C$ respectively.

4.2.6 Mass spectrometry

Mass spectrometry is, by far, the most efficient way of measuring isotope abundance. A mass spectrometer separates charged atoms and molecules on the basis of their masses based on their motions in magnetic and/or electrical fields (Hoefs, 2009). The stable isotope measurements were obtained in the facility for advanced isotopic research and monitoring of weather, climate, and biogeochemical cycling (FARLAB) at UoB.

To measure the carbon and oxygen isotope ratios of carbonate samples, a gas source mass spectrometer is usually used, following the design of Nier (1940). The Nier type mass spectrometer, Thermo Finnegan MAT 253, used in this study consists of three essential parts (Figure 4.3): a source to generate atoms into ions, a magnetic analyzer to separate the masses and an ion collection system (Faure & Mensing, 2005).

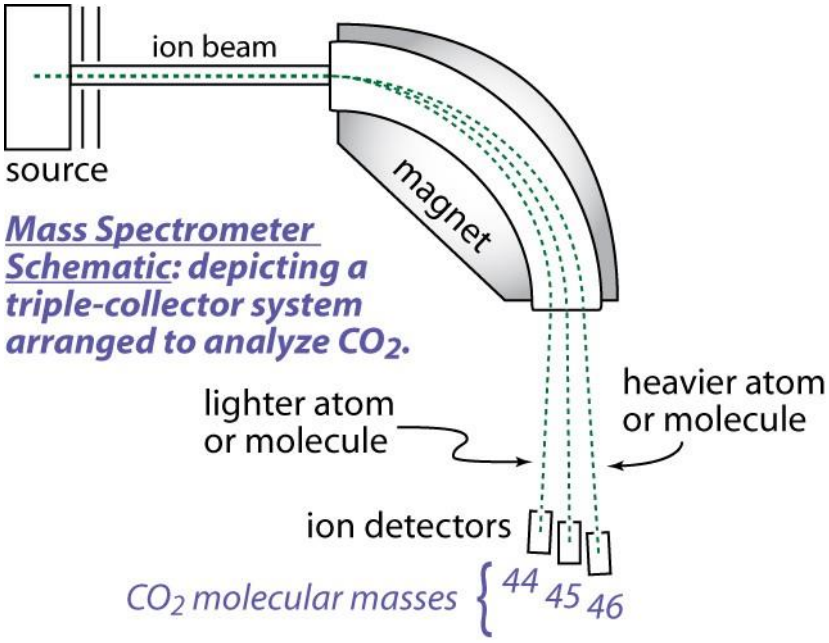

Figure 4.3: Simplified schematic illustration of a mass spectrometer positioned to analyze CO_2 (Dunn, 2008)

Attached to the mass spectrometer is a Kiel IV device, a carbonate preparation system that allows generation of CO_2 gas, which is directly injected into the mass spectrometer. The CO_2 gas is produce when the carbonate ($CaCO_3$) samples and standards (Chapter 4.2.5), react with 100% phosphoric acid (H_3PO_4) at 70°C, a method developed by McCrea (1950).

$$CaCO_3 + H_3PO_4 \Leftrightarrow CaHPO_4 + CO_2 + H_2O \qquad \text{Equation 4.2 (McCrea, 1950)}$$

A small amount of the CO_2 gas is admitted into the mass spectrometer via a sample capillary which is crimped at the end to ensure viscous flow regime and avoid kinetic fractionation. McCreas equation shows that all the carbon is converted to CO_2, hence $\delta^{13}C$ can be measured directly, whilst only 2/3 of the oxygen content is converted to CO_2. Since the fractionation is constant at a set temperature, it can be corrected for if the temperature is constant (Clark & Fritz, 1997). Any residual water is removed from the sample gas by passing it through a tube kept at -80°C through the use of liquid nitrogen. In the vacuum chamber the CO_2 gas molecules are ionized by bombardment with electrons. The ions produced are accelerated by a high voltage electric field to create a beam of ions. The magnetic field deflects the ions proportionally to the masses of the

isotopes; thus, the lighter isotopes are deflected more than the heavier ones. Because of a grounded slit plate in front of the collector, the ion beam will be separated before continuing through the analyzer tube to the collector. The collector consists of a Faraday cup where the positive charge is converted to a current and transmitted to a resistor where the current is measured by a voltmeter. The resulting signal from each stream of separated ions will represent a mass-to charge ration that will identify the relative abundance of each isotope (Faure & Mensing, 2005). The final $\delta^{18}O$ and $\delta^{13}C$ values are given in ‰ relative to the VPDB standard. This reaction creates a reproducible and consistent result at a given temperature

4.3 Foraminifera

Foraminifera are single-celled eukaryotic organisms, belonging to the Phylum Protozoa. Most foraminifera are marine, either living on the bottom of the ocean (benthic) or floating in the water column (planktic). Foraminifera are found in large quantities, over wide spread areas and in many places. Foraminifera form a significant component of the sea-floor sediment (Schiebel, 2002), above the calcium carbonate compensation depth (CCD) which is at ~4,500 m depth, with some variation between and within ocean basins (Coxall et al., 2005). Many secrete a test (or shell) made of calcium carbonate (CaCO3) where the incorporated oxygen and carbon isotopes stem from the surrounding water masses. Foraminifera are preserved after death in the marine sediment, and their isotopic values can be extracted in order to reconstruct the chemical and physical seawater properties at the time the foraminifera lived.

Not all marine species secrete shells that are in equilibrium with the seawater. Vital effects, as a label for deviation from equilibrium, may occur in some species. Vital effect is thought to be a consequence of incorporation of isotopically-light carbon-oxygen compounds derived from the metabolic CO_2 pool within the organism into the test. Generally this produce a ^{13}C and $^{18}0$ depletions in the shell composition (Bauch et al.,1997). In this study, one planktic and two benthic species are used for stable isotope measurements. Their vital effect is regarded as being fairly systematic and thus is consistent and unlikely to drive significant variability in the downcore record
(Zahn et al., 1986).

4.3.1 Planktic foraminifera

Planktic foraminifera live floating in the photic zone, relatively near the surface (upper 200m). Their sensitivity to physical and biological changes in the environment, make planktic foraminifera ideal as indicators of past oceanography and climate. Because of their consistent presence during glacial and interglacial times in subpolar and polar environments, the following planktic species are used in this paleoceanographic study:

<u>*Neogloboquadrina Pachyderma*</u>

N. Pachyderma (Figure 4.4) coil their chambers either in dextral (right) or sinstral (left) direction, seemingly dependent upon temperature (Ericson, 1959). The dextral form is dominant in temperate and sub-polar regions, while the left-coiling specimens *N. pachyderma* (s) is dominant in polar waters at both hemispheres (Niebler et al.,1999), and is the one selected for this study.

Figure 4.4: *N. pachyderma* (s) Scale Bar = 20µm

Blooming of *N. pachyderma* (s) takes place over few weeks during summer (December and January) and almost non existent during periods of ice cover (Kohfeld et al., 1996). The shell flux is controlled by absolute sea surface temperature, seasonal stratification of the upper water column, salinity, insolation and food availability (Jonkers et al., 2010). In the Antarctic Ocean, the species displays its highest frequencies between 1 and 5°C, with reported minimum temperatures of -1.4°C and a minimum salinity of 30‰ (Boltovsky & Wright, 1976). The depth at which the species thrive is not exactly known (Donner &

Wefer, 1994), however they appear most abundantly in the upper 50 to 100 m, and most calcification occur at depths ranging from 100 to 200 m (Bauch et al., 1997). N. *pachyderma* (s) is thus living in different water masses at different depths, highly dependent on water mass distribution (Bauch et al., 1997), this can create a intraspecific genotypic variation within and between water masses (Darling et al., 2006). The small intraspecies $\delta^{18}O$ variability of 0.4‰ (Berger et al., 1978) can be further reduced in significance by preferentially selecting from a narrow size fraction (212-250μm) of *N. pachyderma* (s) specimens.

Even though it is difficult to specify average depth of habitat in the water column *N. pachyderma* (s) records an integrated $\delta^{18}0$ signal for the upper water column and not just the uppermost surface, which is more sensitive to regional or seasonal signals. It is the mixed layer and upper water column habitat that makes this species an ideal indicator for water mass variability.

4.3.2 Benthic foraminifera

Benthic foraminifera acts as tracers for the physical and chemical composition of the ocean and local environmental geochemical conditions. This allows the reconstruction of bottom water age (and ventilation), water mass properties, and productivity which is reflected in the flux of carbon into the sediment. Benthic foraminifera are ocean bottom dwelling organisms living in all marine environments, above (epifaunal) or within the sediment (infaunal). The habitat of the benthic species must be considered before stable isotope analysis, due to the significant contrast between epifaunal foraminifera living in the well-oxygenated water-sediment interface and the infaunal foraminifera deeper in the sediment (Jorissen, 1999). The deep ocean is in general a stable environment, particularly in terms of physio-chemical properties such as temperature and salinity. Thus benthic isotopic values generally show smaller intra-species and downcore fluctuations than the planktic isotopes.

Two benthic species are analyzed for stable isotopes in this study. Figure 4.5 show the $\delta^{13}C$ value of these two benthic species in compared to the dissolved inorganic carbon (DIC) in the ocean.

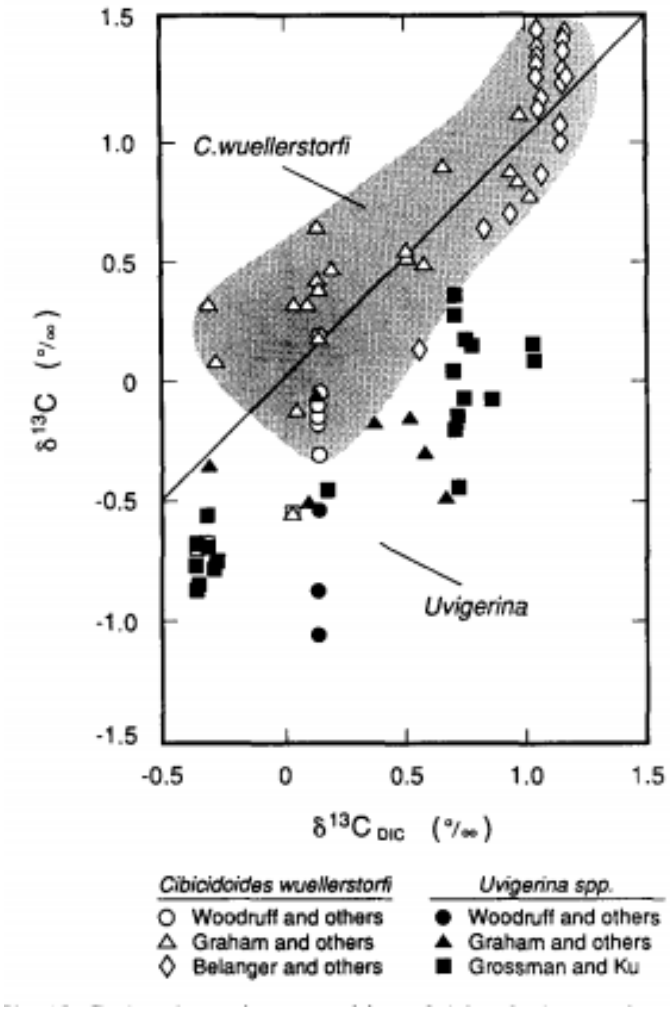

Figure 4.5: Carbon isotopic composition of C. *wuellerstorfi* and U. *peregrina* as a function of the $\delta^{13}C$ of dissolved inorganic carbon (DIC) in the ocean. The line represents a 1:1 correspondence (Grossman, 1987; Wefer & Berger, 1991).

Cibicidoides wuellerstorfi (Schwager 1866)

The disc shaped *C. wuellerstorfi* (Figure 4.6), one of the most common deep sea benthic foraminifera, prefer to live in an epifaunal habitat on or above the sediment surface. Its test is therefore assumed to faithfully record the isotopic composition of the ambient bottom water, without influence from sediment pore water chemistry (Wefer & Berger, 1991), and large scale variations of total dissolved CO_2 in the bottom water mass (Duplessy et al., 1984). However, $\delta^{13}C$ values of *C. wuellerstorfi* shells may not always precisely mirror bottom water $\delta^{13}C_{DIC}$ values. In highly productive areas, a pulsed phytodetritus supply to the sediment–water interface can cause a significant impact on the $\delta^{13}C$ (Mackensen et al., 1993). The oxygen isotopic composition of *C. wuellerstorfi* is

not in equilibrium with the ambient bottom water, but shows a constant offset from equilibrium calcite by 0.64‰ (Shackleton & Opdyke, 1973) a value widely used as a correction factor for inter-species comparisons (Bauch et al., 1997). Knowledge about the deep ocean environment is thus crucial in analyzing benthic foraminifera.

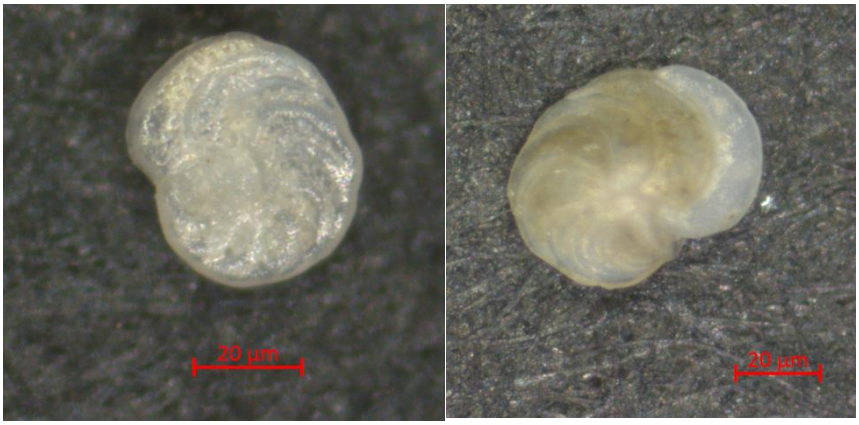

Figure 4.6: *C. wuellerstorfi.* Scale Bar = 20µm

Uvigerina peregrina (d'Orbigny, 1826)

U. peregrina (Figure 4.7) preferentially occupies a shallow infaunal habitat (Jorissen, 1999). Because of its shallow infaunal habitat, it reflects the conditions of the pore water rather than the actual bottom water. The pore water is greatly influenced by the sedimentation of organic substances and exhibit a rapid $\delta^{13}C$ depletion with depth in the sediment (Grossman, 1987). Foraminifera calcifying in the pore water will mirror this depletion and incorporate the "microhabitat effect" (Fontanier et al., 2006). In Figure 4.6 the U. *peregrina* points are plotted with greater scatter towards lighter $\delta^{13}C$. The "microhabitat effect" might be one explanation or a greater sensitivity to variations in nutrient supply for this species (Zahn et al., 1986) or vital effects.

Grossman (1987) showed that the $\delta^{18}O$ values of samples of *U. peregrina* taken at different depths were as expected according to paleotemperature. Further studies by Fontanier et al. (2006) show no systematic relationship between the foraminiferal microhabitat depth and the $\Delta\delta^{18}O$ between foraminiferal and equilibrium calcite. The difference is reflecting increasing thermodynamic fractionation in sync with decreasing temperatures. Uvigerina taxa incorporate stable oxygen isotopes in their shell in near-equilibrium with ambient sea water and has therefore been frequently used to construct marine oxygen isotope records (Shackleton, 1974).

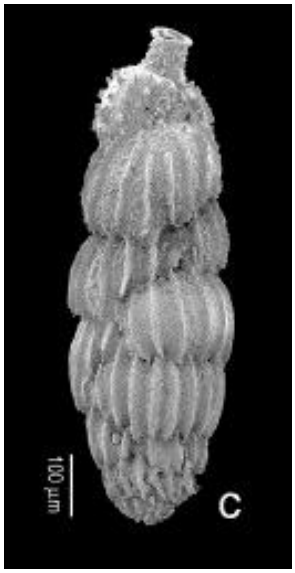

Figure 4.7: *U. peregrina.* Scale Bar = 100µm (Schweizer et al., 2005)

4.4 Ice-rafted debris

If sand size lithic grains or gravel is found in the same area as fine sediment in the open ocean then these are indicators of ice rafted debris (IRD) (Scherer, 1991). Debris, which is embedded in the ice sheet, is transported to the ocean by the extended ice shelf or sea ice and through icebergs that break off from ice margins and into the ocean. The floating ice shelf, sea ice and drifting icebergs will melt when they come in contact with warmer waters, and the IRD will rain down the water column and settle on the ocean floor as IRD deposits or layers, as illustrated in Figure 4.8.

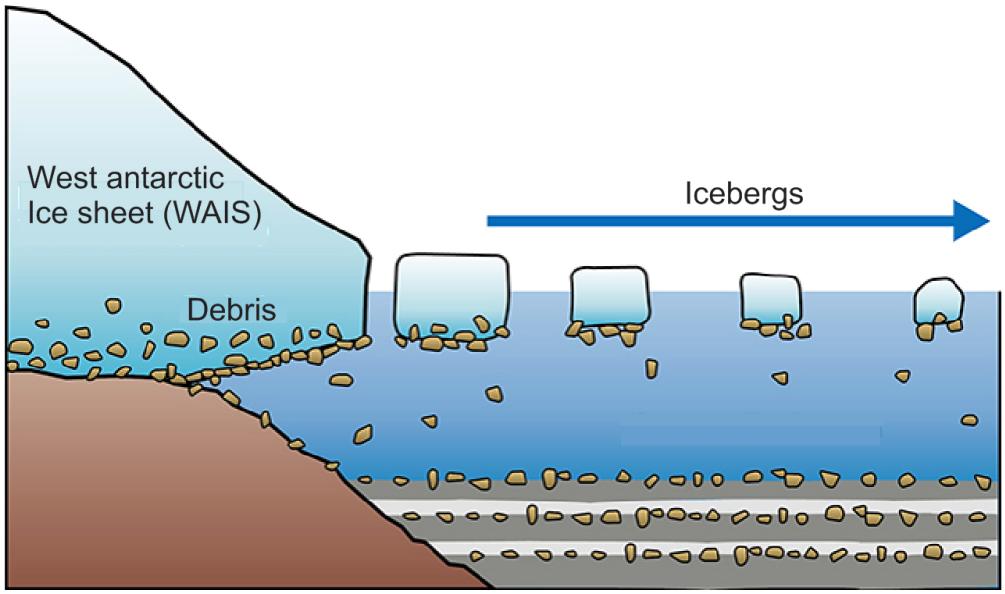

Figure 4.8: Illustration explaining the dynamics of IRD accumulating on the seafloor (modified after (JAMSTEC, 2014)).

IRD in sediment cores provide a nearly continuous signal of ice-sheet variability and dynamics. However there are several ways in which IRD are deposited. Ice rafting occur both when there is cooling and the ice sheet expands and when there is warming, with a lot of melt and ice sheet instability. The distance from where the calving takes place to the location of deposition give information of the survival time of the iceberg, which is dependent upon surface ocean temperature and ocean circulation. With a distant core position, it can be difficult to differentiate an increasing amount of IRD caused by higher amount of iceberg rafting due to ice sheet instabilities or a longer survival time of the iceberg due to water mass temperature or ocean circulation.

IRD research became of major interest when Grossman (1987) proposed that massive discharge of icebergs was a characteristic element of abrupt millennial climate events during 14,000 and 70,000 years ago. Climate events with IRD layers up to a meter in thickness have been termed Heinrich events after Hartmut Heinrich, who in 1988 published an article on a curious set of sedimentary layers in cores from the eastern North Atlantic (Heinrich, 1988). The repeated cycles of IRD deposits, Heinrich layers, put attention to the coupling of surges in ice sheets, iceberg armadas and climate responses (Bond et al., 1992; Broecker, 1994).

IRD reconstructions have been carried out to a larger extent in the Northern Hemisphere (Bond et al., 1992; Broecker, 1994) than in the southern hemisphere because of the low resolution and large dating uncertainties in existing sediment cores (Kanfoush et al., 2000; Hodell et al., 2001; Weber et al., 2014). If the age and the quantity of these deposits on the seabed are known, it is possible to reconstruct the quantity of melting icebergs in the area. The source area can be determined on the basis of geochemical evidence from volcanic ash settled on grounded-ice shelves or sea ice and trough mineralogy (Smith et al., 1983). This thesis will contribute to the IRD research in the southern hemisphere by studying a high resolution, well dated core.

4.5 Stable isotopes

Stable isotope ratios constitute a long established method in paleoclimatology to reconstruct past oceanographic and climate parameters. The nuclei of an atom consist of protons and neutrons. The number of protons is fixed for each element, but the quantity of neutrons can vary creating isotopes of the atom. Isotopes have the same basic chemistry, but different physical properties according to the number of neutrons, which alters its mass. Isotopes are considered stable unless they are radioactive (undergo decay).

In principle, molecules comprised of light isotopes react more easily than those composed of heavier isotopes. This is because molecules with a heavy isotope have marginally greater covalent bond strengths and lower vibrational frequencies than their lighter counterparts, making them slightly less reactive (Ruddiman, 1977).

The isotope ratio, R, is defined as the abundance of the heavier isotope over the abundance of the lighter isotope:

$$R = \frac{Abundance\ of\ rare\ (heavy) isotope}{Abundance\ of\ abundant\ (light) isotope} \qquad \text{Equation 4.3}$$

The partitioning of isotopes during natural physical, chemical or biochemical processes, such as during transpiration, metabolism, evaporation and condensation is called

fractionation. If R_A and R_B are the heavy/light ratios for any two isotopes in exchanging chemical compounds A and B, then the fractionation factor (α) can be defined as:

$$\alpha_{A\text{-}B} = R_A / R_B \qquad \text{Equation 4.4 (Rohling \& Cooke, 1999)}$$

In general are isotope effects small (α≈1), therefore the deviation of α (usually given in ‰) form 1 is normally used rather than the fractionation factor itself. The main phenomena producing fractionation are:

1. Isotopic exchange reactions between phases that are in equilibrium, known as "equilibrium isotope fractionation" which is strongly temperature dependent.
2. Kinetic effects which cause deviation from equilibrium, due to different rates of reaction for the different isotope species (Bigeleisen, 1965).

The stable isotope $^{18}O/^{16}O$ ratios in the biogenic calcite are a function of the ratio in the seawater and the calcification temperature (Rohling & Cooke, 1999). In contrast to $^{13}C/^{12}C$ ratios which are controlled by the ratio of dissolved inorganic carbon in seawater and physiological processes like respiration and symbiotic photosynthesis (Rohling & Cooke, 1999). These geochemical proxies have been used with analyses of foraminifera shells to reconstruct surface and bottom ocean temperatures, ocean circulation changes, global ice volume and glacial-interglacial exchange between the oceanic and terrestrial carbon sinks.

4.5.1 Oxygen isotopes

There are three stable isotopes of oxygen: ^{16}O, ^{17}O and ^{18}O, with natural abundance of 99.757%, 0.038%, and 0.205%, respectively (Epstein et al.,1953). The normal procedure is to measure the ratio of ^{18}O to ^{16}O, based on their higher abundance and the greater mass difference. The absolute abundance of minor isotopes such as ^{18}O, or the value of the isotopic ratio, is exceedingly difficult to determine accurately. The oxygen isotope ratio is therefore commonly quoted as deviations (delta values) from the oxygen isotope ratio ($\delta^{18}O$) of a reference sample or standard substance in per mil (‰).

$$\delta^{18}O_{(sample)} = \frac{^{18}O/^{16}O_{(sample)} - {}^{18}O/^{16}O_{(standard)}}{^{18}O/^{16}O_{(standard)}} \times 1000$$ Equation 4.5 (Ruddiman, 2008)

The measurement of oxygen isotope ratios of biogenic calcite is one of the most established and commonly used of all proxies in climatology. Many organisms create calcite skeletons, which incorporate the geochemistry of the seawater. Foraminifera are most frequently used in marine stable isotope analyzes because of their abundance and diversity in marine sediments. The oxygen isotope ratio of seawater is closely linked with the fractionation processes within the hydrological cycle, which include evaporation, atmospheric vapor transport, precipitation, storage in aquifers and the subsequent return of freshwater to the ocean via precipitation, rivers and iceberg melting (Figure 4.9) (Shackleton & Opdyke, 1973).

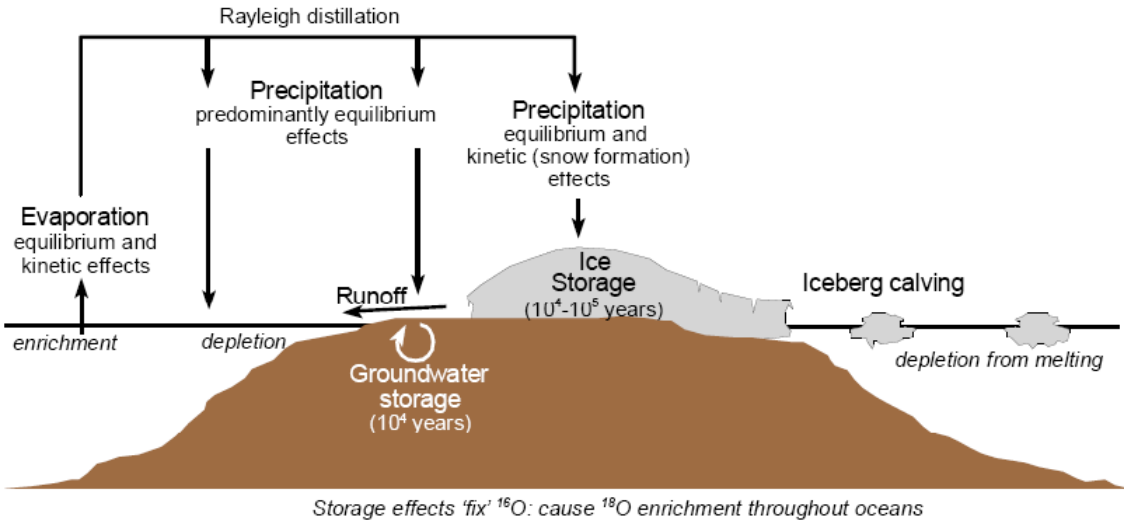

Figure 4.9: Illustration showing the influence of the hydrological cycle on oxygen isotope ratios (Rohling, 1999; Rohling, 2007)

During evaporation, the lighter isotope ^{16}O is preferentially removed. If this precipitate at higher latitudes and is stored as ice then the ocean will get depleted in ^{16}O, giving a positive $\delta^{18}O$ value of seawater when ice sheet grows. Foraminiferal $\delta^{18}O$ is in this way a influenced by global ice volume in continental ice sheets called "glacial effect", in addition to temperature (Rosman & Taylor, 1998). The isotopic composition of marine carbonates is not only dependent on temperature and the magnitude of glacial effect. Evaporation-

precipitation patterns which will affect the salinity (and local variations in water $\delta^{18}O$), the vital effect, temperature selectivity and differential dissolution are parameters that can complicate estimates of paleotemperature (Rohling & Cooke, 1999).

Harold Urey and his group at University of Chicago first proposed the use of stable oxygen isotopic measurements from calcareous shells as a proxy for reconstructing paleotemperature (Urey, 1947). Urey's postdoctoral associate Samuel Epstein and colleagues continued his studies by establishing the relationship between temperature and ^{18}O content relative to that for a PDB standard in an empirically derived paleotemperature equation.

$$T\ (°C) = 16.5 - 4.3\delta + 0.14\delta^2 \qquad \text{Equation 4.6 (Epstein et al., 1953)}$$

Where δ is the difference in per mil of the $^{18}O/^{16}O$ ratio between isotopic composition of the sample and the isotopic composition of the water masses. Epstein´s equation 4.6 is based on the assumption that foraminifera are precipitated in chemical equilibrium with the surrounding seawater and that the composition of the seawater is known, which is only true for the present. In fossil samples, the isotopic composition has altered through time, mainly due to the glacial effect but also other deviations like the temperature, salinity and differential dissolutions needs to be taken into consideration (Urey, 1947).

4.5.2 Carbon isotopes

Of the three naturally occurring isotopes of carbon about 98.9 % is ^{12}C, 1.1 % is ^{13}C and only a very small amount of the radioactive ^{14}C. Variations in the relative amount of the two stable isotopes of carbon (^{12}C and ^{13}C) are an established proxy in paleoceanography for depicting changes in paleoproductivity, exchange between the oceanic and terrestrial carbon pools, and water mass movements in the geologic record. As with oxygen isotopes, carbon isotope ratios are reported as the ratio of heavy to light isotope and its deviation relative to a standard;

$$\delta_{^{13}C}‰ = \frac{^{13}C/^{12}C_{sam} - {}^{13}C/^{12}C_{std}}{^{13}C/^{12}C_{std}} \times 1000 \qquad \text{Equation 4.7}$$

The distribution of $\delta^{13}C$ in the ocean is controlled by photosynthesis, remineralization of organic carbon and through mixing between water masses of different isotopic composition (Epstein et al., 1953). Carbon isotope analysis of planktic foraminifera provide key information on former productivity variations in the oceans upper layers and on the export flux of ^{12}C from the photic zone. Furthermore, has productivity an impact on and are affected by the turnover of oceanic and atmospheric CO_2. Plant plankton in the photic zone, extracts dissolved inorganic carbon (DIC) from CO2 in the ambient water to form organic carbon in their organic tissue (CH2O) through photosynthesis.

$$CO_2 + H_2O + \text{energy (sunlight)} \rightarrow CH_2O + O^2 \qquad \text{Equation 4.8}$$

Photosynthesis preferentially removes the lighter isotope, which is more weakly bonded and reacts more readily, from the surface ocean, leaving the ocean carbon pool (DIC) with more positive $\delta^{13}C$ values. When the organic matter dies and sinks through the water column it dissolves (or oxidizes) into inorganic carbon. The eventual remineralization and release of ^{12}C into the deep ocean, creates a $\delta^{13}C$ depletion in deeper waters (Rohling & Cooke, 1999).

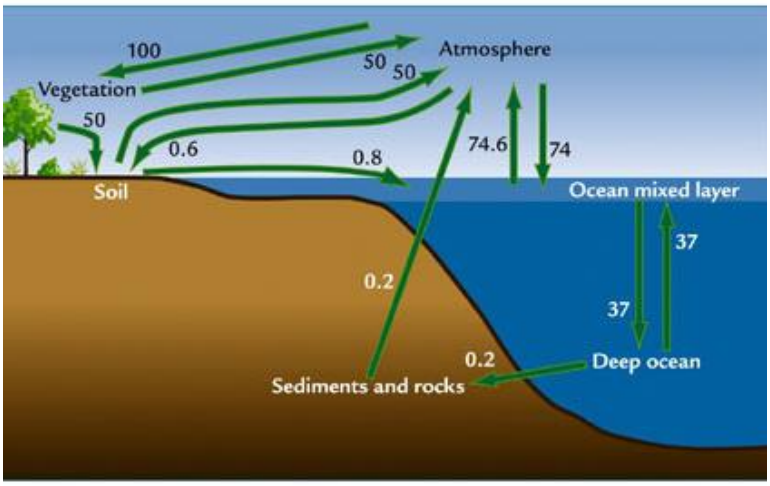

Figure 4.10: The Carbon Cycle exchange (Ruddiman, 2008)

Remineralization at depth releases not only ^{13}C depleted CO_2, but also nutrients into deep water (Curry et al., 1988). Whenever the $\delta^{13}C$ value decreases, the amount of nutrients increases, and vice versa.

The deep water $\delta^{13}C$ reflect the time of exposure, the amount and the rapidity of organic matter decay, which shows true age, export productivity along its pathway and respiration rate (temperature dependent) respectively. This can trace the history of the deep water from its source area and give a relative concept of age, providing a tool for reconstruction of ocean circulation.

Varying degrees of photosynthesis in the polar oceans lead to different inorganic carbon $\delta^{13}C$ values in Arctic versus Antarctic waters. North Atlantic deep water (NADW) is formed from surface waters that have been enriched in ^{13}C by photosynthetic removal of ^{12}C in the tropics and subtropics before it sinks in the Nordic Seas. NADW is the most nutrient depleted deep water mass of the ocean, with $\delta^{13}C$ values in the range of 1.0 – 1.4‰ (Ruddiman, 2008). On the other hand, the Antarctic deep water masses have $\delta^{13}C$ values under 0.5‰, because photosynthetic fractionation does not complete in the Southern Ocean (Rohling & Cooke, 1999).

Carbon isotopes have similar limitations to those of oxygen isotope. For example, variations in carbon isotope content between foraminifera due to fractionation as a result of differential vital effects and regional variations caused by localized circulation changes. Commonly, the $\delta^{13}C$ values observed are much more negative than the $\delta^{13}C$ values calculated from equilibrium with the dissolved inorganic carbon in the surrounding water. Foraminifera shift to low $\delta^{13}C$ during productive periods. However, several benthic foraminifera appear to record $\delta^{13}C$ of the surrounding water faithfully (Curry et al., 1988).

Biological, ecological and geochemical processes complicate carbon isotopes. Foraminifers are subject to alterations by microhabitat environments in porewater, respiration and photosynthesis in symbionts that all influence the $\delta^{13}C$ signal as well as $\delta^{18}O$ (Ruddiman, 2008).

5 Chronology

To determine the rate and timing of the observed variability it is essential to establish a correct age model. Additionally, placing the GS08 -151-02 proxy records on a time scale allows comparisons with paleoceanographic reconstructions from other regions and their timing and duration of observed events. The chronology in this study, utilise radiocarbon dating.

5.1 AMS ^{14}C dating

Radiocarbon dating is one of the most widely used late Quaternary dating methods. Natural, unstable radiocarbon (^{14}C) is produced in the atmosphere from cosmic ray bombardment of molecular nitrogen (N_2) (Wefer & Berger, 1991). The ^{14}C is rapidly oxidized and forms a particular carbon dioxide that gets mixed in the atmosphere and absorbed by the ocean and living organisms through photosynthesis and respiration. As long as the organisms are alive, their new tissue will broadly reflect the atmospheric content of ^{14}C. Upon the organisms death, ^{14}C in the organic tissue will continue to decay to a stable form of nitrogen, ^{14}N, through the emission of beta β particles, without any substitutions or exchanges taking place (Cronin, 2009).

$$^{14}CO_2 \rightarrow {}^{14}NO_2 + \beta$$

Radioactive decay is time dependent, and the half-life of radiocarbon was originally found to be 5568± 30 years by Libby (1949) but today we use the more accurate "Cambridge" half-life with a figure of 5730 ± 40 years (Libby et al., 1961). This means that the residual ^{14}C of fossil material can be used to date material back to a maximum of 50 000 years. In this study I use the accelerator mass spectrometry (AMS) method. AMS is based on the same basic principles as regular mass spectrometry (see chapter 4.2.6), the difference is that AMS can discriminate between ^{14}C and other elements of similar weight. This is done by subjecting the particles to large voltage differences so that they travel at very high speed and the small ^{14}C signal can be separated and detected (Lowe & walker, 2014).

5.1.1 Sources of error in ^{14}C dating

A radiocarbon "date", the age of the carbon in the marine organism is not necessarily the age of the material itself and will depart from normal calendar age for several reasons. The first being the assumption that atmospheric ^{14}C has been constant through time. This is not correct, the production rate of atmospheric ^{14}C varies according to the intensity of solar activity and changes in the solar and earth's magnetic field (Walker & Walker, 2005). Also, changes in the deep ocean circulation and uptake by the ocean, nuclear bombing and burning of fossil fuels (known as the "Suess effect") influence the production rate. These changes must be computed and factored into standard calibration curves in order to accurately convert measured ^{14}C to calendar dates (Lowe & walker, 1984).

Secondly the "reservoir effect" causes the radiocarbon age to deviate from calendar age because different carbon reservoirs may not be in isotopic equilibrium with the atmosphere. ^{14}C becomes incorporated into sea water as dissolved carbonate in the surface. When the surface water sinks the ^{14}C will start to decay without replenishment from the surface giving the sea water an apparent age or reservoir age. The global average marine reservoir age of surface water is 400 ^{14}C years. However, the aging effect varies from tens to hundreds of radiocarbon years regionally as a function of changes in water mass distribution and climate. Deep ocean water is one of the slowest-responding parts of the climate system. On average it takes more than 1000 years for a unit of water to sink from the surface into the deep ocean and to emerge back at the surface. The Atlantic Ocean has younger, faster moving water than the Pacific Ocean (Stuiver & Quay, 1980). The reservoir age also tend to be greater in polar waters where CO_2 exchange is highly reduced in ice-covered regions and where ^{14}C depleted deep water rises in the upwelling area compared to in equatorial waters (Fairbanks et al., 2005).

This means that the reservoir age must be added to the ^{14}C ages from deep-ocean cores, with different correction factors being applied to planktic and benthic species in order to derive a common time scale between terrestrial and marine organic material.

5.2 Calibration and age models

Five samples of *N. pachyderma* (s.) from core GS08-151- 02MC A were sent to Leibniz Labor für Altersbestimmung und Isotopenforschung in Kiel, Germany for AMS dating (Table 5.1). All the samples gave enough carbon and produced sufficient ion beam during the AMS measurement. The $\delta^{13}C$ values are in the normal range for marine carbonates and insofar the results are reliable. Unfortunately, sample KIA 46264 (depth: 12cm) produced graphite of bad quality leading to a more positive $\delta^{13}C$ value than usual. This indicates that fractionation has taken place and, thus, the result should be considered as not reliable.

The chronology of radiocarbon dates in Antarctica depends upon the assumption of a large reservoir correction (about 1200 yr) (Gordon & Harkness, 1992). A recent study of whale-bones from the South Georgia Island (54°17′S 36°30′W) is consistent with a minimum reservoir age of 1060 ± 25 years (Ninnemann, Pers. Comm. Work in preparation from the IPY Paleodrake project). The core site is situated close to South Georgia Island hence a 1060 yr reservoir age is applied when calibrating the core (delta R = 660). AMS measurements produce ages in "radiocarbon years", which must be converted to calendar ages by a process called calibration. For this purpose, the four AMS ^{14}C dates are calibrated using the Marine 13 calibration curve (Reimer et al., 2013) and the age-depth model of the core GS08-151- 02MC A is constructed using a cubic spline curve through the AMS ^{14}C dates calculated at ± 1σ confidence ranges using the age-depth modelling software “CLAM” (Blaauw, 2010), operated through the open-source statistical software “R” (R Core Team, 2013) (Figure 5.1).

Table 5.1 Results of Radiocarbon dating

Lab code [a]	Core depth (cm)	Species [b]	Uncorrected ^{14}C age (yr) ± 1 σ error	Calibrated Age [c] (cal. Yr. BP)	Age range (± 1σ error)
KIA36412	0	Nps	1175± 30 BP	143	11-275
KIA46263	6	Nps	1665 ± 25 BP	587	527-647
KIA46264	12	Nps	1595 BP*		
KIA46265	18	Nps	3055 ± 30 BP	2028	1934-2117
KIA36413	24	Nps	4625±35	3963	3847-4079

[a] KIA – Leibniz Labor für Altersbestimmung und Isotopenforschung, Kiel, Germany
[b] Nps – *Neogloboquadrina pachyderma* (sinistral)
[c] ^{14}C ages were converted into calendar ages with the CLAM 2.2 software (Blaauw, 2010) and the MARINE13 (Reimer et al., 2013) calibration curve, applying a 1060a reservoir age correction.
*not reliable

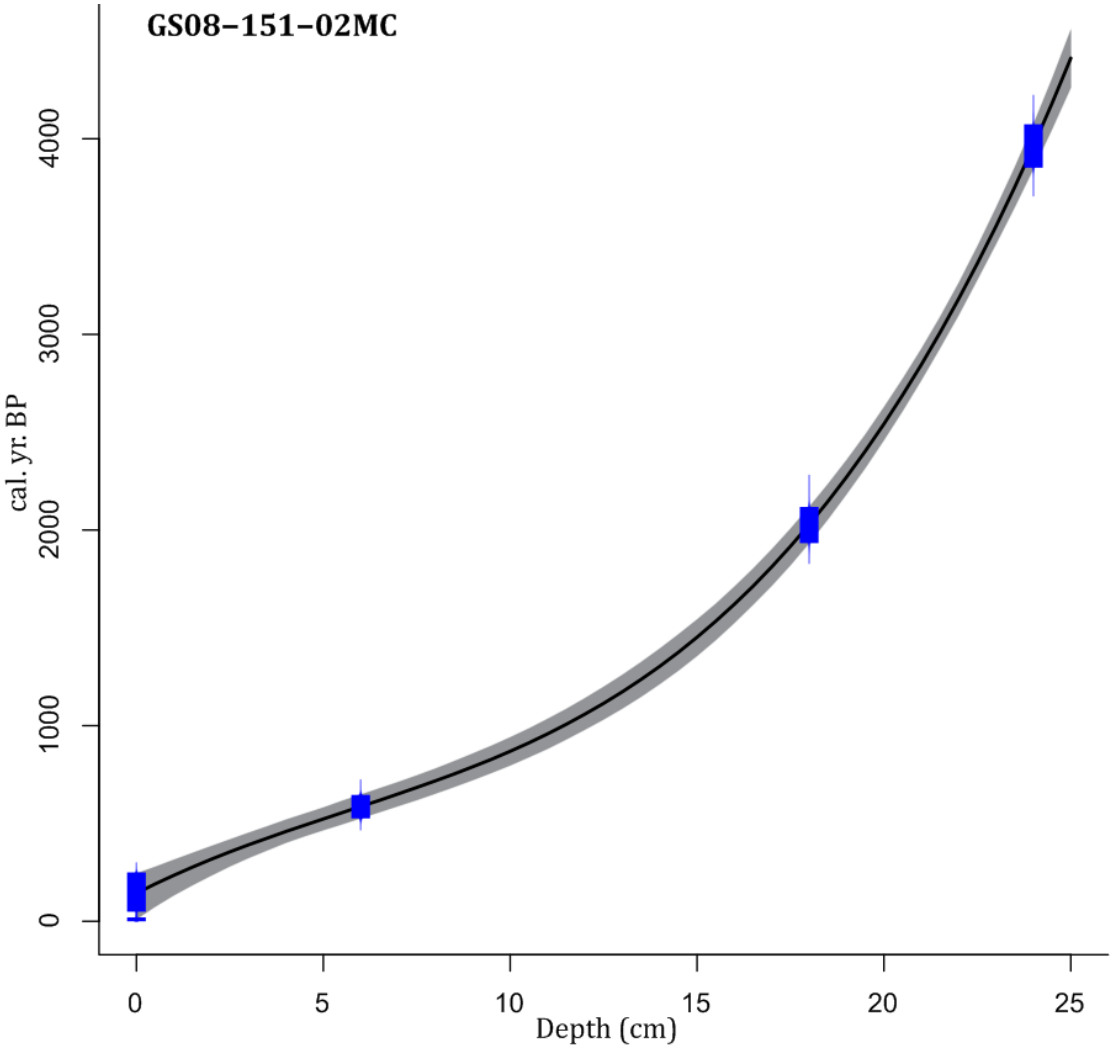

Figure 5.1: Age-depth model for core GS08-151- 02MC A is based on four radiocarbon dates and reconstructed using the software CLAM 2.2 (Blaauw, 2010), using a cubic spline fit between the calibrated dating points plotted with ± 1 σ confidence intervals (gray shading). The black line provides the best fit between the dated points, where the blue color donates the AMS ^{14}C dates. The blue rectangles denote ±1σ age range based upon the Marine 13 calibration curve for the ^{14}C dates.

5.3 Sedimentation rate

Based on the constructed age model, the sedimentation rate for the core is calculated using spline to be on average 5.86 cm/kyr. This corresponds to an average time resolution for every 0.5 cm sample interval of ~80yrs/0.5cm. The younger part of the core exhibit the highest sedimentation rate of 13.5cm/kyr. Meaning that every sample taken of the topmost 6 cm have a resolution of (only) 37 years.

6 Results

In this study, I reconstruct the sequence of regional ocean properties through the late Holocene (the last ~ 4200 years), spanning the Little Ice Age (LIA) and much of the Neoglacial, using the oxygen and carbon isotope composition of planktic and benthic foraminifera of northern Scotia Sea sediments.

In the following subchapters, the results from iceberg rafted debris counts and the oxygen and carbon isotope measurements from the planktic and the benthic foraminifera are presented separately and plotted versus depth and age, using the age model described in the previous chapter. The oxygen and carbon isotope values in the text and all figures are given in per mille (‰) relative to the VPDB standard. All IRD counts and isotope analyses, together with replicates, are listed in Appendix A-C.

6.1 Iceberg rafted debris (IRD)

Iceberg rafted debris (IRD) records reflect the variability of icebergs being transported across a core site. According to William F. Ruddiman (1977), the amount of drifting glacial ice is coupled to the growth and decay of ice sheets. The IRD records obtained from core GS08-151-02MC (0-25 cm) (53° 31.813 S; 44° 42.143 W) span the time interval from pre-industrial time 150 yr BP and back to the neoglacial around 4200 yr BP. In the hypsithermal, prior to the neoglacial (~5000 yr BP) there were relatively small amounts of IRD reaching 53°S due to February SST exceeding 4°C (Deevey & Flint, 1957), which is considered the limit of iceberg survival. The IRD signal is not simply a dynamics signal, but must be put in context with regional climate as well. To distinguish what drives the IRD signal is complex, and will be discussed further in Chapter 7.

Bond and Lotti (1995) suggested that lithic concentrations (grains/g) indicate ice-rafting events better than lithic percentages. Thus, results are expressed as grains of IRD per gram of dry sediment for each individual sample (Appendix A).

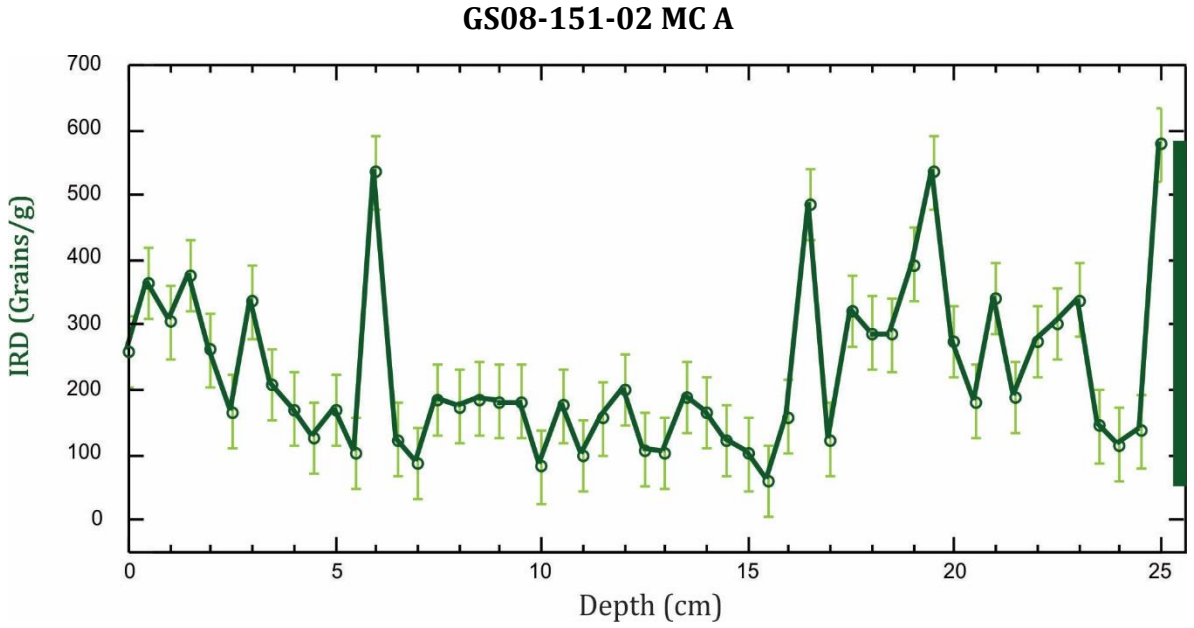

Figure 6.1: IRD (grains/g) record plotted against core depth (cm). Error bars (light green) denote the standard deviation (±56 grains/g) from the mean of the pooled replicated measurements. The green bar illustrates the full range of variability.

Figure 6.1 shows counts of IRD from every sample with a 0.5 cm spacing depth interval (green circle), with duplicate counts carried out for every 4 cm. The error bars are denoted to the standard deviation from the mean of the pooled replicated measurements and calculated to of ±56 grains/g. As the site is located on the northern margin of the iceberg alley it may be near the outer fringes of iceberg survival (reference to chapter 3.2.4). Thus, while there is significant IRD at the core site, ranging from 60 to 577 grains/g (green bar), the input of IRD to the site may not be as high as in more southerly, or central, regions of the iceberg alley. Nevertheless, IRD is present and although changes are small, they are significant relative to the uncertainty in the counts (±56 grains/g). Four significant peaks are recognized at 6 cm, 16.5 cm, 19.5 cm and 25cm.

However, in order to place the IRD record in a scientific timing of the observed changes and make comparisons with regional paleoclimatic records, IRD must be plotted against calendar age (yr BP), with calibrated ages from the GS08-151-02 age model (Chapter 5) (Figure 6.2).

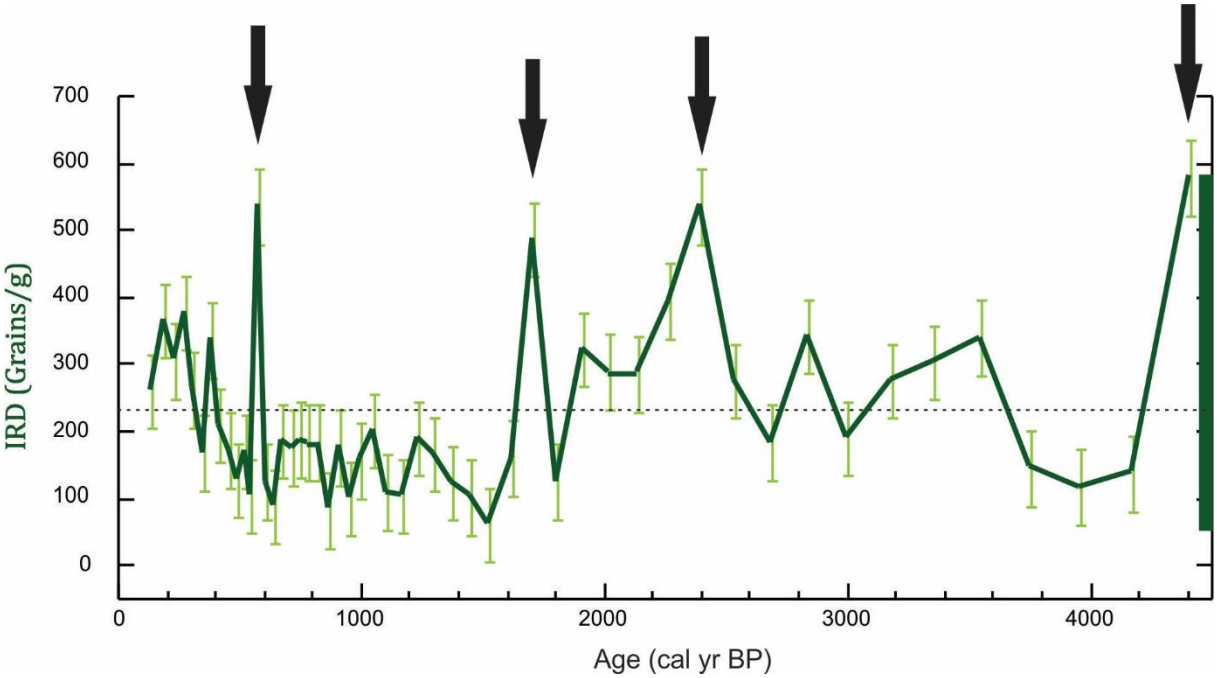

Figure 6.2: IRD grains per gram record (dark green curve) from core GS08-151-02MC. Each 0.5 cm core depth interval is plotted versus age. The light green error bars (±56 grains/g) are denoted to the average standard deviation from the mean of the replicated measurements. The green bar illustrates the range of variability. The dashed line is denoted to the average IRD amount (226 grains/g).

The most prominent features in the IRD record are the abrupt increases in IRD abundance occurring at four individual peaks (black arrows). With the calibrated ages, these events falls at 587, 1700, 2403, 4412 yr BP. The first peak at 4412 yr BP has the highest registered IRD followed by a minima interval between 4200 and 3750 yr BP. Generally, there is higher IRD content than the mean (dashed line), in the first half of the record prior to 1800 yr BP. Following the third IRD peak at around 1700 yr BP the IRD decreased to a minimum of 60 grains/g and remained low until the short IRD peak again at around 587 yr BP. After recovering back to near minimum values the amount IRD then increased toward the core top (140 yr BP).

6.2 Oxygen isotope results

The $\delta^{18}O$ signal reflects seawater physical property changes (i.e. temperature and salinity) in the Scotia Sea. The $\delta^{18}O$ signal can be used to calculate relative changes in temperature by using the paleotemperature equation 4.5 by Epstein et al. (1953) (Subchapter 4.5.1) where 1‰ decrease in $\delta^{18}O$ corresponds to a 4.3°C rise in temperature. Given that ice volume and sea level have been relatively stable in the late Holocene and that the local hydrographic regime in the study area is outside of the

maximum sea ice belt these factors are unlikely to contribute significantly to the $\delta^{18}O$ signal. Even so, local salinity changes are possible in the late Holocene due to changes in evaporation and precipitation as well as surface ocean freshwater transport. In the region of the study site, the $\delta^{18}O$ and the salinity fall close to a linear trend in near surface waters. Based on several available measurements (Ostlund, 1987; Meredith et al., 1999) of $\delta^{18}O$ and salinity from the South Atlantic region (between45-60°S and 20-47°W) of the core location in this study, it is estimated that a 1 psu change in salinity corresponds to a 0.55‰ change in $\delta^{18}O$ in this area (Pers. comm. U. Ninnemann; see Appendix F). Today the spatial gradient in surface salinity in the polar waters surrounding the core site is exceptionally low (within <0.1 psu over a 500 km radius) (Schmidt et al., 1999). With such small lateral gradients, lateral shifts in water masses are unlikely to drive any significant (observable) $\delta^{18}O$ variability at the core site. Thus, I focus on temperature as the most likely driver of $\delta^{18}O$ variability, and interpret the $\delta^{18}O$ calcite record variability primarily as potential changes in water mass temperature, while keeping in mind that the signal may have been caused or influenced by salinity changes.

6.2.1 Late Holocene planktic oxygen isotopic record

To address and identify changes in near-surface water characteristics of the north Scotia Sea I use planktic foraminifera isotopic values. *N.pachyderma* (s.) were abundant through the core and enough were picked for duplicate analyses, ensuring a robust record. The $\delta^{18}O$ of *N.pachyderma* (s.) should reliably represent regional near-surface water temperature and salinity at the core location.

In Figure 6.3 the *N. pachyderma* (s.) $\delta^{18}O$ record from core GS08-151-02MC (Appendix B) is plotted versus depth (cm). The depth scale is provided for centimeters below the seafloor. The blue circles indicate the average of the measured values for the two replicates at each depth interval (0.5 cm), and the blue line connects these values.

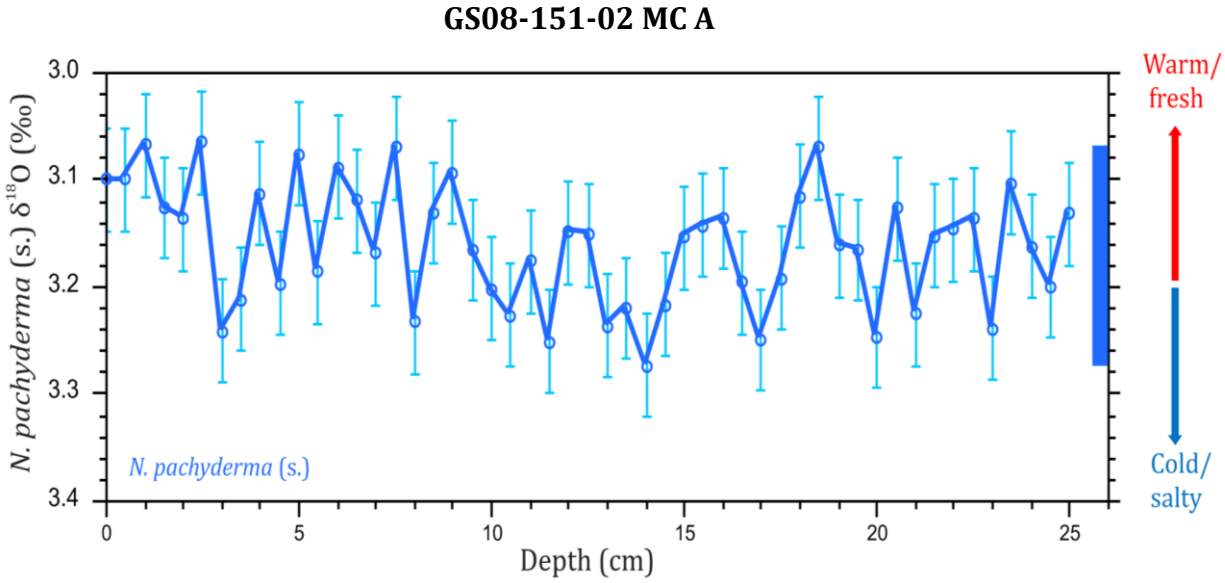

Figure 6.3: Oxygen isotope values of the planktic foraminifera N. pachyderma (s.) of core GS08-151-02MC A (blue curve) relative to VPDB analyzed at 0.5 cm resolution plotted versus core depth. The error bars (light blue) ±0.048‰, denote the pooled standard deviation (1σ) of replicates to illustrate uncertainty. The blue bar illustrates the range of variability. The red and blue arrows to the right indicate related changes in ocean water properties.

The pooled standard deviation for replicates at each core depth level is calculated to ±0.048‰. By comparison, the analytical uncertainty determined by replicate analyses of carbonate standards over a long period of time is (±0.08‰). Thus, the samples at any given depth replicate better than the in house standard, suggesting that they are more homogeneous than the standard material and provide relatively robust and precise results. Hence, the major source of uncertainty in my results appears to be analytical precision of the mass spectrometer and not the uncertainty of any individual analysis.

The downcore N. *pachyderma* (s.) $\delta^{18}O$ record exhibits only (relatively) small fluctuations and no cyclic variability. The mean of the downcore $\delta^{18}O$ record is 3.16‰ and the standard deviation is 0.073‰ (1σ STD), which is equivalent to a temperature change of 0.31°C or a change in salinity of 0.13 psu. The $\delta^{18}O$ record shows minor oscillations ranging from 3.06‰ to 3.27‰, making up a total difference of 0.21 ‰ (blue bar in the plot). This variation is equivalent to a potential sea surface temperature (SST) change of 0.85°C or a salinity change of ~0.38 psu. Decreasing $\delta^{18}O$ indicates warmer and/or fresher conditions. Increasing $\delta^{18}O$ indicates cooled and/or more saline conditions (note that the values of the Y-axix for $\delta^{18}O$ is reversed).

Isotope records that are plotted versus depth provide the most robust curves with the smallest uncertainties (Figure 6.3). However, it is crucial to view the variability from a chronological perspective in order to make any statements on the rate and specific timing of the observed changes.

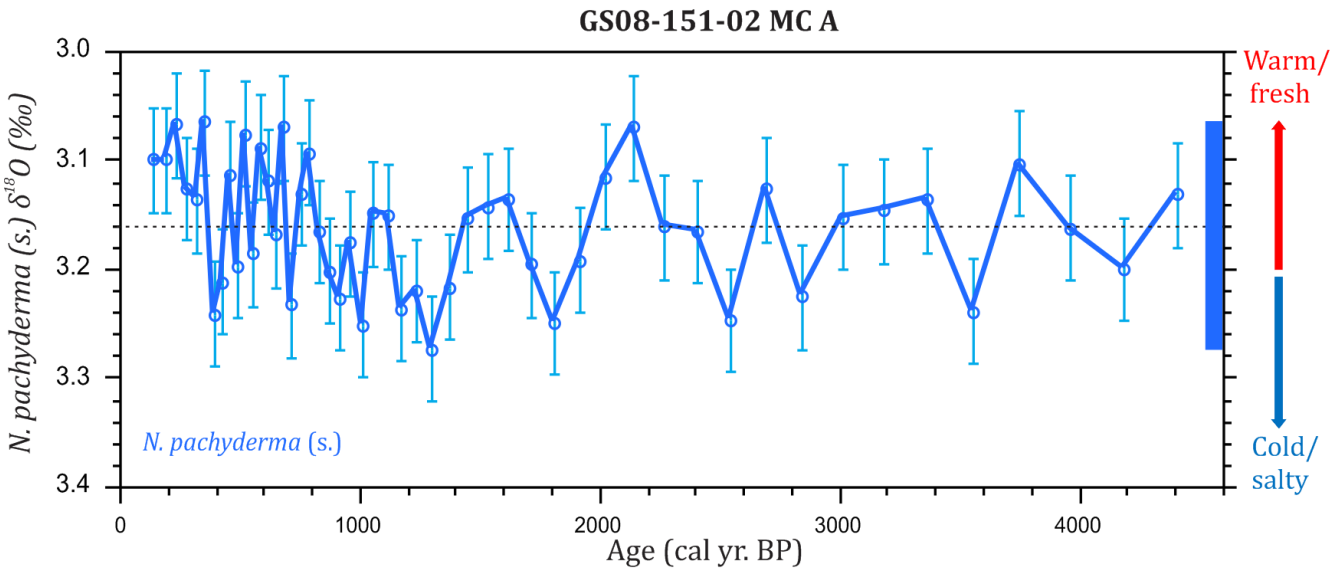

Figure 6.4: Oxygen isotope values of the planktic foraminifera *N. pachyderma* (s.) of core GS08-151-02MC-A (blue curve) relative to VPDB analysed at 0.5 cm resolution plotted versus age. The error bars (light blue) of ±0.048‰ denote the pooled standard deviation (1σ) of replicates to illustrate uncertainty. The blue bar illustrates the range of variability. The red and blue arrows on the right hand side indicate related changes in ocean water properties. The mean value is marked by dashed line.

The results from the $\delta^{18}O$ measurements of N. *pachyderma* (s) from core GS08-151-02MC, are plotted in Figure 6.4 (unsmoothed with error bars) versus age (from ~4 200-140 yr BP). The time resolution is lowest at the bottom of the core with increasing resolution towards the core top due to higher sedimentation rates.

As in the depth plot, the variance in the planktic $\delta^{18}O$ record is small (0.073‰ = 1σ STD) over the late Holocene. Indeed, the downcore variance is similar to, if not smaller than, the analytical precision of the instrument. However, the replicate analyses suggests that the reproducibility may be better, than what is determined by standards. Within the 1σ error bars most measurements are falling within the mean N. *pachyderma* (s.) $\delta^{18}O$ signal of 3.16‰ (dashed line). Thus, there is not much variance and I classify the record as remarkably stable.

However, some small features in the record are evident. One of them being the steady decrease in $\delta^{18}O$ of 0.17‰ since 1300 yr BP (3.27-3.1‰=0.17‰) equivalent to a warming of 0.73°C (or freshening of 0.3psu). Superimposed on the long-term warming is a colder (seen in higher $\delta^{18}O$) period between 700-400 yr BP.

The low planktic $\delta^{18}O$ variability suggests that this region of the Scotia Sea experienced quite stable surface ocean physical properties (temperature and salinity) throughout the late Holocene. The stable result is supported by the context of the location in an open-ocean environment, distant from the maximum sea ice cover, and in polar waters which have relatively cold stable conditions and with no major changes to ice sheets or sea level rise.

6.2.2 Late Holocene benthic oxygen isotopic record

The benthic foraminifera $\delta^{18}O$ record represents variations in the physical properties of the bottom water. The core is retrieved at 2750 m water depth in the north Scotia Sea, bathed in CDW, near maximum NADW influence (see figure 3.3). The initial goal was to use both C. *wuellerstrofi* and U. *peregrina* in order to reconstruct the most complete high-resolution record for the bottom water properties. However, the core was almost barren of the epifaunal benthic foraminifera C. *wuellerstrofi*. Therefore, the U. *peregrina* were used for isotopic analysis (Figure 6.5).

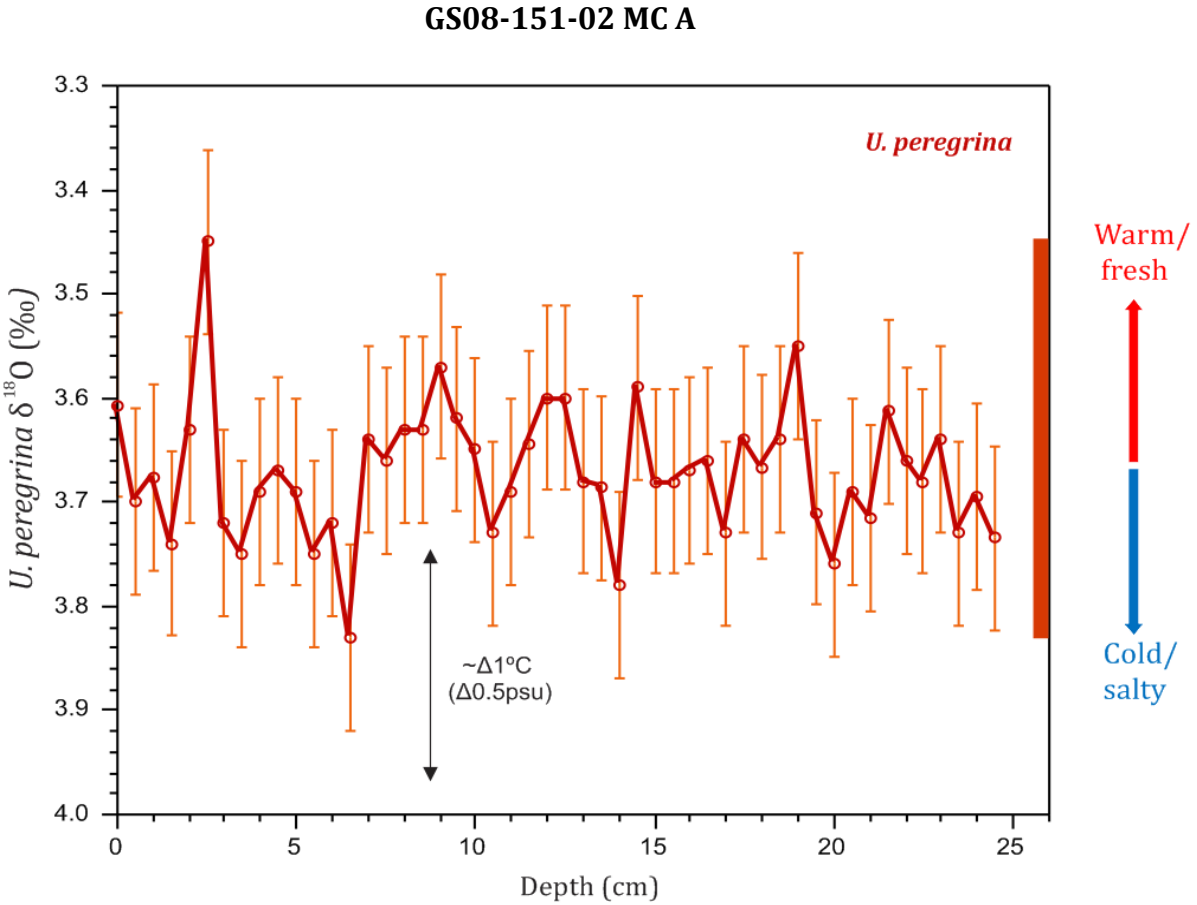

Figure 6.5: The average of all oxygen isotope measurements are plotted (red line) core depth. Circles are showing the average oxygen isotope value at each 0.5 cm core depth level. The error bars (light orange) of ±0.089‰ represent the mean standard deviation of replicates at each core depth level The arrows on the right indicate changes in bottom water properties that cause variations in $\delta^{18}O$.

The standard deviation for replicates from the mean (±0.089‰) of any individual analysis is only slightly larger than the analytical precision of the mass spectrometer (±0.08‰), confirming that the material reproduces well. The average oxygen isotope value (red circles) at each 0.5cm core depth is based on the average of one to three replicates (Appendix C). Approximately 40% of the measurements had no replicates. The $\delta^{18}O$ signal at the depth intervals where no replicates were analyzed could be slightly more prone to influence by outliers. This uncertainty related to a low number of replicates can be quantified by considering the standard error of the mean. The standard error of the mean (SEM) for intervals of duplicate measurements is 0.063‰, and for intervals with triplicates measurements it is 0.056‰ and 0.048‰ for intervals of quadruplicate

measurements. This show that the uncertainty gets slightly lower with increasing number of replicates.

The $\delta^{18}O$ record of *U. peregrina* displays intermittently warmer (fresher) and cooler (more saline) periods throughout the last ~4200 yr BP. The record ranges between a minimum of 3.45‰ and maximum of 3.83‰. The total range of Δ0.38‰, illustrated in Figure 6.6 with red bar, is equivalent to a change of 1.6°C or 0.68 psu. The mean $\delta^{18}O$ value is 3.67‰, and the standard deviation (1σ STD) for the entire record is ± 0.063‰ (ie. ± <0.3°C).

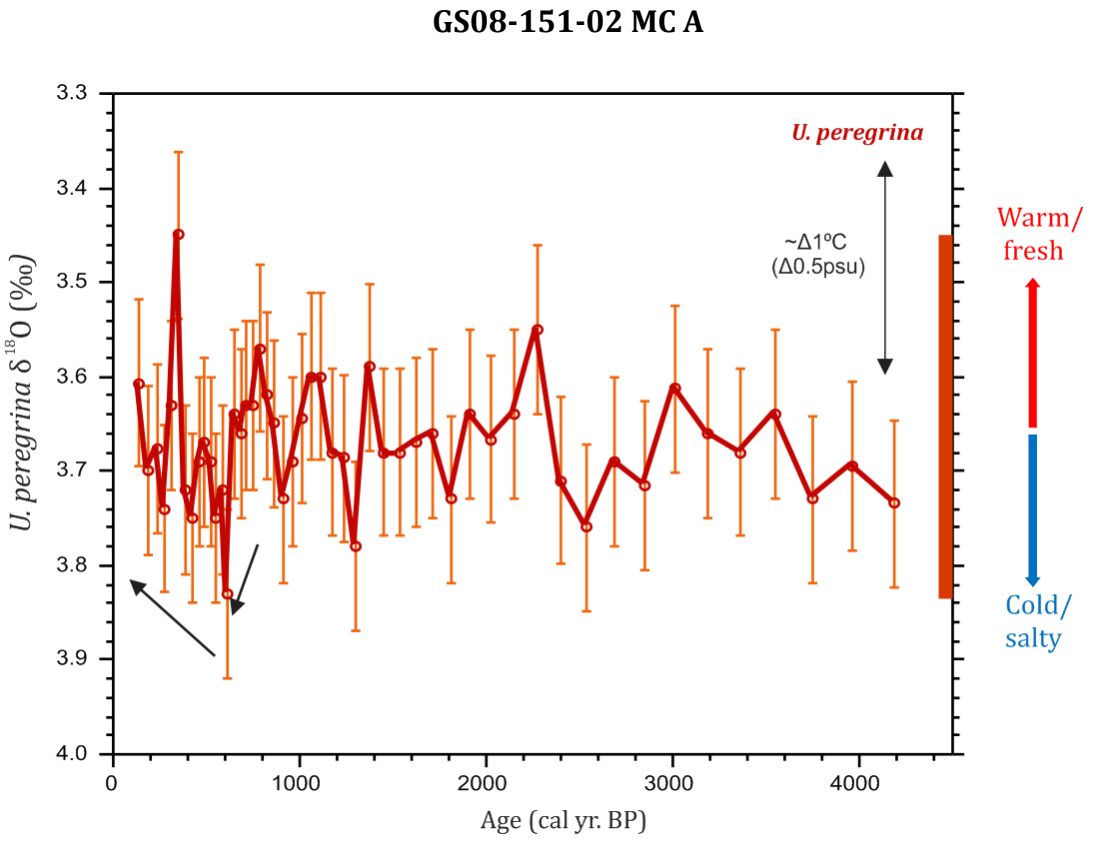

Figure 6.6: The average of all oxygen isotope measurements are plotted (red line) versus age (cal. Yr. BP). Circles are showing the average oxygen isotope value at each 0.5 cm core depth level with light orange error bars (0.0892) going through the sample points. The red bar sow total range of the average plot. The arrows on the right indicate changes in bottom water properties that cause variations in $\delta^{18}O$.

The record shows a very stable long term trend on millennial to multi millennial time scales. The result is consistent with deep-water location (2750 m depth). Changes in deep water properties tend to be on a slightly longer timescales relative to the surface water,

and with larger magnitude. Superimposed on the long-term stable signal is high frequency centennial $\delta^{18}O$ variability, especially during the last 1400 years (figure 6.7).

There is an abrupt increase in $\delta^{18}O$ of 0.26‰ (~1.1°C /0.47psu) between 800 and 600 yr BP (blue box, Figure 6.7) followed by a decrease towards the core top, with a $\delta^{18}O$ minima of 3.45‰ occurring around 355 yr BP. Within this final slightly warming phase there is a drastic warming peak just after 400 yr BP with an oscillation of 0.28‰ (~1.1°C /0.47psu) in the course of 114 years (391-277 yr BP), shown by pink box in Figure 6.6. In addition, there is a sharp benthic $\delta^{18}O$ decrease of 0.28‰ between about 391 and 355 yr BP.

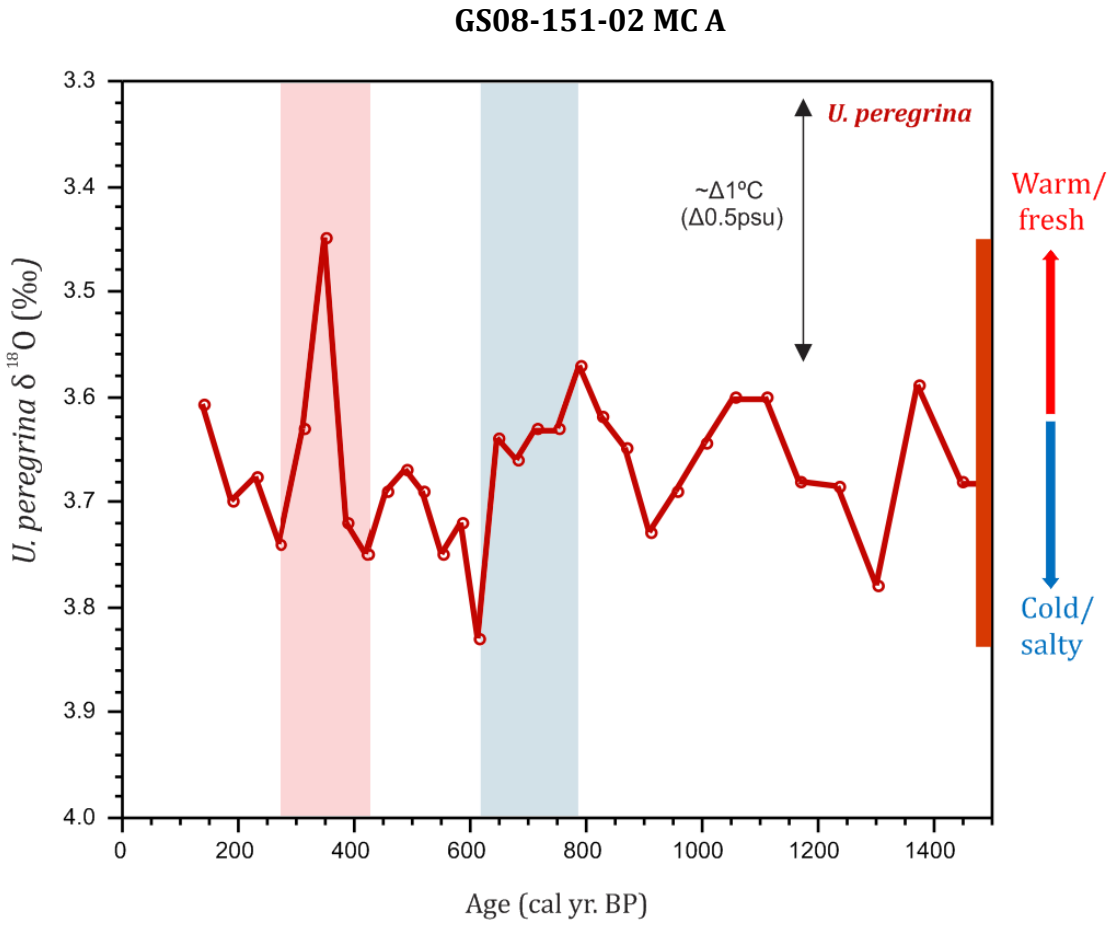

Figure 6.7: Zoomed in figure of the last 1400 yr BP of the benthic *U. peregrina* $\delta^{18}O$ record. Blue box showing abrupt cooling. Pink box displaying the abrupt warming oscillation. Arrows is put in place for temperature/salinity scale.

6.3 Carbon isotope result

In this sub-chapter $\delta^{13}C$ is presented for the past ~4200 years derived from planktic and benthic foraminifera species to show near surface and bottom water properties. The $\delta^{13}C$ (DIC) gradient is controlled by the interplay between biological productivity and nutrient cycles in the water masses, and the ocean - atmosphere exchange of CO_2 (Charles et al., 1993). The surface ocean is generally enriched in ^{13}C and depleted in nutrients, principally because of the preferred incorporation of ^{12}C in to organic matter. The nutrient levels increase as $\delta^{13}C$ values get lighter deeper in the water column due to decomposition of organic matter (Kroopnick, 1985).

The carbon isotope ($\delta^{13}C$) record of planktic and benthic foraminifera are key parameter in describing past carbon cycle oscillations, changes in nutrients and tracking influence of different water masses. However, isotope ratios and nutrients may not be entirely correlated due to air-sea interaction. This is because carbon circulates through the atmosphere and the sea, whereas nutrient circulation is restricted to the oceans. Deviations from equilibrium also occur due to vital effects in the foraminifera (subchapter 4.3 and 4.5.2). The core site, located in the Atlantic sector of the Southern Ocean, is a region well situated to respond to ocean circulation shifts. Thus, benthic (bottom water) $\delta^{13}C$ values will be used to track the changes in the THC, especially influx of NADW and chemical properties of CDW while planktic (near surface water) will monitor possible effects of icebergs enhanced productivity and sequestration of organic carbon to the deep sea.

6.3.1 Late Holocene planktic carbon isotopic record

The carbon isotope measurements for of *N. pachyderma* (s.) from core GS08-151-02MC are plotted versus age (yr BP) and presented in Figure 6.8. The $\delta^{13}C$ values for the planktic record varies between 1.26‰ and 1.51‰ with a standard deviation from the mean (1.39‰ – dashed line) of the plot of 0.06‰ (1σ STD). The blue bar denotes the total range of variability in $\delta^{13}C$ of 0.25 ‰.

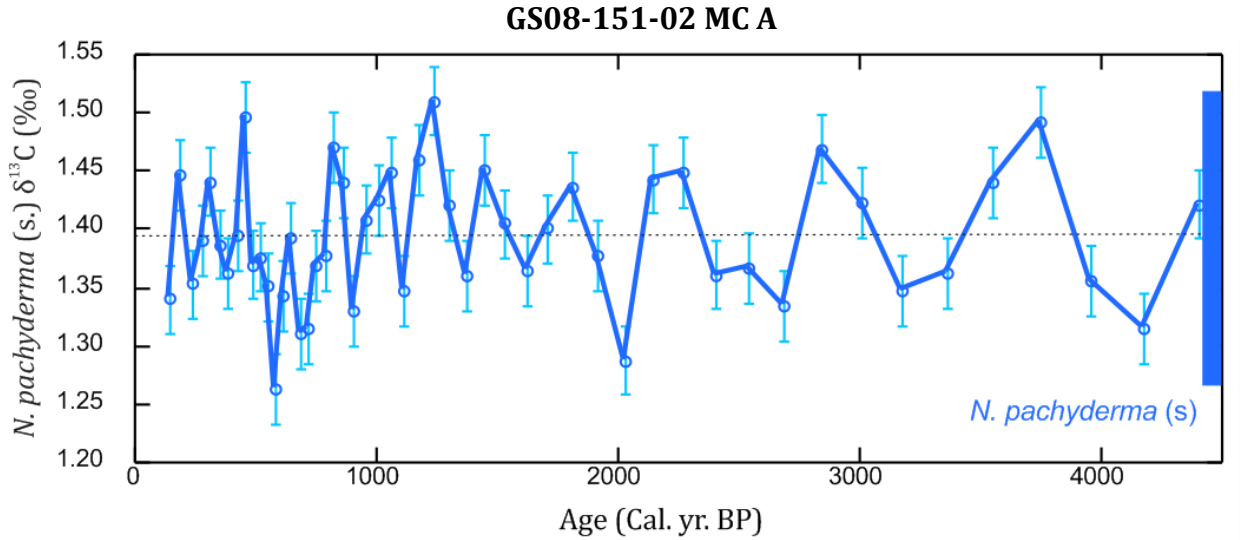

Figure 6.8: The blue line traces the average carbon isotope value at each 0.5 cm core depth level for N. *pachyderma* (s). The average is based on up to two replicates for each depth interval (Appendix B). The mean standard error at each core depth level is ±0.03‰, shown as light blue error bars.

The studied interval exhibits relatively small variability around the mean $\delta^{13}C$ value of 1.392‰, showed as dashed line the Figure 6.8. Superimposed on the minor oscillations is the pronounced decrease following the peak planktic $\delta^{13}C$ values at 1200 yr BP until minimum $\delta^{13}C$ values at 600 yr BP and the rapid rebound back to peak levels 460 yr BP, initiated abruptly over 1 cm. A pronounced decline in $\delta^{13}C$ values indicate that nutrient content in the water masses decreased over the same time interval.

6.3.2 Late Holocene benthic carbon isotopic record

Assuming that the deep South Atlantic water mass geometry has remained the same through the late Holocene one could expect $\delta^{13}C$ values close to 0.3‰ for the AABW (Eide et al., 2017), because of its higher content of nutrients and ^{12}C. Kroopnick (1985) found that NADW usually has values ranging from 1.0 – 1.4‰. As the core site is located close to the area of AABW formation and in an area of NADW influence, the $\delta^{13}C$ is expected to be relatively low.

The infaunal habitat of U. *peregrina* can alter the signal by reflecting the properties of the pore water in the sediment, rather than current bottom water properties. In addition, as the foraminifera grows within the sediment, it is surrounded by material previously deposited, creating potential relative time offset with the material from the same level

that is used for dating (planktic foraminifera). Thus, the actual timing of the *U. peregrina* $\delta^{13}C$ changes could be younger than what is represented in the plotted data. The carbon isotope measurements for U. *peregrina* (GS08-151-02MC) are plotted in Figure 6.9 versus age. The red circles, with connecting lines, represent the average of 1-4 replicate isotopic analysis for each sample interval (0.5cm). The light error bars are set after calculating the average deviation from the mean for each replicate.

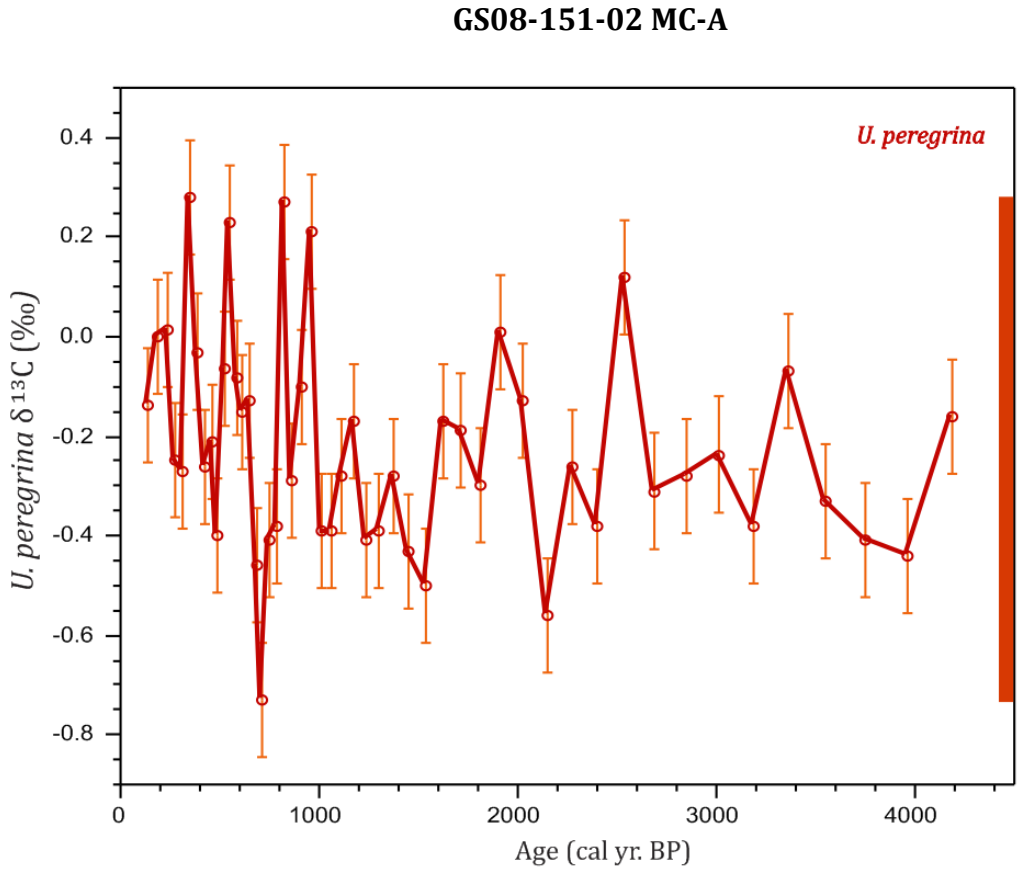

Figure 6.9: The red line traces the average $\delta^{13}C$ value of U. *peregrina* at each 0.5 cm core depth level. The average is based on 1 to 4 replicates for each depth interval (Appendix C.2). The mean standard error at each core depth level is ±0.115‰.

The U. *peregrina* $\delta^{13}C$ record ranges from a minimum of -0.73 ‰ to a maximum of 0.28‰, with a standard deviation of 0.21‰ (1σ STD) and overall change in the record of 1.01‰, shown in the plot as red bar. The signal appears to be relatively stable, without any cyclic behavior or strong trends. The main feature of the record is the relatively large amplitude benthic $\delta^{13}C$ anomalies occurring between 1100 yr BP to present. The high frequency variability within the period occurs on multidecadal to centennial time scales. Prior to

1100 yr BP, the signal is fluctuating around the mean $\delta^{13}C$ value of -0.22 ‰. The larger scale trend over the last millennium has been generally increasing $\delta^{13}C$ values. Superimposed on this trend are two $\delta^{13}C$ peaks between 960 and 839 yr BP. Subsequently, $\delta^{13}C$ rapidly decreases to a minimum at around 700 yr BP suggesting the presence of low-$\delta^{13}C$ bottom water, or increased sedimentation of organic matter, at the core site. Following is a sharp transition to maximum $\delta^{13}C$ levels at around 350 yr BP. The rapid decrease in $\delta^{13}C$ of 1.01‰ over just a few hundred years stand out between the four peaks and higher $\delta^{13}C$ levels during the last millennia.

7 Discussion

There are very little information about centennial scale natural variability of iceberg calving, which is necessary in order to place the recent observational period in context. This thesis provides one of the first high-resolution iceberg rafted debris (IRD) records tracking ice-sheet dynamics and variability, co-registered with planktic and benthic isotope measurements recording variability in regional climate and ocean circulation. The study site is located on the northern edge of the iceberg alley beyond the influence of seasonal sea ice cover (Figure 7.1). This position is sensitive to the flux of icebergs exiting the western edge of the Weddell gyre, predominantly sourced from the WAIS and the Antarctic Peninsula. Additionally, the site is currently beyond the geographic limit of any confounding influence by sea ice rafted debris which complicates records further south and east of the core site within the seasonal sea ice zone. Thus, the site is ideal for portraying past WAIS dynamics and regional climate, and can provide insights into the scale, frequency, and origin of the (natural) variability in Antarctic Ice sheet calving.

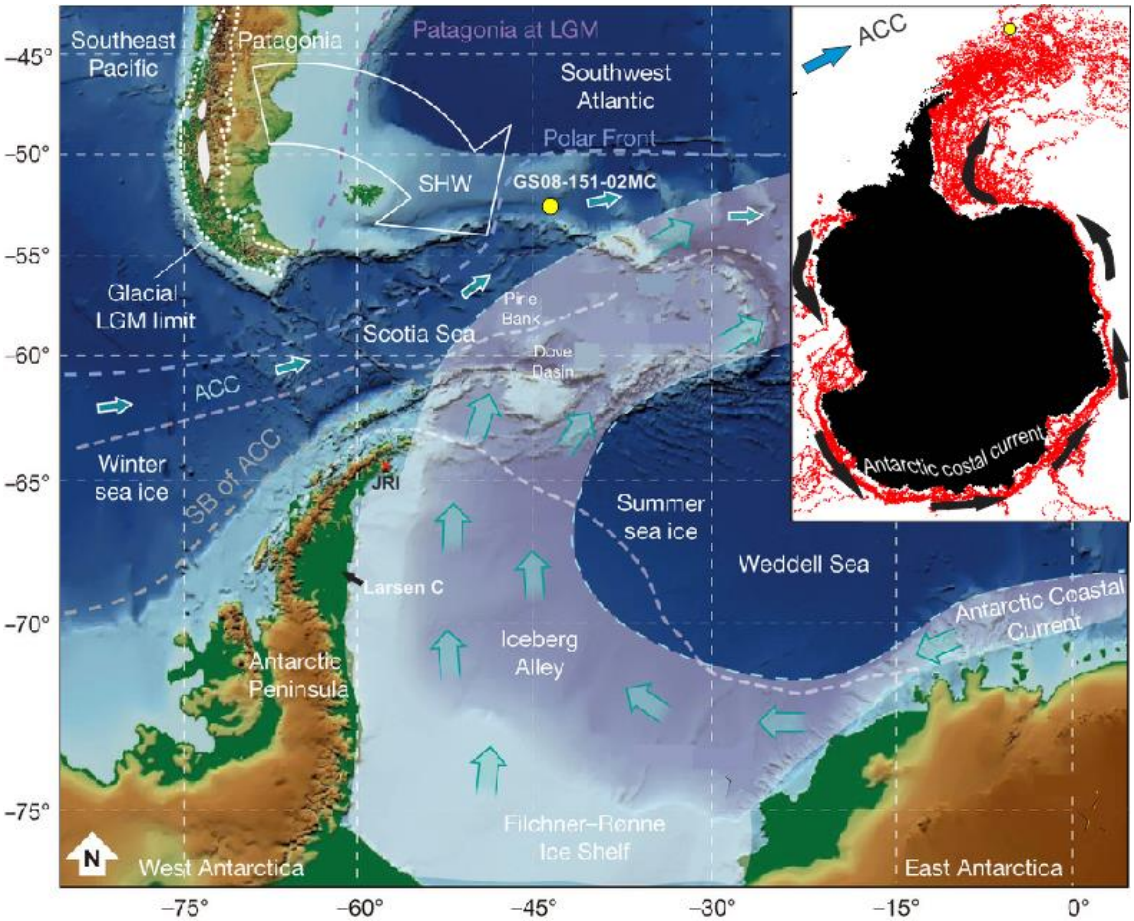

Figure 7.1: Locations of the main pathway of Icebergs and the cores location (yellow dot). White dashed lines show winter and summer sea-ice extent (modified after Weber et al. (2014)). The

inset map (upper right) shows the circum-Antarctic drift of icebergs (red; ≥5 km in length) calving off the Antarctic ice shelves from 1999 to 2009. Black arrows indicate the general pattern) counterclockwise flow within the Antarctic Coastal Current, modified after (Stuart & Long, 2011).

7.1 Possible mechanisms explaining variability in the IRD record.

Antarctic icebergs are large blocks of frozen fresh water that melt around the Antarctic continent while moving under the influence of winds, sea ice, and ocean currents. Icebergs can drift over thousands of kilometers (Rackow et al., 2017) and over several years. The IRD result (described in detail in Chapter 6.1) showed higher amount of IRD within the oldest half of the core from 4200 – 1800 yr BP, followed by a pronounced decrease up until 600 yr BP when the amount of IRD peaked briefly and then steadily increased towards pre industrial times.

What could drive this observed variability in IRD at the core site? The northern limit of iceberg occurrence in the South Atlantic today is equivalent to surface water temperature of about 4°C (austral summer) (Hodell et al., 2001). Given that the Polar Front (PF) is commonly associated with the 2°C isotherm (winter) and has a strong temperature gradient (typically ~1-2°C; Gordon (1971)) the PF strongly influences the maximum extent of iceberg survival. Located to the east (i.e. poleward) of the topographically controlled position of the PF (Figure 7.1), The GS08-151-02 core site is clearly within the range of iceberg influence. However, it is near the northern limits of todays iceberg range and thus iceberg delivery could be sensitive to local temperature changes. Likewise, the main iceberg trajectories (Figure 7.1 inset) follow the surface circulation in the Weddell gyre, which is sensitive to the mean position of the winds responsible for driving the gyre in combination with topography. Thus, a climatic shift in wind patterns could influence surface circulation and iceberg routing pathways. Finally, changes in the generation rate or 'supply' of icebergs would influence iceberg supply to the core site. While it is common for IRD studies to interpret IRD content as changes in iceberg production or 'supply', the influence of routing and survival are also considered and discussed in this chapter.

Thus, the hypothesized mechanisms for driving variability in IRD input are:

1. Survival of icebergs as local conditions warmed/cooled.
2. Supply of icebergs generated by calving from the Antarctic ice sheet
3. Routing of icebergs to the core site driven by changes in winds and ocean circulation.

7.1.1 Comparison between near-surface ocean hydrography and IRD variability.

In order to differentiate between these possible mechanisms for driving the observed IRD variability I first look to the near surface oxygen isotopic records from core GS08-151-02 in the northern Scotia Sea. These records provide information about the ocean salinity and temperature changes occurring within the last ~4200 yr BP.

The $\delta^{18}O$ records from the planktic foraminifera *N. pacyderma* (s) depict the natural variability for local surface water in which it grows. A decrease in $\delta^{18}O$ is a proxy for increasing temperatures and/or freshening of the surface water. Thus, any local sea surface changes given by the planktic $\delta^{18}O$ (e.g. temperature) that covary with IRD would indicate that IRD input is modulated by local climate and survival of the icebergs.

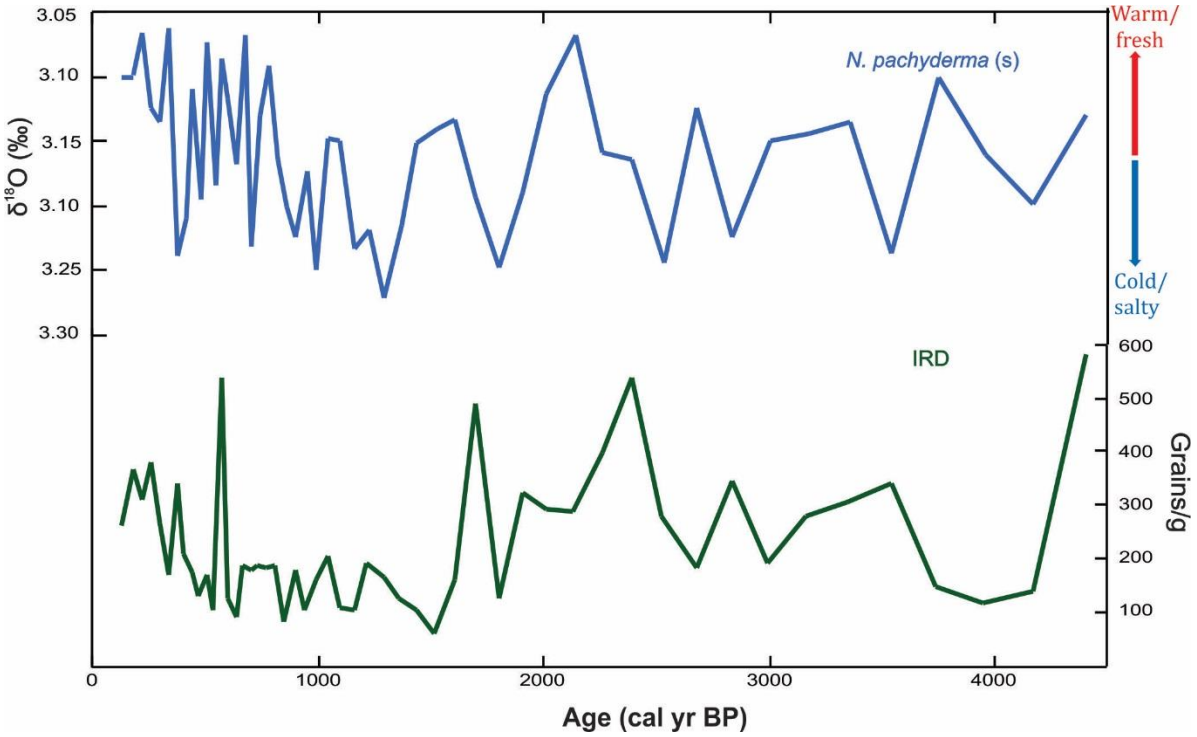

Figure 7.2 Comparison of $\delta^{18}O$ record of near surface properties from site GS08-151-02, depicted by N. *pachyderma* (s.) (in blue color) and Iceberg rafted debris counts in grains per gram (green color) for the last ~4200 years.

The planktic isotope signal reflecting near-surface water temperature and salinity changes appear to be remarkably stable. The small changes in planktic $\delta^{18}O$ (total range of 0.21 ‰) is equivalent to a maximum variability of <1°C (0.85°C). Indeed, variability around the mean is typically less than 0.3°C (1σ STD of $\delta^{18}O$ is 0.073‰; see section 6.2.1). Together this suggests that prior to the last century, surface hydrography in this region was extremely stable and appears to never have surpassed the upper limit for iceberg survival. Furthermore, there is no clear covariance between the near surface properties ($\delta^{18}O$) and IRD. If anything, there is a tendency toward more IRD when SST is warmer, which is inconsistent with the signal expected if IRD were modulated by local temperature. Taken together, the planktic $\delta^{18}O$ record provides new constraints on surface ocean hydrography, which suggests that local temperature changes were not a major factor in driving the observed downcore variability in IRD.

The caveat on this conclusion is that $\delta^{18}O$ does not only monitor temperature, and if there were competing and compensating effects of salinity ($\delta^{18}O$ w) from the foraminiferal isotopes, these could mask temperature changes. However the surface gradient in salinity in the core site region is exceptionally low (<0.1psu over 500km radius) (Schmidt et al., 1999). Thus, I focus on temperature as the most likely driver of $\delta^{18}O$ variability. The stability of the PF, the downcore consistency in *N. pachyderma* (s) dominance, and regionally homogeneous salinities are all evidence consistent with temperature as the dominant influence on planktic $\delta^{18}O$. While other temperature proxies should be analyzed to confirm this (e.g. diatom transfer functions or Mg/Ca of *N. pachyderma*), the available evidence suggests relatively minor changes in ocean temperature occurred during the late Holocene in the northern Scotia Sea.

The Neoglaciation, lasting from 5000-6000 yr BP to pre-industrial times (Nesje & Dahl, 1993), covers the time interval studied in this thesis. Several studies (Hodell et al. 2001; Bakker et al., 2017) have used increased IRD input as evidence for the onset of the Neoglaciation. However, the planktic $\delta^{18}O$ results show no clear evidence for particularly cool conditions or major changes throughout the Neoglaciation. Since the core does not extend past 6000 yr BP it is not possible to rule out the possibility that warmer conditions persisted locally prior to this time. Further mapping of the Neoglaciations regional

expression could provide insight for constraining the mechanisms behind this cooling and its global (vs. regional) significance.

Nevertheless, a simple secular Neoglacial cooling at ~5000 years BP would not explain the variable IRD signal observed in Southern Ocean cores, nor do local variations in temperature appear to drive the local IRD survival. Thus, it is worth considering other factors (than cooling) such as supply of IRD for driving IRD variability. Two factors could drive IRD delivery changes; either there are more icebergs produced by calving of the ice sheet or the routing of the icebergs have varied. Both of which can be climatically driven.

7.1.2 West Antarctic ice sheet discharge

Firstly, I look to where the Icebergs are sourced from. Based on geochemical evidence by Smith et al. (1983) and iceberg trajectories by Stuart and Long (2011) (Figure 7.1), I interpret the icebergs passing the core site to originate primarily from the east Antarctic peninsula (AP). Thus, this will be the focus area for comparing paleoclimate records, where the majority of the icebergs are generated and transported out in the iceberg alley by the Weddell gyre (to the core location)(Chapter 3.2.4).

In order to test the hypothesis that the IRD variability is driven by the amount of calving from WAIS, more specifically the AP, information regarding the climatic and ice sheet changes in this region are needed. The James Ross Island (JRI) ice core is located near the northeastern tip of the AP (red mark on Figure 7.1). In Figure 7.3, I compare the IRD record with the JRI temperature anomalies, relative to the 1961–1990 AD, which are based on an ice-core record of deuterium variations and ice-core age scale. The record was calibrated to yr BP, based on a glaciological flow model with age control provided by volcanic eruptions as fixed time markers (Mulvaney et al., 2012).

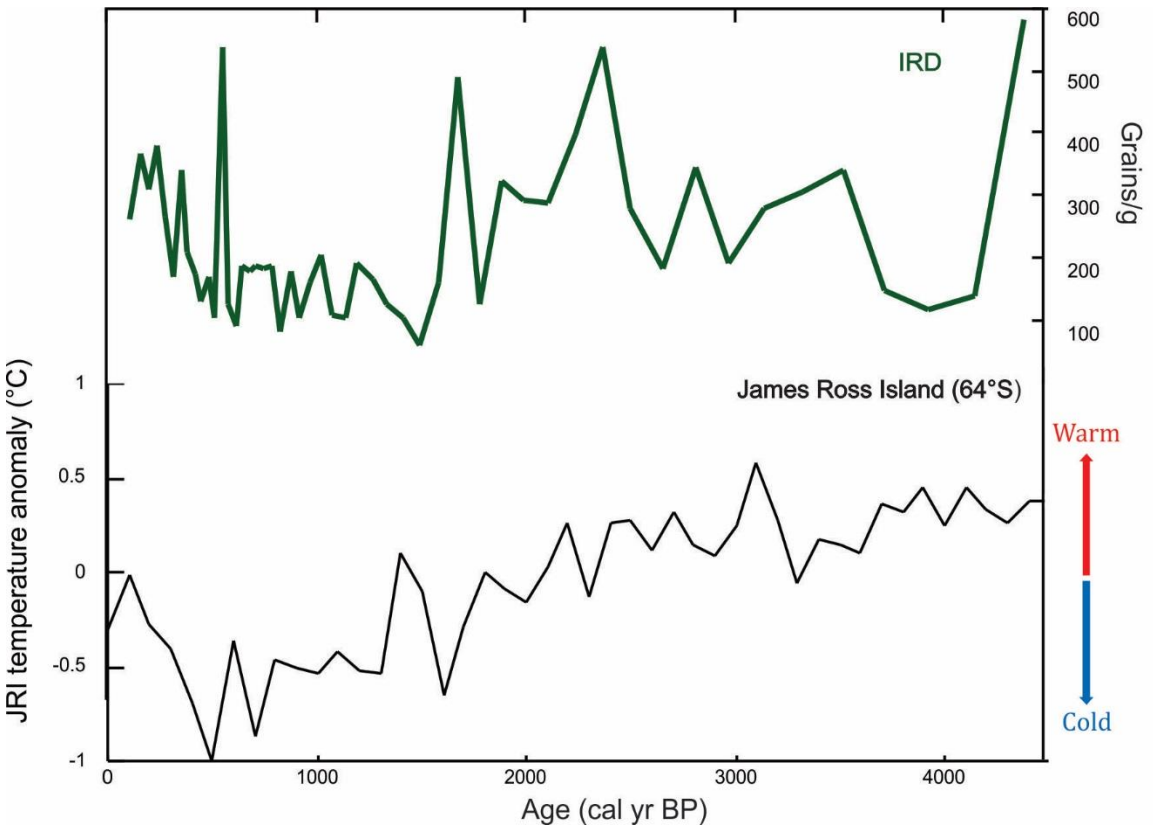

Figure 7.3: IRD counts in grains per gram (green color) for the last ~4200 years compare with atmospheric temperature anomalies from JRI ice core on the east side of the Antarctic Peninsula (Mulvaney et al., 2012).

The JRI ice core documents a long interval of stable climate, prior to the compared time interval, that persisted from 9200 to 2500 yr BP with marginally warmer temperatures than present conditions from 5000 to 3000 yr BP (Mulvaney et al., 2012). This mid Holocene hypsithermal observed at JRI is small in magnitude compared with the well-defined mid-Holocene climate optimum in continental Antarctic ice core records (Masson et al., 2000)—perhaps suggesting the ocean had a moderating influence on JRI climate. After 2500 yr BP, the JRI isotope data show pronounced cooling to a temperature average 0.7°C cooler than present between 800 and 400 yr BP. Followed by sustained warming at JRI starting at 600 yr BP.

Figure 7.3 shows that the IRD record covaries with the regional climate on the eastern AP (based on JRI ice core) over the past 4200 years. There is a general trend of warmer temperatures at JRI and more IRD during the first half of the recorded time period. The gradual cooler conditions occurring after 2500 yr BP at JRI is coincident with decreasing

amounts of IRD in GS08-151-02 over the same time interval, both plateauing with minimum temperatures and minimum IRD around 1000 yr BP. The two records indicate a contemporaneous shift with warming and increased IRD from year 600 BP prior to industrialization. The highest IRD intervals are similar in timing with greater JRI warming.

I look to additional paleoclimate records in order to carry out a regional investigation to evaluate whether JRI temperatures and the IRD signal are consistent with other records documenting past east Antarctic Peninusula ice sheet variability. The Larsen Ice Shelf is positioned just south of the JRI, on the eastern AP and is today a subject for iceberg caving and instability. A sediment core collected by Brachfeld et al. (2003) from beneath the former Larsen-A Ice Shelf documents past variability in the extent of the ice shelf. Their diatomaceous ooze layers, marking intervals with productive open-water, indicate instability of the Larsen A Ice Shelf between 3800 and 1400 yr BP. This period of greater Larsen A instability and retreat overlaps with the period of higher temperatures at the JRI and higher amounts of IRD input to core site. This coherent trend of changes between the Larsen Ice Shelf and the JRI, documenting warmer climate at the source area of icebergs, is consistent with increased iceberg generation and IRD delivery to the core site. Thus, the available evidence suggests that warming on the east AP coincides with increased calving and supply of icebergs consistent with higher concentrations of icebergs at the core site driven by the higher generation rate of icebergs.

What would drive these past changes in ice margin stability? Modern analogs can be used to further elucidate the potential connection between iceberg supply and AP warming. Domack et al. (2005) suggest that the recent prolonged period of warming in the Antarctic Peninsula region (King et al., 2003; Scambos et al., 2003) in combination with the long-term thinning of the ice shelves, has led to collapse of the Larsen ice shelves. The southernmost Larsen A collapsed in 1995, Larsen B in 2002 and Larsen C started to break up in 2016. The recent collapse of the Larsen Ice Shelf is unprecedented during the Holocene (Domack et al., 2005).

Widespread ice sheet acceleration is consistent with ice shelf removal (Scambos et al., 2003; Shepherd et al., 2003; Rignot et al., 2004). The abrupt evolution of the glaciers is attributed to the removal of the ice shelf. As summarized in subchapter 2.3.1, these

observations are in broad agreement with the theory of ice shelf buttressing. In addition, warmer air temperatures can increase surface melt water production, which is transported to the bed through crevasses in the ice sheet and increase basal lubrication at the base of the ice sheet (Zwally et al., 2002). Hence, a combination of basal lubrication and ice shelf instability can significantly accelerate ice sheet flow (Figure 2.4b).

Subglacial melt could also be an important mechanism for driving past ice shelf retreat. The deep basins (>2500 m below sea level, Figure 2.4 a) (Bentley & Ostenso, 1961) beneath the marine based WAIS, makes the ice sheet more prone to changes in marine influence that could cause melting of the ice margin and thus influence ice dynamics and calving rates (Alley et al., 2015) (see Chapter 2.3). Therefore, I consider the possibility that an ocean heat source associated with the Antarctic Circumpolar Current (ACC) drove both ocean induced melting of ice shelves and atmospheric warming of JRI. Circumpolar Deep Water (CDW), which is believed to represent the distal reach of NADW (Broecker et al., 1999) and the deepest part of the ACC (Orsi et al., 1995), is a relatively warm (>1°C), salty (34.65–34.7‰) and poorly-oxygenated intermediate depth water masses (Klinck et al., 2004). Basal ice-shelf melt (shown in Figure 2.5) thus largely depends on the properties of CDW as well as on the effectiveness with which CDW can reach the ice shelves (Joughin & Alley, 2011). The recent pronounced ice shelf thinning observed in WAIS (Rignot, 1998) has been linked to warm (>1°C) CDW intruding the continental shelf through deep troughs (Jenkins et al., 2010) by several previous studies (e.g Jacobs et al., 1979; Jacobs et al., 2011; Bintanja et al., 2013). When this anomalously warm water comes into contact with the ice shelf base it creates basal melting and retreat of the grounding line (Rignot, 1998), consequently thinning the ice shelf, making it less able to buttress the upstream ice-sheet, triggering accelerated glacier flow (Pritchard et al., 2012).

The record of deep-water properties (benthic $\delta^{18}O$) provides a monitor of CDW physical properties with which to test whether changes in deep water temperature or salinity occurred coincident with ice sheet discharge. In Figure 7.4, the benthic $\delta^{18}O$ record is plotted together with the IRD record as a proxy for WAIS discharge variability to evaluate if changes in CDW physical properties were associated with IRD input.

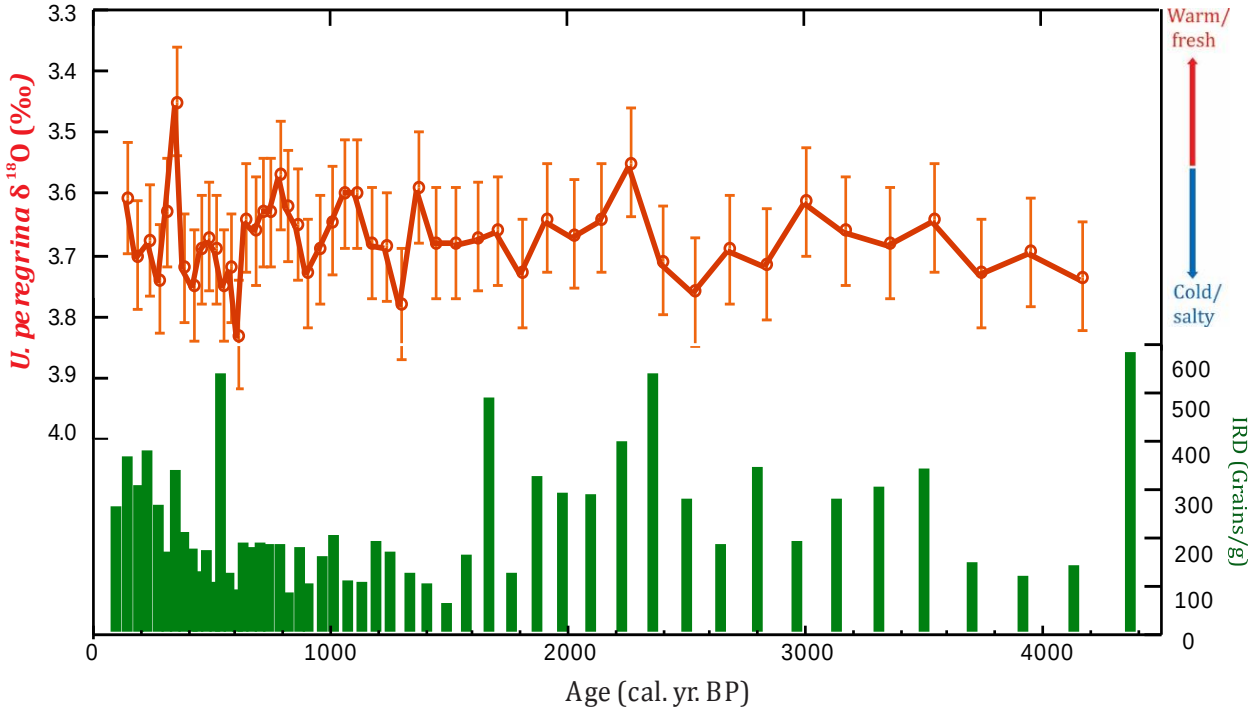

Figure 7.4: Comparison between the IRD records and *U. peregrina* (deep ocean) with error bars (0.089‰). IRD counts are displayed as bars (grains/g) for each core depth interval. The red and blue arrows are denoted to changes in deep-water physical properties.

The high resolution $\delta^{18}O$ record of benthic foraminifera (*U. peregrina*) exhibits relatively small (1σ STD = 0.063‰) variability; equivalent to <0.3°C if driven solely by temperature. Indeed, as mentioned in results (6.2.2), this variance is smaller than the analytical uncertainty, suggesting little to no resolvable natural variability in bottom water temperature occurred, unless it was offset by competing salinity ($\delta^{18}O_w$) changes. In addition, the benthic $\delta^{18}O$ record of *U. peregrina* exhibits no corresponding signal prior to, or consistent with, IRD variability. Therefore, there is no evidence for significant changes in CDW physical properties that could have driven ocean induced melting. Instead, the pathways and amount of CDW advected into sub ice-shelf cavities may have been more influential in driving late Holocene IRD variability.

What is driving the CDW into contact with the ice margins? Numerous studies have reported that increases in SWW and a poleward shift of the ACC (Gille et al., 2002) could bring the anomalously warm CDW into contact with the West Antarctic ice shelves (Rignot, 1998). As explained in Chapter 2.2.2 and 3.2.4, the changes in the strength and position of the Southern westerly winds (SWW) are mainly related to the Southern annular mode (SAM) which is reflecting the atmospheric pressure gradient between the

mid-latitudes and the South Pole. Increasing pressure gradients strengthens the winds and forces the band of SWW to contract towards higher latitudes. SAM is positive when this pressure gradient is high.

The SWW influence the spatial distribution of precipitation in southern South America, with intensified (orographic) precipitation when the SWW strengthens. Thus, palaeoclimatic archives from southern Patagonia provide a view of hydrologic change that can operate as a proxy for strengths in the westerly winds. Moy et al. (2008) presents a $\delta^{18}O$ fine-fraction sediment record from Lago Guanaco lake (51°S) indicating precipitation variability and hence SWW strengths for the last 1200 years (Figure 7.5. b).

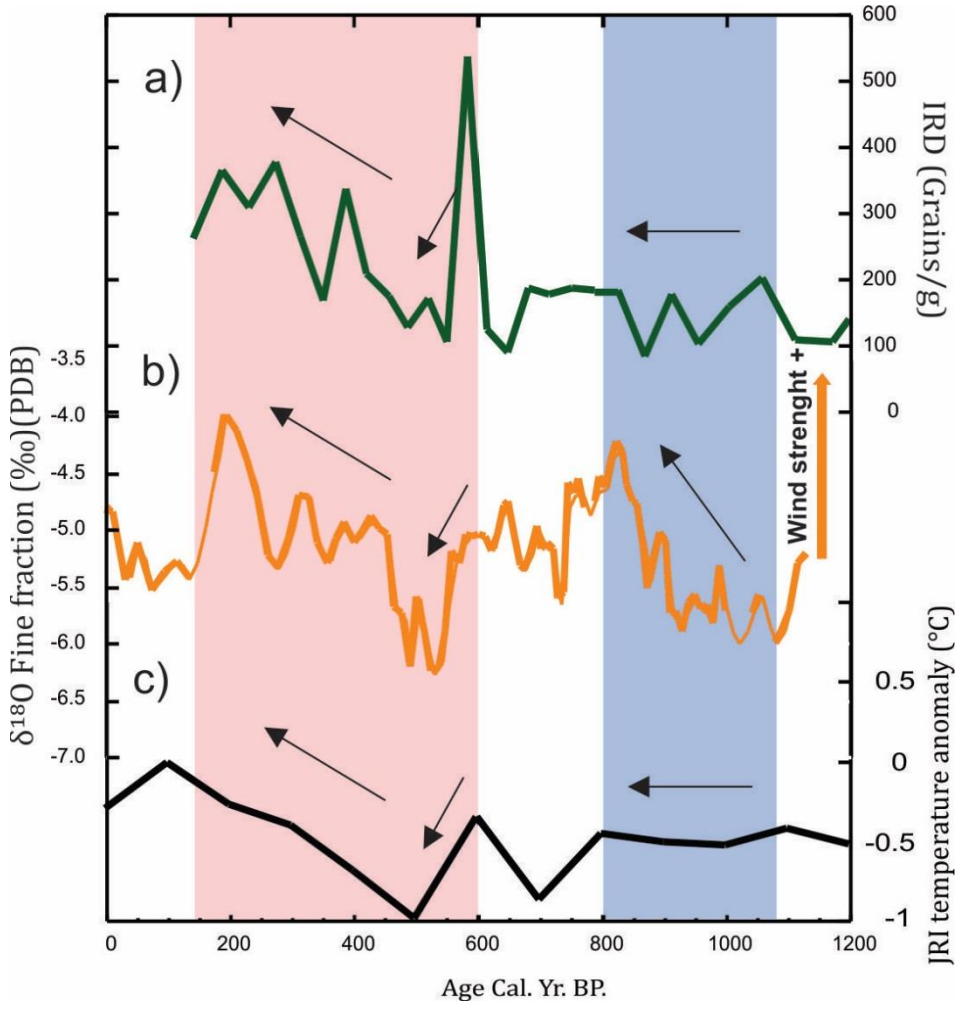

Figure 7.5: Comparing IRD, SWW strengths and JRI temperature(Mulvaney et al., 2012) reconstructions the last 1200 years (Moy et al., 2008). The orange curve display changes in evaporation interpreted from the $\delta^{18}O$ of fine-fraction sediment in Southern Patagonia during the last 1200 cal yr BP, as a proxy for SWW strengths (orange arrow). The pink box indicate when the records covary in phase with each other, and the purple box illustrate when the records are inconsistent.

Figure 7.5 displays the IRD record versus reconstructed SWW and JRI temperature anomalies over the past 1200 years. The figure illustrates (blue box) that the gradual increase in SWW between 1100-800 yr BP, is not reflected in the IRD or JRI temperature record, which are relatively stable through the period. However, the decrease in SWW coincide well with cooling at JRI and low IRD input between around 600 and 500 yr BP, and the following increase in SWW strength since 500 yr BP occurred simultaneously as increased IRD input and warming at JRI. Similarities for the last 600 years (pink box) between the IRD record, the SWW reconstructions (Moy et al., 2008) and JRI temperature variability (Mulvaney et al., 2012) indicate climate teleconnections between atmospheric circulation, the Southern Ocean circulation and the WAIS.

7.1.3 Variability in routing of Icebergs

If winds are changing this would not only drive changes in the Weddell Gyre's ability to transport warm CDW under the ice margin, but could also affect routing of surface ocean currents that carry icebergs. The Weddell gyre determines the position of the iceberg alley as most icebergs transported out from AP is carried out by the gyre's western margin. One possibility is that the Weddell gyre could have expanded or contracted with the changing of the SWW, and in this way could affect the variability in IRD delivery to the core site. In which case an increase in IRD could be reflecting shifts in the wind driven circulation and its ability to transport icebergs to the core site.

Routing changes are difficult to differentiate from changes in iceberg supply (calving) with only one core location. However, it is unlikely that the position of the polar front has moved across the core location. The mean temperature change across the PF over a 7-year period was measured to be 1.44°C by satellite sea surface temperature data across an average width of 43 km (Moore et al., 1999). The stable surface planktic $\delta^{18}O$ values (1σ STD=~0.3°C) exhibit no fluctuations of the PF or the SAF across the core site. The apparent stability of the PF and SAF is consistent with there being strong bathymetrical constraints on the position of PF and SAF (Talley, 2011), and thus argues against large changes the regional water flow paths and frontal positions at the core site. Nonetheless, one cannot rule out changes in ocean circulation pathways and eliminate routing as

influential on the IRD signal just yet. Additional information is needed in order to delineate routing and supply influences. Preferentially, a transect of cores would be analyzed through the iceberg alley. Differential variability along the transect would indicate varying position of 'iceberg alley' while coherent changes at all sites would indicate changes in iceberg generation.

7.1.4 Impact of melting icebergs

Icebergs have traditionally been rather understudied, so we are only now discovering how important they are and how they interact with the rest of the climate system. Smith et al. (2007), one of the pioneers in the field of "iceberg ecosystem", observed trails of phytoplankton following after melting icebergs, and postulated a connection between released terrigenous debris and changes in nutrient concentration (iron fertilization) and stimulated productivity in the pelagic zone (Chapter 2.3.2). The bloom of phytoplankton productivity around a melting iceberg, takes up lighter carbon (^{12}C) leaving the water enriched in $\delta^{13}C$. In regions where iceberg fertilization accounts for a significant fraction of the total productivity it would tend to drive higher $\delta^{13}C$ values in surface waters coincident with increased IRD input.

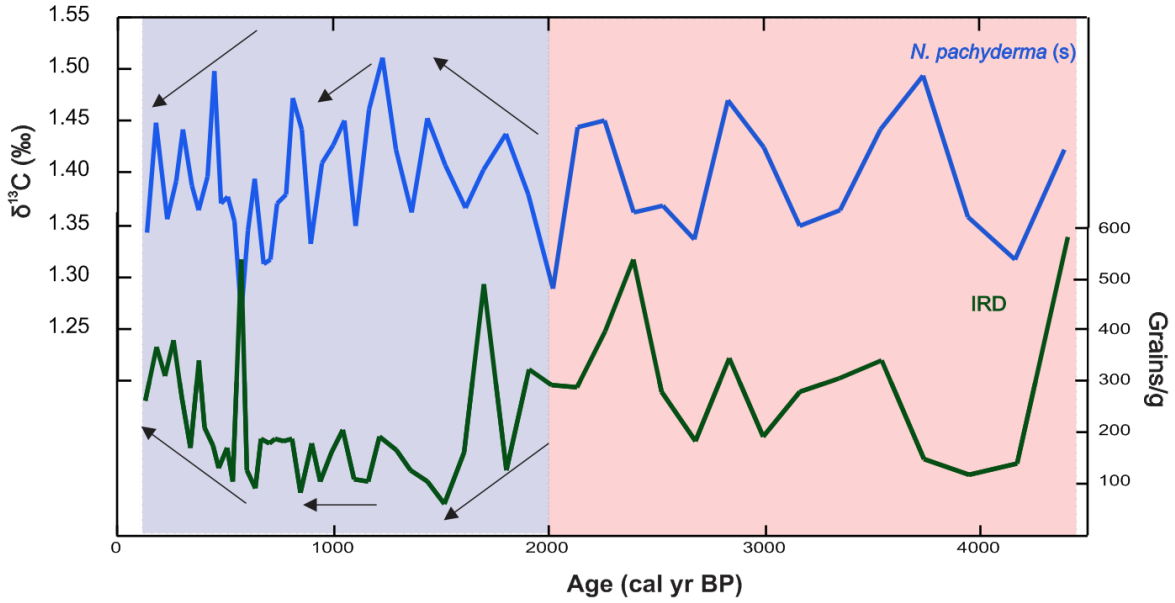

Figure 7.6: *N. pachyderma* (s) carbon isotope record (blue) and IRD record (green) from core GS08-151-02MC A. The pink box indicate when the records covary in phase with each other, and the purple box illustrate when the records are in antiphase.

The N. *pachyderma* (s) $\delta^{13}C$ and IRD record in Figure 7.6 show some, although not consistent, similarities. Less nutrient concentrations (increasing $\delta^{13}C$) occasionally correspond to enhanced input of IRD during the late Holocene period up until 2000 yr BP (pink box). After 2000 yr BP, there is more inconsistency in the records, indicated by trend arrows in opposite directions. The distinct IRD peak at ~600 yr BP coincides with a $\delta^{13}C$ minimum, implying low productivity, shows the opposite relationship that is expected if iceberg fertilization modulated productivity variations at the site. The rebound back to peak $\delta^{13}C$ levels at 460 yr BP, is dated to occur 100 years after the IRD peak, so this is unlikely to be related. Thus, the N. *pachyderma* (s) $\delta^{13}C$ record shows that periods of both enrichment and depletion of biological and chemical productivity in the pelagic zone are associated with icebergs. Thus, while it is possible that icebergs played a role in fertilizing productivity, the lack of a consistent $\delta^{13}C$-IRD covariance suggests that it was not the dominant influence regulating productivity through the late Holocene.

7.2 Regional climate change; sources and implications

The late Holocene climate changes in the WAIS region, discussed above, have been brought about by a number of different forcing mechanisms operating with relatively different strengths and on different time scales. These comprise the long-term influence of changes in orbital solar forcing and greenhouse gases superimposed on shorter-term changes in heat transport within the ocean and atmospheric system.

7.2.1 Global and regional climate connections

Interglacial variability in the deep Southern Ocean $\delta^{13}C$ signal implies that even relatively warm climates are not immune to rapid changes in THC (Ninnemann et al., 1999). It has been hypothesized that during the little ice age (LIA) lasting from about 650-100 yr BP (in the NH) the THC slowed down (Broecker, 2000). If true, one would predict a decrease in NADW input to the deep Southern Ocean (lowering CDW $\delta^{13}C$).

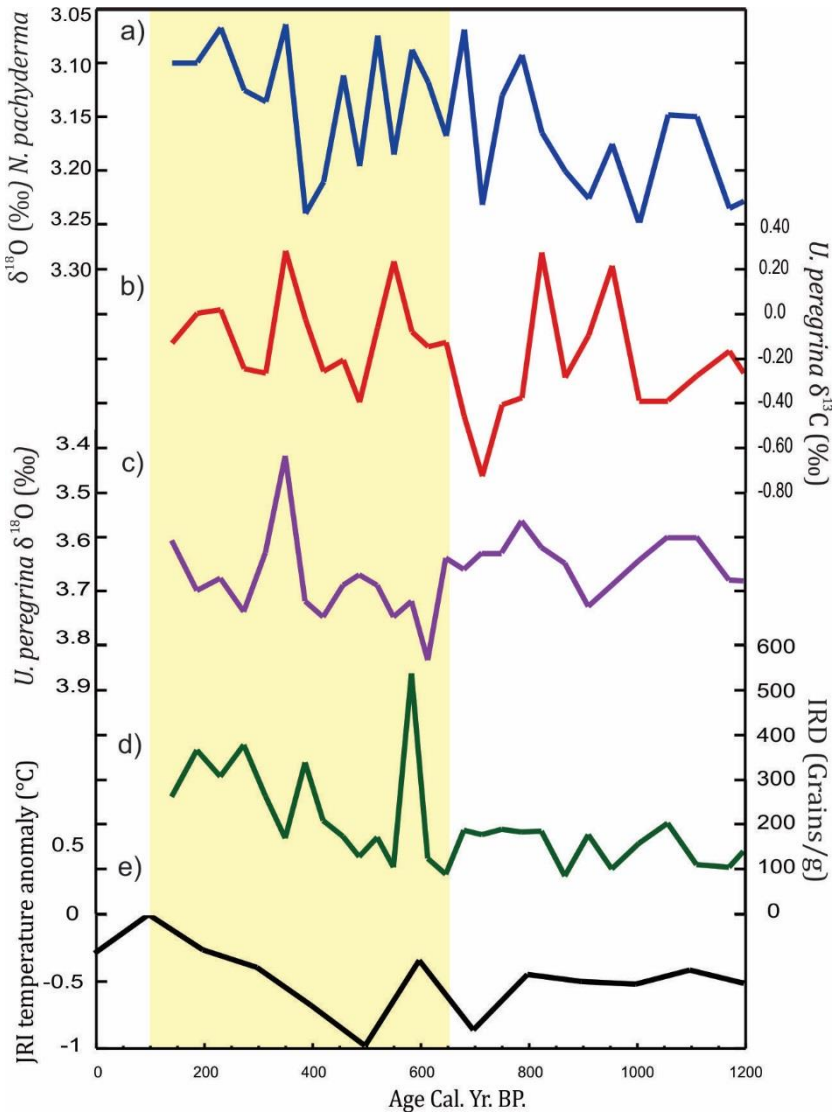

Figure 7.7: Comparison between planktic (surface)(a) and benthic (bottom)(b-c) water mass properties, IRD record(d) and temperature anomalies (e) at James Ross Island relative to the 1961-1990 mean (Mulvaney et al., 2012). The time interval of LIA (650-100 yr BP.) is marked by yellow box.

Since the multicore (GS08-151-02) is located in the Atlantic zone of the Southern Ocean, close to the depth of maximum NADW influence, a decrease in nutrients would accompany any increased inflow of low nutrient NADW, i.e. higher input of ^{13}C-enriched NADW. Hence, NADW input to the Southern Ocean can be used to track the strength of the THC (Stocker & Wright, 1991). Shown in Figure 7.7 are changes in local water mass properties (a-c) used to evaluate potential changes in the THC and its associated inter-hemispheric heat transport that could also influence IRD input (d) and JRI temperature (e).

The oxygen isotope record show a sharp decrease in both benthic (Δ0.28‰) and planktic (Δ0.17‰) $\delta^{18}O$ between 391-355 yr BP. The bottom water $\delta^{18}O$ change is equivalent to a warming or salinity change of 1.1°C or 0.47 psu, over the course of 36 years. The similar decrease in planktic $\delta^{18}O$ (0.73°C /0.3 psu) suggests that this warming extended throughout the water column, with the deep water warming more than the surface ocean. The (bottom water) U. *peregrina* $\delta^{13}C$ record (Figure 7.7 b) documents high frequency variability during this period on multidecadal to centennial time scales. The record exhibits four high $\delta^{13}C$ peaks during the last millennium, which could indicate greater NADW influence. Between these peaks is a rapid and strong minimum in U. *peregrina* $\delta^{13}C$ occurring around 700 yr BP, potentially indicating lower influence of NADW to the core site, prior to the onset of LIA in the NH. However, increased photosynthetic fractionation in the Weddell Sea where AABW is formed (Mackensen et al., 1996) could also explain the peaks in *U. peregrina* $\delta^{13}C$. Finally, *U perigrina* $\delta^{13}C$ is also infaunal and is influenced by pore water modification of $\delta^{13}C$ through oxidation of organic matter. Thus, because the core site is influenced both by AABW and NADW (Figure 3.3), the significance of the low $\delta^{13}C$ values remains ambiguous. A high resolution record of epifaunal $\delta^{13}C$ (e.g. *C. wuellerstorfi*) would provide additional constraints as this species habitat, above the pore water, and may more accurately reflect bottom water changes. Thus, while more work is required, there is currently no clear evidence for a change in bottom water chemistry consistent with a decrease in THC during the LIA.

Antiphasing, between the hemispheres, of climate oscillations during the deglaciation is tied to changes in THC (Broecker, 1998). According to this idea of the bipolar seesaw effect, one would expect the Southern Ocean region to warm corresponding to a NH cooling and THC slowdown (Charles et al., 1996). In a regional context, the JRI temperature record (Mulvaney et al., 2012) and my IRD record indicate cooler conditions and less calving from the AP at the onset of the LIA around 650 yr BP, with increasing temperature and IRD input throughout the period. There is a peak in IRD abundance right at the onset of LIA. When the errors about the bracketing calibrated ages are propagated, the age range of the IRD peak falls between 530 and 650 yr BP. This IRD peak appears to coincide with one of the extremes in the LIA in the NH at about 1450 AD, when it was very cold, possibly due in part to solar and volcanic co-forcing, at this time.

In summary, although there are some interesting fluctuations in the presented data (Figure 7.7), particularly at the onset of the LIA, overall the records do not document a clear, consistent, and persistent signal for the LIA. Part of the mismatch with expected signals may arise from the uncertainties (presented by the error bars, Chapter 6) and individual differences between the records due to the possible dating errors or time lag of the infaunal benthic foraminifera, consequently the LIA impact in the region remain undefined. However, as noted above, the local climate changes (benthic and planktic $\delta^{18}O$) show very small changes, which are close to the noise threshold for the records. Thus, the coherence with global climate signals may not be the most revealing point. Instead, the overall stability suggests that this region did not experience large variability and thus the record is inconsistent with any mechanism that should drive clear variability at the core site. This includes large reductions in THC which, in models, tends to drive circum-Antarctic warming (Broecker, 1998), including in the region of the core site.

Other records do provide clearer evidence for regional SH climate variability during the LIA. Ice cores from the WAIS divide (Orsi et al., 2012) and SST reconstructions (ODP site 1098) at west Antarctic Peninsula (Shevenell et al., 2011) document cooling during the LIA, which is opposite to the bipolar antiphasing expected if THC were driving the signal. In addition, the Hamberg overspill glacier on South Georgia rapidly retreated behind its present-day position from 500 yr BP (van der Bilt et al., 2017). The out of phase response in different regions and the much smaller magnitude in the SH signal, does not support a coherent and globally synchronous SH response during the LIA. The contrasting patterns with the polar records getting colder during the LIA and the subpolar (APFZ) getting warmer, can be linked to shifts in regional atmospheric and oceanic circulation patterns (Shevenell et al., 2011; Abram et al., 2014) mainly attributed to changes in SAM (Marshall et al., 2003; Moy et al., 2008). There has been a trend towards more positive SAM, increasing wind strengths (Figure 7.5 b) and thus an enhanced Antarctic dipole effect. The Antarctic dipole can explain the opposite temperature trends between west AP (ODP site 1089)(Shevenell et al., 2011) and east AP at JRI (Mulvaney et al., 2012) the last 2200 yr, illustrated by arrows in Figure 7.8. Thus our record, together with regional records do not show the coherent circumpolar changes expected due to large THC variability during the LIA. Instead, a dipole pattern of climate variability suggests atmospheric changes (SAM) may have been more influential in driving climate variability over the past millennium.

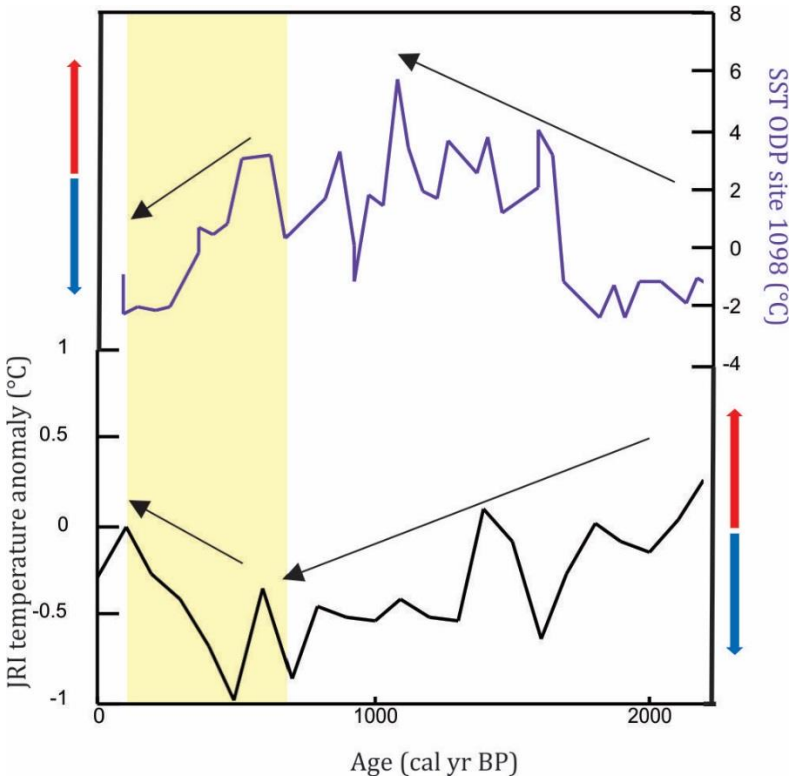

Figure 7.8: Shows SST trends at ODP site 1098 from the west side of the Antarctic Peninsula (Shevenell et al., 2011) compared with temperature anomalies from JRI on the east side of the Antarctic Peninsula (Mulvaney et al., 2012). The time interval of LIA (650-100 yr BP.) is marked by yellow box. The Blue and red arrows indicate cooling and warming respectively.

7.2.2 Perspective to recent rapid regional warming and future warming

Here I discuss how the GS08-151-02 MC high-resolution records, characterizing the natural variability of climate, ocean circulation, and ice sheet behavior through the late Holocene provide perspective for understanding how recent climate-ocean changes compare to current trends in the Southern Ocean. The N. *pachyderma* (sin.) $\delta^{18}O$ records monitoring near surface temperature and salinity, suggest that near surface ocean properties between the PF and the SAF have been remarkably stable over the past ~4200 years. The standard deviation from the mean of the record is 0.073‰ (1σ STD), equivalent to a change in temperature of 0.31°C or a salinity change of 0.13 psu.

By contrast to this apparent late Holocene stability the Antarctic Peninsula has warmed by 2.94°C over the last 50 years; significantly more than the global average of 0.52°C (Hansen et al., 2010) (Figure 7.8). Surface climate changes are rapidly transmitted into

the ocean interior in the Antarctic region. Indeed, most of the heating of the Earth climate system since the 1950's is concentrated in the world ocean (Levitus et al., 2005). The ocean has warmed substantially during this time period at all (mean) depths (Gille, 2008). In fact, the subsurface Southern Ocean seems to have warmed faster than any other part of the world oceans (Robertson et al., 2002). The warming is concentrated within the Antarctic Circumpolar Current (ACC), and the strong trend in the Southern Ocean appears regionally consistent with the poleward migration of the ACC. This migration is driven by a poleward shift of the SWW, related to the shift in the southern annular mode (Gille, 2008) (Chapter 7.1.2). Strengthening of the SWW over the past 50 years has been linked to stratospheric ozone depletion. Ozone in the stratosphere absorbs incoming insolation from the sun, thus with less ozone leads to less absorption and cooling in the upper atmosphere. This increases the temperature gradient strengthening westerly winds, leading to positive SAM (Arblaster & Meehl, 2006). Marshall et al., (2004) shows in GCM simulations that observed trends in the SAM are consistent with the combined effects of anthropogenic and natural forcing.

Hansen et al., (2010) carried out analyses of global sea surface temperature (SST) variability based on historic shipboard measurements collected between 1900 and 1982 AD, and satellite measurements from 1982 until present. Figure 7.9 show a plot of the changes in SST over the last 100 years, illustrating the average temperature change of >0.6- 1^{o}C in the region of the core site. This warming trend is consistent with SST measurements near South Georgia by Whitehouse et al. (2008) quantifying almost year-round temperature changes over an 81-year period (1925-2006). In the top 100 meters of the water column they found a mean increase in temperature of ~0.9^{o}C in January (summer) and ~2.3^{o}C in August (winter).

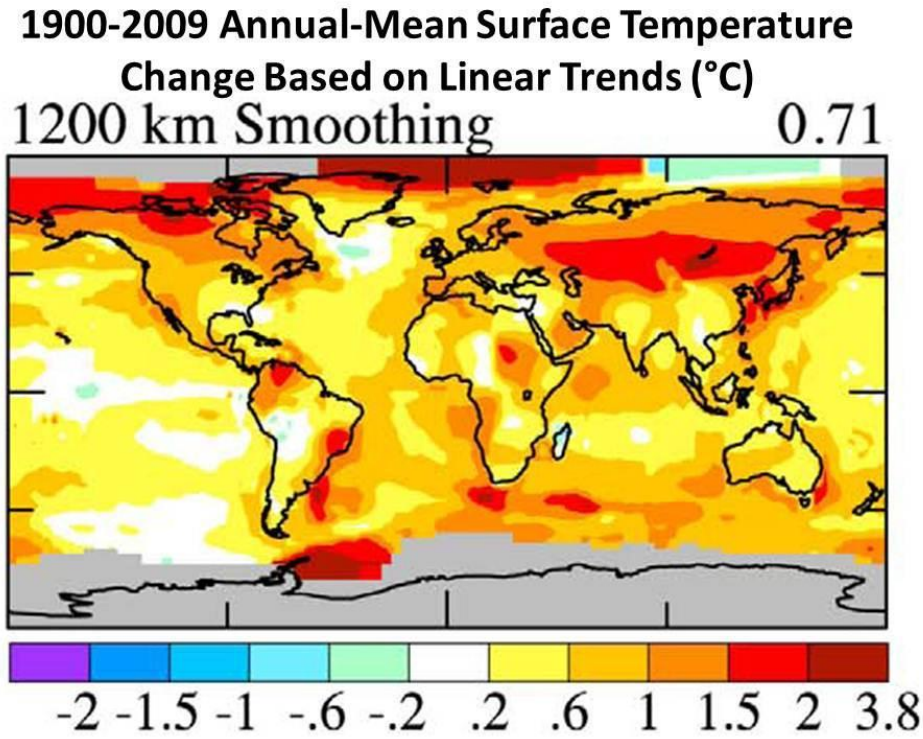

Figure 7.9: Plot of the regional changes in sea surface temperature over the last century, after Hansen et al., (2010).

The ice core record from JRI (Mulvaney et al., 2012) showed that warming of the northern Antarctic Peninsula (JRI) began 600 yr BP, with the recent phase of warming starting in the 1920s. The high rate of warming over the past century, reaching 1.56°C, is unusual in the context of natural climate variability over the past two millennia (Mulvaney et al., 2012). Figure 7.9 also shows the recent regional warming in Antarctic Peninsula as one of the fastest-warming regions on Earth: 3.4°C/century (Vaughan et al., 2003). Observations of rapid and ongoing glacial retreat have been observed across the globe (Oerlemans, 2005) as well in the region of the study area. Glacial retreat in South Georgia (Gordon et al., 2008; van der Bilt et al., 2017), Antarctic Peninsula (Cook et al., 2016), in Patagonia (Glasser et al., 2011) and throughout the southern hemisphere (Solomina et al., 2016) are in line with the recent rapid warming (Vaughan et al., 2003).

Relative to the late Holocene natural variability documented in this study, the rate and magnitude of warming observed recently in the region is highly unusual. The recent SST warming of 0.9°C (Whitehouse et al., 2008; Hansen et al., 2010) equals a 3σ STD event in the *N. pachyderma* (s) $\delta^{18}O$ record. Thus, the recent rapid SST increase exceeds the

background range (1σ STD = 0.3°C) of natural variability and has a 99.7% (3σ) probability that it was not caused by natural variability. Hence, any further warming of the Southern Ocean will move even more clearly beyond the range of natural variability observed over the past ~4200 years. This strongly supports a role for anthropogenic forcing (as extremely likely), in driving 20th century warming in this region.

7.2.3 Consequence of future warming

Continued anthropogenic driven global temperature rise and strengthening of the SWW can dramatically increase the temperature of ocean water at ice sheet grounding lines and at the base of floating ice shelves around Antarctica. If this occurs ice sheets might start to deteriorate with potentially significant ramifications for global sea level rise. These changes would be of particular concern because large portions of the marine based WAIS are prone to melting and ice shelf retreat could thus further accelerate future sea level rise (chapter 2.3).

In 2016, melting of the West Antarctica and Antarctic Peninsula together with Greenland and East Antarctica contributed 0.59 ± 0.20 mm/year to the global mean sea level rise (DeConto & Pollard, 2016). Antarctic mass loss seems to be accelerating and will most likely continue to increase in the future, when relatively warm CDW will be able to reach the southernmost ice shelves (Hellmer et al., 2012). DeConte and Pollard (2016) state roughly in their worst-case scenario (with model coupling ice sheet and climate dynamics), that sea level could rise by 1.8 meters by the end of this century, and the pace could pick up drastically in the 22nd century, if emissions continue unabated. Consequently, immense land areas will most likely have to be abandoned, by civilization, to the rising sea.

7.3 Summary of conclusions

- Surface ocean properties in the Scotia Sea are remarkably stable in the late Holocene. With surface water property changes (planktic $\delta^{18}O$) out of phase compared to IRD input it is unlikely that climate drove the IRD variability.
- The available evidence suggests that warming at the east AP (JRI) coincides with increased IRD at the core site, pointing toward increased calving and supply of icebergs as the main driver in past variability. Routing, due to shifts in wind patterns and gyre circulation, may also play a role. Additional records (across the axis of 'iceberg alley') would be useful to delineate calving vs. routing
- The synchronicity between the IRD record, the SWW reconstructions and JRI temperature variability is similar to present day climate teleconnections linking atmospheric circulation, the Southern Ocean circulation and the WAIS. The stronger and poleward contracted SWW belt draws warmer CDW up under the ice sheet. Where the warm water comes into contact with the ice shelf base it creates basal melting and retreat of the grounding line, consequently thinning the ice shelf, making it less able to buttress the upstream ice-sheet, triggering accelerated glacier flow.
- The records do not document a clear, consistent, and persistent signal of an interhemispheric bipolar seesaw during the LIA, nor more generally during the late Holocene. The lack of a coherent Southern Ocean response argues against a major role for THC in driving interhemispheric climate signals over the LIA.
- Recent warming trends are 3 standard deviations beyond the range of natural variability (at the 99.7 percentile). This strongly supports a role for anthropogenic forcing in driving recent changes.

In conclusion, IRD varied on centennial to millennial timescales during the late Holocene most likely driven by WAIS discharge and/or wind driven routing of icebergs. There is a clear coupling between climate, ocean circulation, and the ongoing WAIS changes. Similar relationships can explain the pattern observed in the past with periods of warm AP associated with more iceberg discharge due to increased CDW influence driving AP warming and basal melt. The anomalously large and rapid recent warming relative to natural variability of the past raises concern for the future evolution of AP and the WAIS generally. The marine based WAIS, positioned on reversed slopes, makes it highly

susceptible to perturbation by increased CDW (due to contracting SWW belt) and surface melt. Thinning ice shelves and loss of buttressing could have severe consequences for future sea level rise, ocean overturning circulation, and ocean carbon sequestration.

Unfortunately there are very few comparable records to those presented in this thesis with which to build a more coherent regional and Southern Ocean picture of late Holocene ocean-ice-climate evolution. Additional records, for example transecting the iceberg alley could help to more accurately delineate the ultimate mechanism behind the observed IRD variability and provide a better characterization of regional climate and deep circulation responses. Ultimately, such records are necessary for elucidating climate-ice coupling and identifying any tipping points in the ice sheet. This empirical basis for understanding of ice-ocean-climate interactions is necessary for testing models and to accurately predict future ice-climate evolution.

8 References

Abram, N. J., Mulvaney, R., Vimeux, F., Phipps, S. J., Turner, J., & England, M. H. (2014). Evolution of the Southern Annular Mode during the past millennium. *Nature Clim. Change, 4*(7), 564-569. doi:10.1038/nclimate2235

http://www.nature.com/nclimate/journal/v4/n7/abs/nclimate2235.html#supplementary-information

Allen, C. S., Pike, J., Pudsey, C. J., & Leventer, A. (2005). Submillennial variations in ocean conditions during deglaciation based on diatom assemblages from the southwest Atlantic. *Paleoceanography, 20*(2).

Alley, R. B., Anandakrishnan, S., Christianson, K., Horgan, H. J., Muto, A., Parizek, B. R., . . . Walker, R. T. (2015). Oceanic forcing of ice-sheet retreat: West Antarctica and more. *Annual Review of Earth and Planetary Sciences, 43*, 207-231.

Anderson, D. M. (2001). Attenuation of millennial‐scale events by bioturbation in marine sediments. *Paleoceanography, 16*(4), 352-357.

Arblaster, J. M., & Meehl, G. A. (2006). Contributions of external forcings to southern annular mode trends. *Journal of Climate, 19*(12), 2896-2905.

Bakker, P., Clark, P. U., Golledge, N. R., Schmittner, A., & Weber, M. E. (2017). Centennial-scale Holocene climate variations amplified by Antarctic Ice Sheet discharge. *Nature, 541*(7635), 72-76.

Barker, P. F., Dalziel, I. W. D., & Storey, B. C. (1991). Tectonic development of the Scotia Arc region. *The geology of Antarctica, 6*, 215-248.

Bauch, D., Carstens, J., & Wefer, G. (1997). Oxygen isotope composition of living Neogloboquadrina pachyderma (sin.) in the Arctic Ocean. *Earth and Planetary Science Letters, 146*(1), 47-58.

Bentley, C. R., & Ostenso, N. A. (1961). Glacial and subglacial topography of West Antarctica. *Journal of Glaciology, 3*(29), 882-911.

Berger, W. H., Killingley, J. S., & Vincent, E. (1978). Sable isotopes in deep-sea carbonates-box core erdc-92, west equatorial pacific. *Oceanologica Acta, 1*(2), 203-216.

BIAC. (2017). Bipolar Atlantic Thermohaline Circulation. Retrieved from http://www.uib.no/sites/w3.uib.no/files/w2/bi/biacillustration1_1.jpg

Bigeleisen, J. (1965). Chemistry of isotopes. *Science, 147*(3657), 463-471.

Bijma, J., Spero, H., & Lea, D. (1999). Reassessing foraminiferal stable isotope geochemistry: Impact of the oceanic carbonate system (experimental results) *Use of proxies in paleoceanography-Examples from the South Atlantic (G Fischer, G Wefer, eds) Springer, Berlin, Heidelberg* (pp. 489-512).

Bintanja, R., Van Oldenborgh, G., Drijfhout, S., Wouters, B., & Katsman, C. (2013). Important role for ocean warming and increased ice-shelf melt in Antarctic sea-ice expansion. *Nature geoscience, 6*(5), 376-379.

Blaauw, M. (2010). Methods and code for 'classical'age-modelling of radiocarbon sequences. *quaternary geochronology, 5*(5), 512-518.

Boltovsky, E., & Wright, R. (1976). *Recent foraminifera*: W. Junk.

Bond, G., Heinrich, H., Broecker, W., Labeyrie, L., McManus, J., Andrews, J., . . . Simet, C. (1992). Evidence for massive discharges of icebergs into the North Atlantic ocean during the last glacial period.

Bond, G. C., & Lotti, R. (1995). Iceberg discharges into the North Atlantic on millennial time scales during the last glaciation. *Science, 267*(5200), 1005.

Brachfeld, S., Domack, E., Kissel, C., Laj, C., Leventer, A., Ishman, S., . . . Eglinton, L. B. (2003). Holocene history of the Larsen-A Ice Shelf constrained by geomagnetic paleointensity dating. *Geology, 31*(9), 749-752.

Broecker, W. S. (1992). *The great ocean conveyor.* Paper presented at the AIP Conference Proceedings.

Broecker, W. S. (1994). Massive iceberg discharges as triggers for global climate change. *Nature, 372*, 421-424.

Broecker, W. S. (1998). Paleocean circulation during the last deglaciation: a bipolar seesaw? *Paleoceanography, 13*(2), 119-121.

Broecker, W. S. (2000). Was a change in thermohaline circulation responsible for the Little Ice Age? *Proceedings of the National Academy of Sciences, 97*(4), 1339-1342.

Broecker, W. S., & Denton, G. H. (1989). The role of ocean-atmosphere reorganizations in glacial cycles. *Geochimica et Cosmochimica Acta, 53*(10), 2465-2501.

Broecker, W. S., Sutherland, S., & Peng, T.-H. (1999). A possible 20th-century slowdown of Southern Ocean deep water formation. *Science, 286*(5442), 1132-1135.

Carmack, E. C., & Foster, T. D. (1977). Water masses and circulation in the Weddell Sea. *Polar Oceans*, 151-165.

Charles, C. D., Lynch-Stieglitz, J., Ninnemann, U. S., & Fairbanks, R. G. (1996). Climate connections between the hemisphere revealed by deep sea sediment core/ice core correlations. *Earth and Planetary Science Letters, 142*(1-2), 19-27.

Charles, C. D., Wright, J. D., & Fairbanks, R. G. (1993). Thermodynamic influences on the marine carbon isotope record. *Paleoceanography, 8*(6), 691-697.

Ciais, P., Sabine, C., Bala, G., Bopp, L., Brovkin, V., Canadell, J., . . . Thornton, P. (2013). Carbon and Other Biogeochemical Cycles. In T. F. Stocker, D. Qin, G.-K. Plattner, M.

Tignor, S. K. Allen, J. Boschung, A. Nauels, Y. Xia, V. Bex, & P. M. Midgley (Eds.), *Climate Change 2013: The Physical Science Basis. Contribution of Working Group I to the Fifth Assessment Report of the Intergovernmental Panel on Climate Change* (pp. 465–570). Cambridge, United Kingdom and New York, NY, USA: Cambridge University Press.

Clark, I. D., & Fritz, P. (1997). *Environmental isotopes in hydrogeology*: CRC press.

Compton, R. R., & Compton, R. (1985). *Geology in the Field*: Wiley New York.

Cook, A. J., Holland, P. R., Meredith, M. P., Murray, T., Luckman, A., & Vaughan, D. G. (2016). Ocean forcing of glacier retreat in the western Antarctic Peninsula. *Science, 353*(6296), 283-286.

Coplen, T. B., Kendall, C., & Hopple, J. (1983). Comparison of stable isotope reference samples.

Coxall, H. K., Wilson, P. A., Pälike, H., Lear, C. H., & Backman, J. (2005). Rapid stepwise onset of Antarctic glaciation and deeper calcite compensation in the Pacific Ocean. *Nature, 433*(7021), 53-57.

Crepon, M., Houssais, M. N., & Guily, B. S. (1988). The drift of icebergs under wind action. *Journal of Geophysical Research: Oceans, 93*(C4), 3608-3612.

Cronin, T. M. (2009). *Paleoclimates: understanding climate change past and present*: Columbia University Press.

Curry, J. A., Schramm, J. L., & Ebert, E. E. (1995). Sea ice-albedo climate feedback mechanism. *Journal of Climate, 8*(2), 240-247.

Curry, W. B., Duplessy, J.-C., Labeyrie, L. D., & Shackleton, N. J. (1988). Changes in the distribution of δ13C of deep water ΣCO2 between the last glaciation and the Holocene. *Paleoceanography, 3*(3), 317-341.

Darling, K. F., Kucera, M., Kroon, D., & Wade, C. M. (2006). A resolution for the coiling direction paradox in Neogloboquadrina pachyderma. *Paleoceanography, 21*(2).

Deacon, M. C. (1933). A general account of the hydrology of the South Atlantic Ocean.—"Discovery" Rep.

DeConto, R. M., & Pollard, D. (2016). Contribution of Antarctica to past and future sea-level rise. *Nature, 531*(7596), 591-597.

Deevey, E. S., & Flint, R. F. (1957). Postglacial hypsithermal interval. *Science, 125*(3240), 182-184.

Denton, G. H., & Karlén, W. (1973). Holocene climatic variations—their pattern and possible cause. *Quaternary research, 3*(2), 155IN1175-1174IN2205.

Domack, Duran, D., Leventer, A., Ishman, S., Doane, S., McCallum, S., . . . Prentice, M. (2005). Stability of the Larsen B ice shelf on the Antarctic Peninsula during the Holocene epoch. *Nature, 436*(7051), 681-685.

Domack, E., Leventer, A., Dunbar, R., Taylor, F., Brachfeld, S., & Sjunneskog, C. (2001). Chronology of the Palmer Deep site, Antarctic Peninsula: a Holocene palaeoenvironmental reference for the circum-Antarctic. *The Holocene, 11*(1), 1-9.

Donner, B., & Wefer, G. (1994). Flux and stable isotope composition of Neogloboquadrina pachyderma and other planktonic foraminifers in the Southern Ocean (Atlantic sector). *Deep Sea Research Part I: Oceanographic Research Papers, 41*(11), 1733-1743.

Drewry, D. J. (1983). The surface of the Antarctic ice sheet. *Antarctica: Glaciological and Geophysical Folio*.

Dunn, S. (Producer). (2008, 23.11.2016). Gas Source Mass Spectrometry: Stable Isotope Geochemistry. Retrieved from http://serc.carleton.edu/research_education/geochemsheets/techniques/gassourcemassspec.html

Duplessy, J.-C., Shackleton, N. J., Matthews, R. K., Prell, W., Ruddiman, W. F., Caralp, M., & Hendy, C. H. (1984). 13C record of benthic foraminifera in the last interglacial ocean: implications for the carbon cycle and the global deep water circulation. *Quaternary Research, 21*(2), 225-243.

Echols, R. (1967). DISTRIBUTION OF FORAMINIFERA AND RADIOLARIA IN SEDIMENTS OF THE SCOTIA SEA AREA, ANTARCTIC OCEAN: ProQuest Dissertations Publishing.

Eide, M., Olsen, A., Ninnemann, U. S., & Johannessen, T. (2017). A global ocean climatology of preindustrial and modern ocean δ13C. *Global Biogeochemical Cycles, 31*(3), 515-534.

Ellison, C. R., Chapman, M. R., & Hall, I. R. (2006). Surface and deep ocean interactions during the cold climate event 8200 years ago. *Science, 312*(5782), 1929-1932.

Epstein, S., Buchsbaum, R., Lowenstam, H. A., & Urey, H. C. (1953). Revised carbonate-water isotopic temperature scale. *Geological Society of America Bulletin, 64*(11), 1315-1326.

Ericson, D. B. (1959). Coiling Direction of Globigerina pachyderma as a Climatic Index. *Science, 130*(3369), 219-220. doi:10.1126/science.130.3369.219

Fairbanks, R. G., Mortlock, R. A., Chiu, T.-C., Cao, L., Kaplan, A., Guilderson, T. P., . . . Nadeau, M.-J. (2005). Radiocarbon calibration curve spanning 0 to 50,000 years BP based on paired 230 Th/234 U/238 U and 14 C dates on pristine corals. *Quaternary Science Reviews, 24*(16), 1781-1796.

Faure, G., & Mensing, T. M. (2005). *Isotopes: principles and applications*: John Wiley & Sons Inc.

Favier, L., Durand, G., Cornford, S. L., Gudmundsson, G. H., Gagliardini, O., Gillet-Chaulet, F., . . . Le Brocq, A. M. (2014). Retreat of Pine Island Glacier controlled by marine ice-sheet instability. *Nature Climate Change, 4*(2), 117-121.

Fletcher, J. O. (1969). Ice extent on the Southern Ocean and its relation to world climate.

Fontanier, C., Mackensen, A., Jorissen, F. J., Anschutz, P., Licari, L., & Griveaud, C. (2006). Stable oxygen and carbon isotopes of live benthic foraminifera from the Bay of Biscay: Microhabitat impact and seasonal variability. *Marine Micropaleontology, 58*(3), 159-183.

Fretwell, P., Pritchard, H. D., Vaughan, D. G., Bamber, J., Barrand, N., Bell, R., . . . Casassa, G. (2013). Bedmap2: improved ice bed, surface and thickness datasets for Antarctica. *The Cryosphere, 7*(1).

Fürst, J. J., Durand, G., Gillet-Chaulet, F., Tavard, L., Rankl, M., Braun, M., & Gagliardini, O. (2016). The safety band of Antarctic ice shelves. *Nature Climate Change, 6*(5), 479-482.

Gareth, J. M., Andrew, O., Nicole, P. M. v. L., & John, C. K. (2006). The Impact of a Changing Southern Hemisphere Annular Mode on Antarctic Peninsula Summer Temperatures. *Journal of Climate, 19*(20), 5388-5404. doi:10.1175/jcli3844.1

Gille, S. T. (2002). Warming of the Southern Ocean since the 1950s. *Science, 295*(5558), 1275-1277.

Gille, S. T. (2008). Decadal-scale temperature trends in the Southern Hemisphere ocean. *Journal of Climate, 21*(18), 4749-4765.

Glasser, N., Harrison, S., Jansson, K. N., Anderson, K., & Cowley, A. (2011). Global sea-level contribution from the Patagonian Icefields since the Little Ice Age maximum. *Nature Geoscience, 4*(5), 303-307.

Gordon, A. L. (1971). *Antarctic polar front zone*: Wiley Online Library.

Gordon, A. L. (1971). *Oceanography of Antarctic waters*: Wiley Online Library.

Gordon, J. E., & Harkness, D. D. (1992). Magnitude and geographic variation of the radiocarbon content in Antarctic marine life: implications for reservoir corrections in radiocarbon dating. *Quaternary Science Reviews, 11*(7-8), 697-708.

Gordon, J. E., Haynes, V. M., & Hubbard, A. (2008). Recent glacier changes and climate trends on South Georgia. *Global and Planetary Change, 60*(1), 72-84.

Gouretski, V. V., & Koltermann, K. P. (2004). Berichte des Bundesamtes für Seeschifffahrt und Hydrographie: Nr.

Grose, T. J., Johnson, J. A., & Bigg, G. R. (1995). A comparison between the FRAM (Fine Resolution Antarctic Model) results and observations in the Drake Passage. *Deep Sea Research Part I: Oceanographic Research Papers, 42*(3), 365-388.

Grossman, E. L. (1987). Stable isotopes in modern benthic foraminifera; a study of vital effect. *The Journal of Foraminiferal Research, 17*(1), 48-61.

Hansen, J., Ruedy, R., Sato, M., & Lo, K. (2010). Global surface temperature change. *Reviews of Geophysics, 48*(4).

Hays, J. D., Imbrie, J., & Shackleton, N. J. (1976). *Variations in the Earth's orbit: pacemaker of the ice ages*.

Heinrich, H. (1988). Origin and consequences of cyclic ice rafting in the northeast Atlantic Ocean during the past 130,000 years. *Quaternary research, 29*(2), 142-152.

Hellmer, H. H., Kauker, F., Timmermann, R., Determann, J., & Rae, J. (2012). Twenty-first-century warming of a large Antarctic ice-shelf cavity by a redirected coastal current. *Nature, 485*(7397), 225-228.

Hemming, S. R. (2004). Heinrich events: Massive late Pleistocene detritus layers of the North Atlantic and their global climate imprint. *Reviews of Geophysics, 42*(1).

Hodell, D. A., Evans, H. F., Channell, J. E., & Curtis, J. H. (2010). Phase relationships of North Atlantic ice-rafted debris and surface-deep climate proxies during the last glacial period. *Quaternary Science Reviews, 29*(27), 3875-3886.

Hodell, D. A., Kanfoush, S. L., Shemesh, A., Crosta, X., Charles, C. D., & Guilderson, T. P. (2001). Abrupt cooling of Antarctic surface waters and sea ice expansion in the South Atlantic sector of the Southern Ocean at 5000 cal yr BP. *Quaternary Research, 56*(2), 191-198.

Hoefs, J. (2009). *Stable isotope geochemistry* (6th. ed. ed.). Berlin: Springer.

Hofmann, E. E., Klinck, J. M., Lascara, C. M., & Smith, D. A. (1996). *Water mass distribution and circulation west of the Antarctic Peninsula and including Bransfield Strait*: Wiley Online Library.

Howe, J. A., & Pudsey, C. J. (1999). Antarctic circumpolar deep water: a Quaternary paleoflow record from the northern Scotia Sea, South Atlantic Ocean. *Journal of Sedimentary Research, 69*(4).

Jacobs, S., Gordon, A., & Amos, A. (1979). Effect of glacial ice melting on the Antarctic surface water. *Nature, 277*(5696), 469-471.

Jacobs, S. S., Jenkins, A., Giulivi, C. F., & Dutrieux, P. (2011). Stronger ocean circulation and increased melting under Pine Island Glacier ice shelf. *Nature geoscience, 4*(8), 519-523.

JAMSTEC. (2014, October 27, 2014). Retrieved from http://www.jamstec.go.jp/e/about/press_release/20141027/

Jenkins, A., Dutrieux, P., Jacobs, S. S., McPhail, S. D., Perrett, J. R., Webb, A. T., & White, D. (2010). Observations beneath Pine Island Glacier in West Antarctica and implications for its retreat. *Nature geoscience, 3*(7), 468-472.

Jonkers, L., Brummer, G. J. A., Peeters, F. J. C., van Aken, H. M., & De Jong, M. F. (2010). Seasonal stratification, shell flux, and oxygen isotope dynamics of left‐coiling N. pachyderma and T. quinqueloba in the western subpolar North Atlantic. *Paleoceanography, 25*(2).

Jorissen, F. J. (1999). Benthic foraminiferal microhabitats below the sediment-water interface *Modern foraminifera* (pp. 161-179): Springer.

Joughin, I., & Alley, R. B. (2011). Stability of the West Antarctic ice sheet in a warming world. *Nature Geoscience, 4*(8), 506-513.

Joughin, I., Smith, B. E., & Medley, B. (2014). Marine ice sheet collapse potentially under way for the Thwaites Glacier Basin, West Antarctica. *Science, 344*(6185), 735-738.

Kanfoush, S. L., Hodell, D. A., Charles, C. D., Guilderson, T. P., Mortyn, P. G., & Ninnemann, U. S. (2000). Millennial-scale instability of the Antarctic ice sheet during the last glaciation. *Science, 288*(5472), 1815-1819.

Kennett, J. P. (1977). Cenozoic evolution of Antarctic glaciation, the circum‐Antarctic Ocean, and their impact on global paleoceanography. *Journal of geophysical research, 82*(27), 3843-3860.

King, J., Turner, J., Marshall, G., Connolley, W., & Lachlan‐Cope, T. (2003). *Antarctic Peninsula climate variability and its causes as revealed by analysis of instrumental records*: Wiley Online Library.

Kleiven, H. K. F., Kissel, C., Laj, C., Ninnemann, U. S., Richter, T. O., & Cortijo, E. (2008). Reduced North Atlantic deep water coeval with the glacial Lake Agassiz freshwater outburst. *Science, 319*(5859), 60-64.

Klinck, J. M., Hofmann, E. E., Beardsley, R. C., Salihoglu, B., & Howard, S. (2004). Water-mass properties and circulation on the west Antarctic Peninsula Continental Shelf in Austral Fall and Winter 2001. *Deep Sea Research Part II: Topical Studies in Oceanography, 51*(17), 1925-1946.

Kohfeld, K. E., Fairbanks, R. G., Smith, S. L., & Walsh, I. D. (1996). Neogloboquadrina pachyderma (sinistral coiling) as paleoceanographic tracers in polar oceans: Evidence from Northeast Water Polynya plankton tows, sediment traps, and surface sediments. *Paleoceanography, 11*(6), 679-699.

Kroopnick, P. (1985). The distribution of 13 C of ΣCO 2 in the world oceans. *Deep Sea Research Part A. Oceanographic Research Papers, 32*(1), 57-84.

Kuhlbrodt, T., Griesel, A., Montoya, M., Levermann, A., Hofmann, M., & Rahmstorf, S. (2007). On the driving processes of the Atlantic meridional overturning circulation. *Reviews of Geophysics, 45*(2).

Lamy, F., Hebbeln, D., Röhl, U., & Wefer, G. (2001). Holocene rainfall variability in southern Chile: a marine record of latitudinal shifts of the Southern Westerlies. *Earth and Planetary Science Letters, 185*(3), 369-382.

Lawver, L. A., Gahagan, L. M., & Coffin, M. F. (1992). The development of paleoseaways around Antarctica. *The Antarctic Paleoenvironment: A Perspective on Global Change: Part One*, 7-30.

Levitus, S., Antonov, J., & Boyer, T. (2005). Warming of the world ocean, 1955–2003. *Geophysical Research Letters, 32*(2).

Libby, W. F. (1961). Radiocarbon dating. *Science See Saiensu, 133*.

Libby, W. F., Anderson, E. C., & Arnold, J. R. (1949). Age determination by radiocarbon content: world-wide assay of natural radiocarbon. *Science, 109*(2827), 227-228.

Liu, J., Curry, J. A., & Martinson, D. G. (2004). Interpretation of recent Antarctic sea ice variability. *Geophysical Research Letters, 31*(2).

Liu, Y., Moore, J. C., Cheng, X., Gladstone, R. M., Bassis, J. N., Liu, H., . . . Hui, F. (2015). Ocean-driven thinning enhances iceberg calving and retreat of Antarctic ice shelves. *Proceedings of the National Academy of Sciences, 112*(11), 3263-3268.

Lowe, J. J., & Walker, M. J. C. (1984). Reconstructing Quaternary Environments.

Lowe, J. J., & Walker, M. J. C. (2014). *Reconstructing Quaternary Environments* (2nd ed. ed.). Hoboken: Taylor and Francis.

Lythe, M. B., & Vaughan, D. G. (2001). BEDMAP: A new ice thickness and subglacial topographic model of Antarctica. *Journal of Geophysical Research: Solid Earth, 106*(B6), 11335-11351.

Mackensen, A., Hubberten, H. W., Bickert, T., Fischer, G., & Fütterer, D. K. (1993). The δ13C in benthic foraminiferal tests of Fontbotia wuellerstorfi (Schwager) relative to the δ13C of dissolved inorganic carbon in southern ocean deep water: implications for glacial ocean circulation models. *Paleoceanography, 8*(5), 587-610.

Mackensen, A., Hubberten, H. W., Scheele, N., & Schlitzer, R. (1996). Decoupling of δ13CΣCO 2 and phosphate in recent Weddell Sea deep and bottom water: Implications for glacial Southern Ocean paleoceanography. *Paleoceanography, 11*(2), 203-215.

Manabe, S., Stouffer, R., Spelman, M., & Bryan, K. (1991). Transient responses of a coupled ocean–atmosphere model to gradual changes of atmospheric CO2. Part I. Annual mean response. *Journal of Climate, 4*(8), 785-818.

Manabe, S., & Stouffer, R. J. (1997). Coupled ocean‐atmosphere model response to freshwater input: Comparison to Younger Dryas event. *Paleoceanography, 12*(2), 321-336.

Mann, M. E., Zhang, Z., Rutherford, S., Bradley, R. S., Hughes, M. K., Shindell, D., . . . Ni, F. (2009). Global Signatures and Dynamical Origins of the Little Ice Age and Medieval Climate Anomaly. *Science, 326*(5957), 1256-1260. doi:10.1126/science.1177303

Marshall. (2003). Trends in the Southern Annular Mode from observations and reanalyses. *Journal of Climate, 16*(24), 4134-4143.

Marshall, G. J., Stott, P. A., Turner, J., Connolley, W. M., King, J. C., & Lachlan‐Cope, T. A. (2004). Causes of exceptional atmospheric circulation changes in the Southern Hemisphere. *Geophysical Research Letters, 31*(14).

Masson, V., Vimeux, F., Jouzel, J., Morgan, V., Delmotte, M., Ciais, P., . . . Mosley-Thompson, E. (2000). Holocene climate variability in Antarctica based on 11 ice-core isotopic records. *Quaternary Research, 54*(3), 348-358.

Mayewski, P. A., Meredith, M. P., Summerhayes, C. P., Turner, J., Worby, A., Barrett, P. J., . . . Naveira Garabato, A. C. (2009). State of the Antarctic and Southern Ocean climate system. *Reviews of Geophysics, 47*(1).

Mazur, A., Wåhlin, A., & Krężel, A. (2017). An object-based SAR image iceberg detection algorithm applied to the Amundsen Sea. *Remote Sensing of Environment, 189*, 67-83.

McCrea, J. M. (1950). On the isotopic chemistry of carbonates and a paleotemperature scale. *The Journal of Chemical Physics, 18*(6), 849-857.

Meredith, M. P., Heywood, K. J., Frew, R. D., & Dennis, P. F. (1999). Formation and circulation of the water masses between the southern Indian Ocean and Antarctica: Results from ‰ 18O. *Journal of marine research, 57*(3), 449-470.

Monnin, E., Indermühle, A., Dällenbach, A., Flückiger, J., Stauffer, B., Stocker, T. F., . . . Barnola, J.-M. (2001). Atmospheric CO2 concentrations over the last glacial termination. *Science, 291*(5501), 112-114.

Moore, J. K., Abbott, M. R., & Richman, J. G. (1999). Location and dynamics of the Antarctic Polar Front from satellite sea surface temperature data. *Journal of Geophysical Research: Oceans, 104*(C2), 3059-3073.

Morris, E. M., & Vaughan, D. G. (2003). *Spatial and temporal variation of surface temperature on the Antarctic Peninsula and the limit of viability of ice shelves*: Wiley Online Library.

Moy, C. M., Dunbar, R. B., Moreno, P. I., Francois, J.-P., Villa-Martínez, R., Mucciarone, D. M., . . . Garreaud, R. D. (2008). Isotopic evidence for hydrologic change related to the westerlies in SW Patagonia, Chile, during the last millennium. *Quaternary Science Reviews, 27*(13), 1335-1349.

Mulvaney, R., Abram, N. J., Hindmarsh, R. C. A., Arrowsmith, C., Fleet, L., Triest, J., . . . Foord, S. (2012). Recent Antarctic Peninsula warming relative to Holocene climate and ice-shelf history. *Nature, 489*(7414), 141-144.

Nesje, A., & Dahl, S. O. (1993). Lateglacial and Holocene glacier fluctuations and climate variations in western Norway: a review. *Quaternary Science Reviews, 12*(4), 255-261.

Nghiem, S., Chao, Y., Neumann, G., Li, P., Perovich, D., Street, T., & Clemente‐Colon, P. (2006). Depletion of perennial sea ice in the East Arctic Ocean. *Geophysical Research Letters, 33*(17).

Niebler, H. S., Hubberten, H. W., & Gersonde, R. (1999). Oxygen isotope values of planktic foraminifera: a tool for the reconstruction of surface water stratification *Use of Proxies in Paleoceanography* (pp. 165-189): Springer.

Nielsen, S. H. H., Koç, N., & Crosta, X. (2004). Holocene climate in the Atlantic sector of the Southern Ocean: Controlled by insolation or oceanic circulation? *Geology, 32*(4), 317-320.

Nier, A. O. (1940). A mass spectrometer for routine isotope abundance measurements. *Review of Scientific Instruments, 11*(7), 212-216.

Ninnemann, U. S., Charles, C. D., & Hodell, D. A. (1999). Origin of global millennial scale climate events: Constraints from the Southern Ocean deep sea sedimentary record. *Mechanisms of Global Climate Change at Millennial Time Scales*, 99-112.

NOAA. (2017). Recent Monthly Average Mauna Loa CO2. Retrieved from https://www.esrl.noaa.gov/gmd/ccgg/trends/

Nowlin Jr, W. D., & Clifford, M. (1982). The kinematic and thermohaline zonation of the Antarctic Circumpolar Current at Drake Passage. *Journal of Marine Research, 40*, 481-507.

NSIDC. (2017). Sea Ice Index. Retrieved from http://nsidc.org/data/seaice_index/

Observatory, N. E. (2016, September 8). Crack Advances Across Antarctic Ice Shelf. Retrieved from https://earthobservatory.nasa.gov/IOTD/view.php?id=88708

Oerlemans, J. (2005). Extracting a climate signal from 169 glacier records. *Science, 308*(5722), 675-677.

Orsi, A. H., Nowlin, W. D., & Whitworth, T. (1993). On the circulation and stratification of the Weddell Gyre. *Deep Sea Research Part I: Oceanographic Research Papers, 40*(1), 169-203.

Orsi, A. H., Whitworth, T., & Nowlin, W. D. (1995). On the meridional extent and fronts of the Antarctic Circumpolar Current. *Deep Sea Research Part I: Oceanographic Research Papers, 42*(5), 641-673.

Orsi, A. J., Cornuelle, B. D., & Severinghaus, J. P. (2012). Little Ice Age cold interval in West Antarctica: evidence from borehole temperature at the West Antarctic Ice Sheet (WAIS) divide. *Geophysical Research Letters, 39*(9).

Ostlund, H. G. (1987). GEOSECS Atlantic, Pacific, and Indiean Ocean Expeditions Vol 7.

Pritchard, H., Ligtenberg, S., Fricker, H., Vaughan, D., Van den Broeke, M., & Padman, L. (2012). Antarctic ice-sheet loss driven by basal melting of ice shelves. *Nature, 484*(7395), 502-505.

Pudsey, C. J., & Howe, J. A. (2002). Mixed biosiliceous-terrigenous sedimentation under the Antarctic Circumpolar Current, Scotia Sea. *Geological Society, London, Memoirs, 22*(1), 325-336.

Rackow, T., Wesche, C., Timmermann, R., Hellmer, H. H., Juricke, S., & Jung, T. (2017). A simulation of small to giant Antarctic iceberg evolution: Differential impact on climatology estimates. *Journal of Geophysical Research: Oceans*.

Rahmstorf, S. (2002). Ocean circulation and climate during the past 120,000 years. *Nature, 419*(6903), 207-214.

Rahmstorf, S. (2006). Thermohaline Ocean Circulation. Encyclopedia of Quaternary Sciences. *Postdam Institute for Climate Impact Research, 5*.

Reimer, P. J., Bard, E., Bayliss, A., Beck, J. W., Blackwell, P. G., Ramsey, C. B., . . . Friedrich, M. (2013). IntCal13 and Marine13 radiocarbon age calibration curves 0–50,000 years cal BP. *Radiocarbon, 55*(4), 1869-1887.

Rignot, E. (2006). Changes in ice dynamics and mass balance of the Antarctic ice sheet. *Philosophical Transactions of the Royal Society of London A: Mathematical, Physical and Engineering Sciences, 364*(1844), 1637-1655.

Rignot, E., Bamber, J. L., Van Den Broeke, M. R., Davis, C., Li, Y., Van De Berg, W. J., & Van Meijgaard, E. (2008). Recent Antarctic ice mass loss from radar interferometry and regional climate modelling. *Nature geoscience, 1*(2), 106-110.

Rignot, E., Casassa, G., Gogineni, P., Krabill, W., Rivera, A. u., & Thomas, R. (2004). Accelerated ice discharge from the Antarctic Peninsula following the collapse of Larsen B ice shelf. *Geophysical Research Letters, 31*(18).

Rignot, E. J. (1998). Fast recession of a West Antarctic glacier. *Science, 281*(5376), 549-551.

Rind, D., Healy, R., Parkinson, C., & Martinson, D. (1995). The role of sea ice in 2× CO2 climate model sensitivity. Part I: the total influence of sea ice thickness and extent. *Journal of Climate, 8*(3), 449-463.

Rintoul, S., Hughes, C., & Olbers, D. (2001). The Antarctic circumpolar current system *In: Ocean Circulation and Climate/G. Siedler, J. Church and J. Gould, eds. New York: Academic Press. p.* (pp. 271-302).

Robertson, R., Visbeck, M., Gordon, A. L., & Fahrbach, E. (2002). Long-term temperature trends in the deep waters of the Weddell Sea. *Deep Sea Research Part II: Topical Studies in Oceanography, 49*(21), 4791-4806.

Rohling, E. J. (2007). Oxygen isotope composition of seawater. *Encyclopedia of quaternary science, 3*, 1748-1756.

Rohling, E. J., & Cooke, S. (1999). Stable oxygen and carbon isotopes in foraminiferal carbonate shells *Modern foraminifera* (pp. 239-258): Springer.

Rosman, K. J. R., & Taylor, P. D. P. (1998). Isotopic compositions of the elements 1997 (Technical Report). *Pure and Applied Chemistry, 70*(1), 217-235.

Ross, N., Bingham, R. G., Corr, H. F. J., Ferraccioli, F., Jordan, T. A., Le Brocq, A., . . . Siegert, M. J. (2012). Steep reverse bed slope at the grounding line of the Weddell Sea sector in West Antarctica. *Nature Geoscience, 5*(6), 393-396.

Ruddiman, W. F. (1977). Late Quaternary deposition of ice-rafted sand in the subpolar North Atlantic (lat 40 to 65 N). *Geological Society of America Bulletin, 88*(12), 1813-1827.

Ruddiman, W. F. (2008). *Earth's climate : past and future* (2nd ed. ed.). New York: W.H. Freeman.

Scambos, T., Hulbe, C., & Fahnestock, M. (2003). Climate‐induced ice shelf disintegration in the Antarctic peninsula. *Antarctic Peninsula Climate Variability: Historical and Paleoenvironmental Perspectives*, 79-92.

Schiebel, R. (2002). Planktic foraminiferal sedimentation and the marine calcite budget. *Global Biogeochemical Cycles, 16*(4).

Schiermeier, Q. (2008). Sediment cores reveal Antarctica's warmer past. *Nature, 453*(7191), 13-14.

Schlitzer, R. (2008). Ocean data view. *http://odv. awi. de*.

Schmidt, G., Bigg, G., & Rohling, E. (1999). Global seawater oxygen-18 database–v1. 21. *Online at http://data. giss. nasa. gov/o18data, online at http://data. giss. nasa. gov/o18data*.

Schmidt, G. A., Bigg, G. R., & Rohling, E. J. (1999). Global seawater oxygen-18 database.

Schoof, C. (2007). Ice sheet grounding line dynamics: Steady states, stability, and hysteresis. *Journal of Geophysical Research: Earth Surface, 112*(F3).

Schweizer, M., Pawlowski, J., Duijnstee, I. A. P., Kouwenhoven, T. J., & Van der Zwaan, G. J. (2005). Molecular phylogeny of the foraminiferal genus Uvigerina based on ribosomal DNA sequences. *Marine Micropaleontology, 57*(3), 51-67.

Shackleton, N. J. (1974). Attainment of isotopic equilibrium between ocean water and the benthonic foraminifera genus Uvigerina: isotopic changes in the ocean during the last glacial.

Shackleton, N. J., & Opdyke, N. D. (1973). Oxygen isotope and palaeomagnetic stratigraphy of equatorial Pacific core V28-238: Oxygen isotope temperatures and ice volumes on a 10 5 year and 10 6 year scale. *Quaternary research, 3*(1), 39-55.

Shepherd, A., Ivins, E. R., Geruo, A., Barletta, V. R., Bentley, M. J., Bettadpur, S., . . . Galin, N. (2012). A reconciled estimate of ice-sheet mass balance. *Science, 338*(6111), 1183-1189.

Shepherd, A., Wingham, D., Payne, T., & Skvarca, P. (2003). Larsen ice shelf has progressively thinned. *Science, 302*(5646), 856-859.

Shevenell, A., Ingalls, A., Domack, E., & Kelly, C. (2011). Holocene Southern Ocean surface temperature variability west of the Antarctic Peninsula. *Nature, 470*(7333), 250-254.

Smethie, W. M., Fine, R. A., Putzka, A., & Jones, E. P. (2000). Tracing the flow of North Atlantic Deep Water using chlorofluorocarbons. *Journal of Geophysical Research: Oceans, 105*(C6), 14297-14323.

Smith, D. A., Hofmann, E. E., Klinck, J. M., & Lascara, C. M. (1999). Hydrography and circulation of the West Antarctic Peninsula Continental Shelf. *Deep Sea Research Part I: Oceanographic Research Papers, 46*(6), 925-949. doi:http://dx.doi.org/10.1016/S0967-0637(98)00103-4

Smith, D. G., Ledbetter, M. T., & Ciesielski, P. F. (1983). Ice-rafted volcanic ash in the South Atlantic sector of the Southern Ocean during the last 100,000 years. *Marine Geology, 53*(4), 291-312.

Smith, K., Sherman, A., Shaw, T. J., Murray, A., Vernet, M., & Cefarelli, A. (2011). Carbon export associated with free-drifting icebergs in the Southern Ocean. *Deep Sea Research Part II: Topical Studies in Oceanography, 58*(11), 1485-1496.

Smith, K. L., Robison, B. H., Helly, J. J., Kaufmann, R. S., Ruhl, H. A., Shaw, T. J., . . . Vernet, M. (2007). Free-drifting icebergs: hot spots of chemical and biological enrichment in the Weddell Sea. *Science, 317*(5837), 478-482.

Smith, S. R., & Stearns, C. R. (1993). Antarctic pressure and temperature anomalies surrounding the minimum in the Southern Oscillation index. *Journal of Geophysical Research: Atmospheres, 98*(D7), 13071-13083.

Solomina, O. N., Bradley, R. S., Jomelli, V., Geirsdottir, A., Kaufman, D. S., Koch, J., . . . Nesje, A. (2016). Glacier fluctuations during the past 2000 years. *Quaternary Science Reviews, 149*, 61-90.

Speer, K., Rintoul, S. R., & Sloyan, B. (2000). The diabatic Deacon cell. *Journal of physical oceanography, 30*(12), 3212-3222.

Stammerjohn, S., Martinson, D., Smith, R., Yuan, X., & Rind, D. (2008). Trends in Antarctic annual sea ice retreat and advance and their relation to El Niño–Southern Oscillation and Southern Annular Mode variability. *Journal of Geophysical Research: Oceans, 113*(C3).

Stocker, T. F., & Wright, D. G. (1991). Rapid transitions of the ocean's deep circulation induced by changes in surface water fluxes. *Nature, 351*(6329), 729.

Stuart, K. M., & Long, D. G. (2011). Tracking large tabular icebergs using the SeaWinds Ku-band microwave scatterometer. *Deep Sea Research Part II: Topical Studies in Oceanography, 58*(11–12), 1285-1300. doi:http://dx.doi.org/10.1016/j.dsr2.2010.11.004

Stuiver, M., & Quay, P. D. (1980). Changes in atmospheric carbon-14 attributed to a variable sun. *Science, 207*(4426), 11-19.

Talley, L. (1996). Antarctic intermediate water in the South Atlantic *The South Atlantic* (pp. 219-238): Springer.

Talley, L. D. (1999). Some aspects of ocean heat transport by the shallow, intermediate and deep overturning circulations. *Mechanisms of global climate change at millennial time scales*, 1-22.

Talley, L. D. (2011). *Descriptive physical oceanography: an introduction*: Academic press.

Thompson, D. W., Solomon, S., Kushner, P. J., England, M. H., Grise, K. M., & Karoly, D. J. (2011). Signatures of the Antarctic ozone hole in Southern Hemisphere surface climate change. *Nature Geoscience, 4*(11), 741-749.

Tiedemann, R., Sarnthein, M., & Shackleton, N. J. (1994). Astronomic timescale for the Pliocene Atlantic δ18O and dust flux records of Ocean Drilling Program Site 659. *Paleoceanography, 9*(4), 619-638.

Toggweiler, J. R., Russell, J. L., & Carson, S. R. (2006). Midlatitude westerlies, atmospheric CO2, and climate change during the ice ages. *Paleoceanography, 21*(2).

Turner, J., Bindschadler, R., Convey, P., Di Prisco, G., Fahrbach, E., Gutt, J., . . . Summerhayes, C. (2009). *Antarctic climate change and the environment*.

Turner, J., & Overland, J. (2009). Contrasting climate change in the two polar regions. *Polar Research, 28*(2), 146-164.

Urey, H. C. (1947). The thermodynamic properties of isotopic substances. *Journal of the Chemical Society (Resumed)*, 562-581.

Urey, H. C. (1947). The thermodynamic properties of isotopic substances. *Journal of the Chemical Society*, 562-581.

van der Bilt, W. G. M., Bakke, J., Werner, J. P., Paasche, Ø., Rosqvist, G., & Vatle, S. S. (2017). Late Holocene glacier reconstruction reveals retreat behind present limits and two‐stage Little Ice Age on subantarctic South Georgia. *Journal of Quaternary Science*.

Vaughan, D. G., Marshall, G. J., Connolley, W. M., Parkinson, C., Mulvaney, R., Hodgson, D. A., . . . Turner, J. (2003). Recent rapid regional climate warming on the Antarctic Peninsula. *Climatic change, 60*(3), 243-274.

Waelbroeck, C., Mulitza, S., Spero, H., Dokken, T., Kiefer, T., & Cortijo, E. (2005). A global compilation of late Holocene planktonic foraminiferal δ 18 O: relationship between surface water temperature and δ 18 O. *Quaternary Science Reviews, 24*(7), 853-868.

Walker, M., & Walker, M. J. C. (2005). *Quaternary dating methods*: John Wiley and Sons.

Wanner, H., Beer, J., Bütikofer, J., Crowley, T. J., Cubasch, U., Flückiger, J., . . . Kaplan, J. O. (2008). Mid-to Late Holocene climate change: an overview. *Quaternary Science Reviews, 27*(19), 1791-1828.

Weber, M., Clark, P., Kuhn, G., Timmermann, A., Sprenk, D., Gladstone, R., . . . Chikamoto, M. (2014). Millennial-scale variability in Antarctic ice-sheet discharge during the last deglaciation. *Nature, 510*(7503), 134-138.

Weertman, J. (1974). Stability of the junction of an ice sheet and an ice shelf. *Journal of Glaciology, 13*(67), 3-11.

Wefer, G., & Berger, W. H. (1991). Isotope paleontology: growth and composition of extant calcareous species. *Marine geology, 100*(1), 207-248.

Wefer, G., Berger, W. H., Bijma, J., & Fischer, G. (1999). Clues to Ocean History: a Brief Overview of Proxies. In G. Fischer & G. Wefer (Eds.), *Use of Proxies in Paleoceanography: Examples from the South Atlantic* (pp. 1-68). Berlin, Heidelberg: Springer Berlin Heidelberg.

Whitehouse, M., Meredith, M., Rothery, P., Atkinson, A., Ward, P., & Korb, R. (2008). Rapid warming of the ocean around South Georgia, Southern Ocean, during the 20th century: forcings, characteristics and implications for lower trophic levels. *Deep Sea Research Part I: Oceanographic Research Papers, 55*(10), 1218-1228.

Williams, R. G., & Follows, M. J. (2011). *Ocean dynamics and the carbon cycle: Principles and mechanisms*: Cambridge University Press.

Yuan, X. (2004). ENSO-related impacts on Antarctic sea ice: a synthesis of phenomenon and mechanisms. *Antarctic Science, 16*(04), 415-425.

Zahn, R., Winn, K., & Sarnthein, M. (1986). Benthic foraminiferal δ13C and accumulation rates of organic carbon: Uvigerina peregrina group and Cibicidoides wuellerstorfi. *Paleoceanography, 1*(1), 27-42.

Zwally, H., Schutz, B., Abdalati, W., Abshire, J., Bentley, C., Brenner, A., . . . Harding, D. (2002). ICESat's laser measurements of polar ice, atmosphere, ocean, and land. *Journal of Geodynamics, 34*(3), 405-445.

Appendix

Credits

I credit Professor Ulysses S. Ninnemann, Helga (Kikki) F. Kleiven and Nil Irvali from the Department of Earth Science and Bjerknes Centre for Climate Research (BCCR) at the University of Bergen (UoB) for helping the data to become a reality.

Appendix A: Counts of Ice-rafted debris (IRD)

Table A.1: Iceberg rafted debris expressed as both % and grains/g

Core depth (cm)	1. IRD%	2. IRD%	Standard error of the mean ±	1. IRD grain/g	2. IRD grain/g	Standard error of the mean ±
0	1.2788	1.3942	0.0577	259.319	380.335	60.5078
0.5	0.9845			363.636		
1	0.9409			304.912		
1.5	0.8499			375.991		
2	1.4989			261.881		
2.5	0.8368			166.873		
3	1.4493			335.51		
3.5	1.1354			207.311		
4	1.5924	1.2748	0.1588	170.856	307.54	68.3423
4.5	0.6768			126.535		
5	0.9464			168.843		
5.5	0.4011			103.287		
6	1.4248			534.252		
6.5	0.6098			122.903		
7	0.7009			86.867		
7.5	1.0101			184.786		
8	3.7152	3.1414	0.2869	174.774	131.08	21.8467
8.5	1.1236			186.064		
9	1.3384			181.778		
9.5	1.2635			182.555		
10	1.2367			81.76		
10.5	1.0417			175.317		
11	0.8612			99.3395		
11.5	0.7463			156.08		
12	0.9763	1.6605	0.3421	200.737	258.091	49.6057
12.5	1.0989			107.731		
13	0.5727			103.112		
13.5	1.0681			188.391		
14	1.2422			164.452		
14.5	0.9174			121.766		
15	1.4019			100.693		
15.5	1.139			59.6709		
16	0.8989	1.996	0.2743	158.879	397.198	119.159
16.5	2.2556			485.938		
17	0.7895			123.623		
17.5	1.9284			320.647		
18	2.2388			287.778		
18.5	1.6432			285.38		

19	2.9032			393.154		
19.5	2.6415			534.487		
20	1.4523	1.1725	0.1399	273.91	136.955	68.4774
20.5	1.4754			181.956		
21	1.6807			340.414		
21.5	2.2606			188.54		
22	2.3551			274.106		
22.5	2.8986			301.561		
23	3.8462			338.711		
23.5	1.6699			144.418		
24	2.1665	1.292	0.4372	116.125	122.237	3.05591
24.5	1.94			136.787		
25	2.1384			577.219		

Appendix B: Isotope measurements of planktic foraminifera

Table B.1: N. *pachyderma* (s)*:* Oxygen isotope measurements (‰ VPDB)

Depth depth (cm)	Average $\delta^{18}O$ N. *pachyderma*	1. $\delta^{18}O$ N. *pachyderma*	2. $\delta^{18}O$ N. *pachyderma*	Standard error of the mean ±
0	3.1	3.098	3.104	0.02
0.5	3.1	3.099		
1	3.068	3.106	3.03	0.04
1.5	3.126	3	3.252	0.125
2	3.137	3.143	3.131	0.005
2.5	3.065	3.065		
3	3.241	3.241		
3.5	3.212	3.205	3.218	0.008
4	3.112	3.106	3.119	0.007
4.5	3.197	3.186	3.207	0.011
5	3.076	3.036	3.115	0.04
5.5	3.186	3.213	3.16	0.027
6	3.088	3.142	3.035	0.054
6.5	3.119	3.218	3.02	0.1
7	3.169	3.128	3.21	0.041
7.5	3.069	3.137	3.002	0.068
8	3.233	3.231	3.235	0.002
8.5	3.131	3.052	3.21	0.079
9	3.093	3.057	3.13	0.073
9.5	3.165	3.176	3.155	0.01
10	3.202	3.244	3.16	0.042
10.5	3.227	3.214	3.24	0.013
11	3.176	3.17	3.183	0.06

11.5	3.251	3.24	3.263	0.011
12	3.149	3.149		
12.5	3.151	3.12	3.182	0.016
13	3.236	3.211	3.261	0.025
13.5	3.22	3.22		
14	3.273	3.273		
14.5	3.217	3.275	3.158	0.059
15	3.154	3.154		
15.5	3.143	3.126	3.16	0.017
16	3.136	3.287	2.985	0.151
16.5	3.196	3.2	3.192	0.004
17	3.25	3.271	3.228	0.021
17.5	3.192	3.181	3.203	0.011
18	3.116	3.114	3.117	0.002
18.5	3.07	2.972	3.168	0.096
19	3.162	3.209	3.114	0.047
19.5	3.165	3.213	3.118	0.047
20	3.247	3.316	3.178	0.069
20.5	3.127	3.108	3.146	0.019
21	3.226	3.282	3.17	0.068
21.5	3.152	3.116	3.188	0.036
22	3.146	3.113	3.18	0.033
22.5	3.137	3.139	3.135	0.002
23	3.239	3.19	3.287	0.048
23.5	3.103	3.052	3.154	0.051
24	3.162	3.201	3.123	0.039
24.5	3.2	3.241	3.159	0.041
25	3.132	3.132	3.132	0

Table B.2 N. *pachyderma* (s)*:* carbon isotope measurements (‰ VPDB)

Core depth (cm)	Average $\delta^{13}C$ N. *pachyderma*	1. $\delta^{13}C$ N. *pachyderma*	2. $\delta^{13}C$ N. *pachyderma*	Standard error of the mean ±
0	1.3395	1.32	1.36	0.02
0.5	1.446	1.45		
1	1.3525	1.43	1.27	0.08
1.5	1.39	1.39	1.39	0
2	1.441	1.37	1.51	0.07
2.5	1.387	1.39		
3	1.362	1.36		
3.5	1.395	1.36	1.42	0.03
4	1.496	1.47	1.52	0.03
4.5	1.3695	1.36	1.38	0.01
5	1.376	1.29	1.46	0.09

5.5	1.3505	1.33	1.37	0.02
6	1.2635	1.22	1.3	0.04
6.5	1.343	1.44	1.25	0.09
7	1.392	1.39	1.39	0
7.5	1.311	1.36	1.26	0.05
8	1.3145	1.37	1.26	0.05
8.5	1.3685	1.38	1.36	0.01
9	1.378	1.42	1.34	0.04
9.5	1.471	1.48	1.46	0.01
10	1.44	1.44	1.44	0
10.5	1.33	1.33	1.34	0.01
11	1.4085	1.43	1.39	0.02
11.5	1.425	1.48	1.37	0.05
12.5	1.449	1.39	1.3	0.04
13	1.3465	1.43	1.49	0.03
13	1.4595	1.49		
13.5	1.51	1.51		
14	1.42	1.42		
14.5	1.36	1.36	1.35	0.01
15	1.45	1.45		
15.5	1.4045	1.42	1.39	0.02
16	1.364	1.31	1.42	0.05
16.5	1.4	1.38	1.53	0.08
17	1.4365	1.34	1.53	0.1
17.5	1.3775	1.42	1.33	0.04
18	1.2875	1.29	1.28	0.01
18.5	1.443	1.44	1.45	0
19	1.4485	1.44	1.45	0.01
19.5	1.361	1.33	1.39	0.03
20	1.3665	1.33	1.41	0.04
20.5	1.334	1.19	1.39	0.1
21	1.469	1.47	1.47	0
21.5	1.422	1.39	1.45	0.03
22	1.3475	1.24	1.45	0.1
22.5	1.3625	1.4	1.32	0.04
23	1.4405	1.39	1.49	0.05
23.5	1.491	1.52	1.47	0.03
24	1.356	1.29	1.42	0.07
24.5	1.3145	1.24	1.39	0.08
25	1.4215	1.46	1.38	0.04

Appendix C: Isotope measurements of benthic foraminifera

Table C.1 U. *peregrine:* Oxygen isotope measurements (‰ VPDB)

Core depth (cm)	Average $\delta^{18}O$ U. *peregrina*	1. $\delta^{18}O$ U.*peregrina*	2. $\delta^{18}O$ U.*peregrina*	3. $\delta^{18}O$ U.*peregrina*	4. $\delta^{18}O$ U.*peregrina*	SEM error ±
0	3.61	3.55	3.6300	3.64		0.04
0.5	3.70	3.73			3.66	0.04
1	3.68	3.96	3.5200	3.55		0.1
1.5	3.74	3.78			3.7	0.04
2	3.63	3.63				
2.5	3.45	3.79			3.1	0.35
3	3.72	3.74	3.7000			0.02
3.5	3.75	3.73	3.7900	3.59	3.89	0.09
4	3.69	3.69				
4.5	3.67	3.67				
5	3.69	3.69			3.68	0.01
5.5	3.75	3.75				
6	3.72	3.67	3.7800	3.71		0.04
6.5	3.83	3.83				
7	3.64	3.64				
7.5	3.66	3.66			3.66	0
8	3.63	3.63				
8.5	3.63	3.59	3.6000	3.73	3.6	0.04
9	3.57	3.57				
9.5	3.62	3.62				
10	3.65	3.65				
10.5	3.73	3.66	3.5800	3.95		0.15
11	3.69				3.69	
11.5	3.64	3.69			3.6	0.04
12	3.60	3.6				
12.5	3.60	3.65			3.55	0.05
13	3.68	3.68				
13.5	3.69	3.58	3.7800	3.7		0.07
14	3.78	3.78				
14.5	3.59	3.59				
15	3.68	3.78			3.59	0.09
15.5	3.68	3.68				
16	3.67	3.63	3.7600	3.67	3.71	0.07
16.5	3.66	3.61			3.71	0.05
17	3.73	3.73				
17.5	3.64	3.64				
18	3.67	3.7	3.6000	3.7		0.043
18.5	3.64	3.64				

19	3.55	3.55				
19.5	3.71	3.71			3.7	0.01
20	3.76	3.72			3.8	0.05
20.5	3.69	3.69				
21	3.71	3.71			3.72	0.001
21.5	3.61	3.51	3.5800	3.75		0.0633
22	3.66	3.81			3.51	0.15
22.5	3.68	3.63	3.8500		3.68	0.07
23	3.64	3.52	3.7400		3.66	0.08
23.5	3.73	3.8	3.6600			0.07
24	3.70	3.63	3.7600		3.7	0.03
24.5	3.73	3.77			3.7	0.03

Table C.2: U. *peregrine:* carbon isotope measurements (‰ VPDB).

Core depth (cm)	Average $\delta^{13}C$ U. *peregrina*	1. $\delta^{13}C$ U.*peregrina*	2. $\delta^{13}C$ U.*peregrina*	3. $\delta^{13}C$ U.*peregrina*	4. $\delta^{13}C$ U.*peregrina*	SEM Error ±
0	-0.14	-0.27000	-0.020000	-0.12000		0.12
0.5	0.00	0.13000			-0.127	0.13
1	0.01	0.45000	0.050000	-0.46000		0.3
1.5	-0.25	-0.25000			-0.26	0.01
2	-0.27	-0.27000				
2.5	0.28	-0.18000			0.742	0.46
3	-0.03	-0.20000	0.14000			0.17
3.5	-0.26	-0.27000	-0.30000	-0.13000	-0.342	0.08
4	-0.21	-0.21000				
4.5	-0.40	-0.40000				
5	-0.06	-0.22000			0.088	0.15
5.5	0.23	0.23000				
6	-0.08	-0.21000	0.13000	-0.17000		0.12
6.5	-0.15	-0.15000				
7	-0.13	-0.13000				
7.5	-0.46	-0.43000			-0.494	0.03
8	-0.73	-0.73000				
8.5	-0.41	-0.44000	-0.53000	-0.24000	-0.442	0.04
9	-0.38	-0.38000				
9.5	0.27	0.27000				
10	-0.29	-0.29000				
10.5	-0.10	-0.22000	-0.29000	0.21000		0.2
11	0.21				0.21	
11.5	-0.39	-0.22000			-0.558	0.17

12	-0.39	-0.39000				
12.5	-0.28	-0.040000			-0.528	0.24
13	-0.17	-0.17000				
13.5	-0.41	-0.68000	-0.39000	-0.16000		0.17
14	-0.39	-0.39000				
14.5	-0.28	-0.28000				
15	-0.43	-0.080000			-0.777	0.35
15.5	-0.50	-0.50000				
16	-0.17	-0.24000	-0.17000	-0.16000	-0.107	0.04
16.5	-0.19	-0.23000			-0.136	0.05
17	-0.30	-0.30000				
17.5	0.01	0.0100000				
18	-0.13	0.040000	-0.21000	-0.21000		0.08
18.5	-0.56	-0.56000				
19	-0.26	-0.26000				
19.5	-0.38	-0.21000			-0.546	0.17
20	0.12	-0.22000			-0.01	0.13
20.5	-0.31	-0.31000				
21	-0.28	-0.28000			-0.28	0
21.5	-0.24	-0.14000	-0.34000	-0.23000		0.07
22	-0.38	-0.42000			-0.342	0.04
22.5	-0.07	-0.060000			-0.086	0.02
23	-0.33	-0.31000	-0.42000		-0.251	0.09
23.5	-0.41	-0.72000	-0.10000			0.31
24	-0.44	-0.25000	-0.28000		-0.797	0.3
24.5	-0.16	-0.25000			-0.06	0.09

Appendix D: Statistics

Statistical analyses were carried out on the stable isotope measurements, in order to test the reliability of the data sets. Standard deviation (STD) has been calculated for a whole data set by using equation D.1. $\bar{x}$ is the mean value of all replicates in each interval, x is the value of each measurement, n is the number of replicates and k is the number of intervals with replicates. Where SD is the standard deviation, (in text STD)

$$\text{SEM} = \frac{SD}{\sqrt{n}} \qquad \text{Equation D.1}$$

$$SD = \sqrt{\frac{\sum(\bar{x}-x)^2}{n-k}} \qquad \text{Equation D.2}$$

The standard error of the mean (SEM) in each interval has been calculated by using equation D.2, where n is the number of replicates within each interval.

N. *pachyderma* (s.)

The deviation from the average of the N. *pachyderma* (s.) $\delta^{18}O$ isotopic measurements is calculated for each core depth level with replicated measurements. The deviation of the replicates from the mean value shows a normal distribution (Figure D.1), with an average deviation from the mean of ±0.048‰.

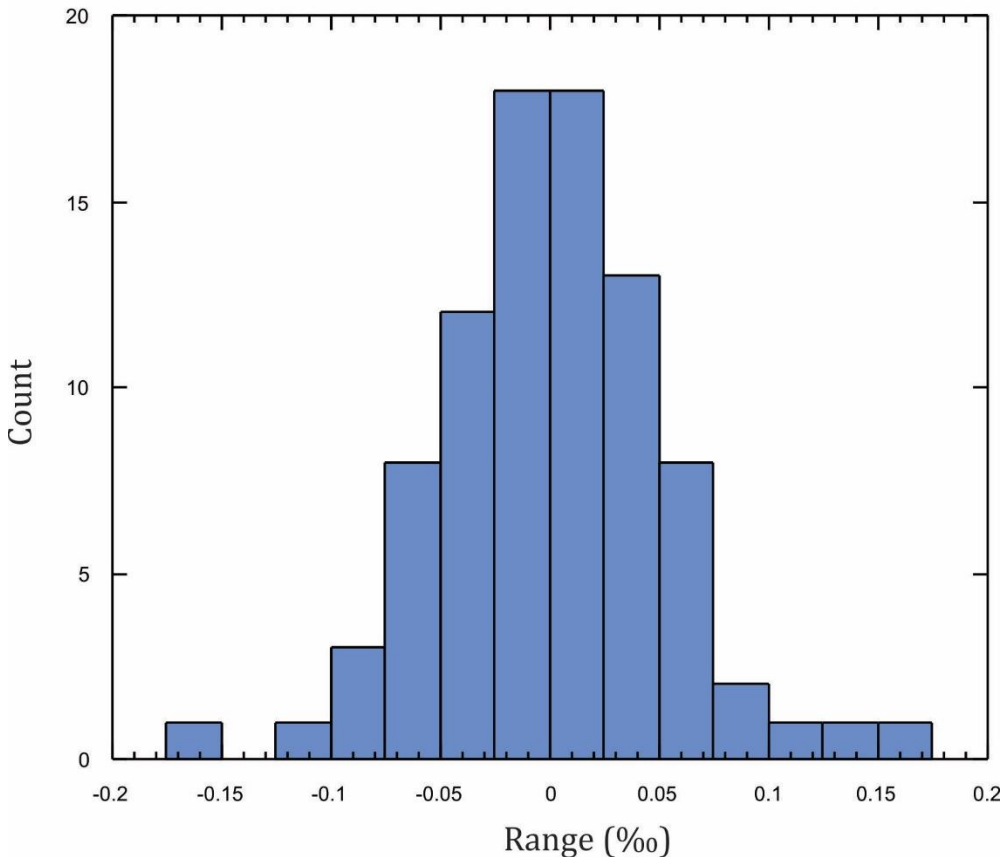

Figure D.1: Replicates deviation from the mean of the *N. pachyderma* (s.) $\delta^{18}O$ data. The y-axis shows the number of counts and the x-axis displays the range given in ‰.

N. *pachyderma* (s.)

The deviation from the average of the N. *pachyderma* (s.) $\delta^{13}C$ isotopic measurements is

calculated for each core depth level where replicated measurements were carried out. The deviation of the replicates from the mean value shows a normal distribution (Figure D.2), with an average deviation from the mean of ±0.03‰.

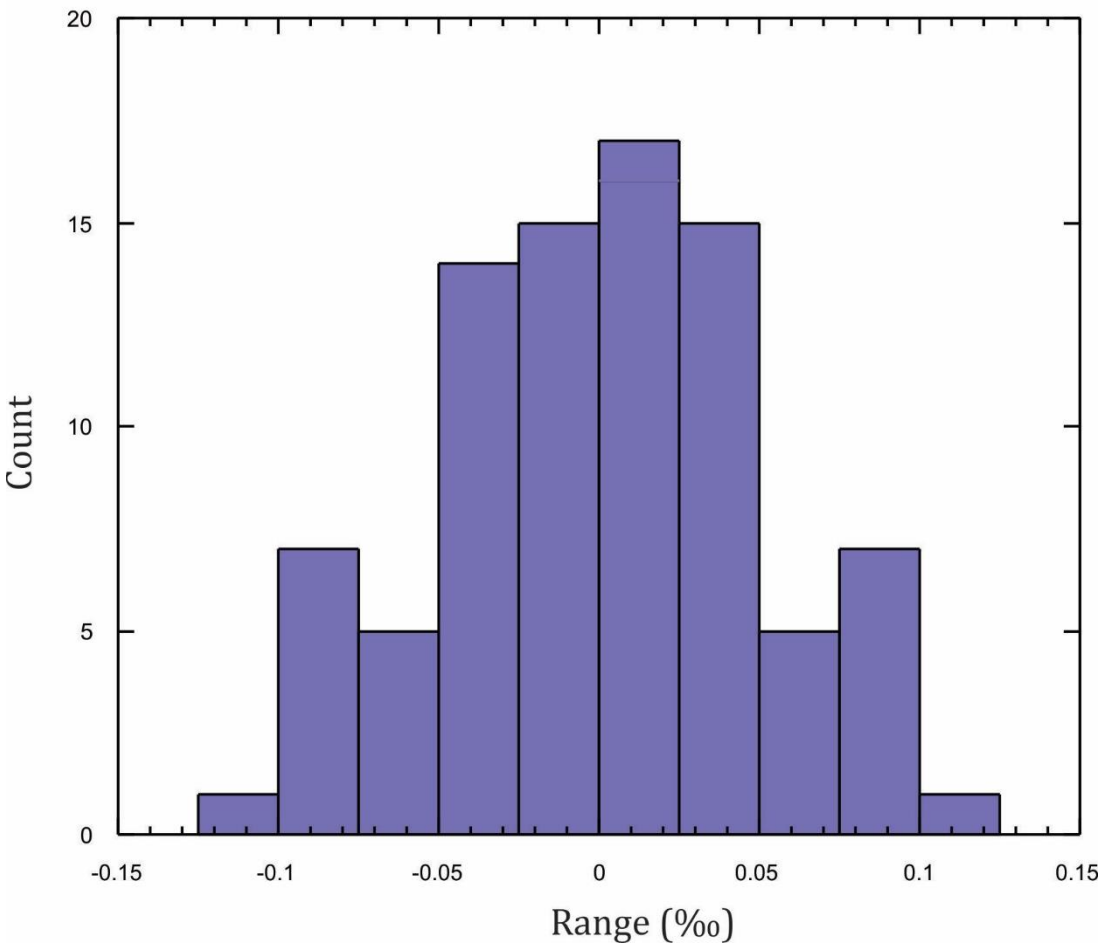

Figure D.1: Replicates deviation from the mean of the *N. pachyderma* (s.) $\delta^{13}O$ data. The x-axis displays the range given in ‰ and the y-axis shows the number of counts.

Appendix E: AMS ^{14}C dating

The result of the AMS 14C dating for core GS08-151-02MC A are presented here, as received from the Leibniz Labor für Alterbestimmung und Isotopenforschung at Christian-Albrechts University in Kiel, Germany (Table E.1). Except for KIA 46264, all samples gave enough carbon and produced sufficient ion beam during the AMS measurement. The $\delta^{13}C$ values are in the normal range for marine carbonates and insofar the results are reliable. The sample KIA 46264 gave also enough carbon. Yet, due to the bad quality of the graphite, the target produced only 77 % of the average ion current of a

1 mg sample, and the $\delta^{13}C$ value is more positive than usual. This indicates that fractionation has taken place and, thus, the result should be considered as not reliable.

Table E.1: AMS 14C dating for core GS08-151-02MC A

	Sample Name	Sample Description	Amount of C analysed (mg)	Corrected pMC†	Conventional Age	$\delta^{13}C$(‰)‡
KIA 36412	GS08 151-02MC-A; 0 cm	N. pachyderma sinistral	0.9	36.37 ±0.33	1175 ± 30 BP	0.85 ±0.12
KIA 46263	GS08 151-02MC-A; 6 cm ; 9.7 mg	N. pachyderma sinistral	0.9	81.27 ± 0.26	1665 ± 25 BP	1.50 ± 0.24
KIA 46264	*GS08 151-02MC-A; 12 cm ; 9.2 mg*	*N. pachyderma sinistral*	*0.9*	*82.00**	*1595 BP**	*7.39**
KIA 46265	GS08 151-02MC-A; 18 cm ; 9.0 mg	N. pachyderma sinistral	1.0	68.37 ± 0.23	3055 ± 30 BP	2.36 ± 0.15
KIA 36413	GS08 151-02MC-A; 24 cm	N. pachyderma sinistral	0.8	56.23 ±0.25	4625 ± 35 BP	0.66 ±0.18

Appendix F: Salinity and seawater $\delta^{18}O$ relationship in the study area

The plot (Figure F.1) show the regional mixing line between salinity and $\delta^{18}O$ in the study area, as estimated from salinity and $\delta^{18}O$ data gathered from Ostlund (1987) and Meredith et al. (1999). The full dataset consists of 25 measurements of salinity and seawater $\delta^{18}O$, collected between 45-60ºS and 20-47ºW. The slope in the plot is influenced by meltwater from the Antarctic Peninsula and thus steeper than it would be otherwise. As the site used in this study (GS08-151-02) is not significantly influenced by this, we can consider the slope to be an upper limit extreme for sensitivity to salinity changes, and although the salinity variability is low, the changes at site GS08-151-02 might be smaller than this.

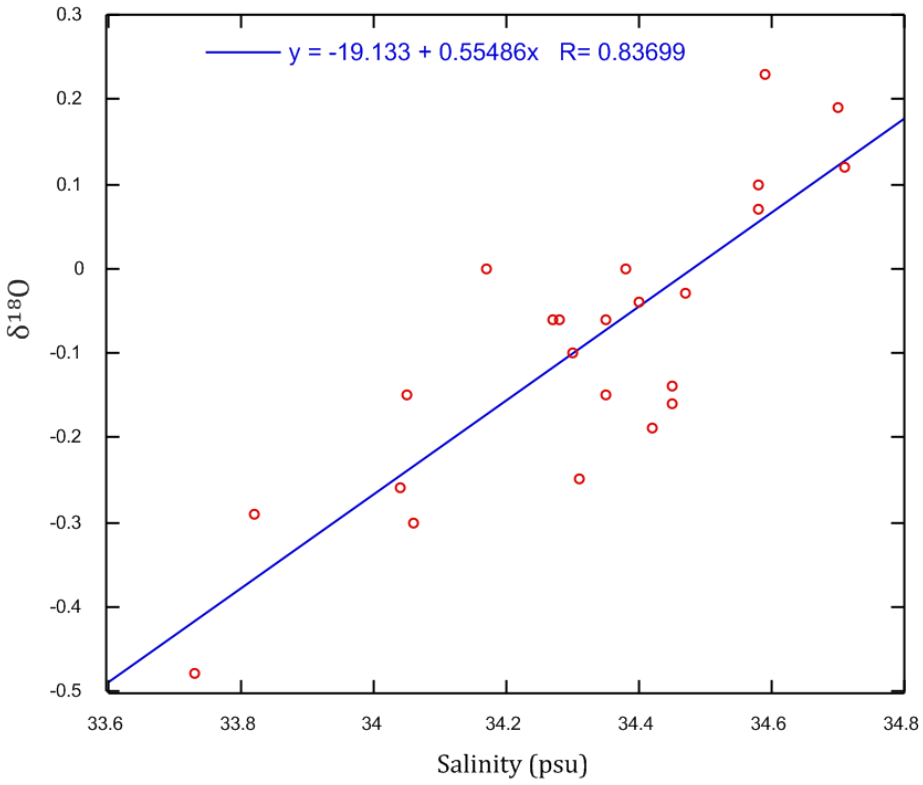

Figure F.1: Plot showing the relationship between salinity and $\delta^{18}O$ of sea water in the study area.

Appendix G: list of Abbreviations

AABW

Antarctic bottom water

ACC

Antarctic Circumpolar Current

AMS

Accelerator mass spectrometer

AP

Antarctic Peninsula

APFZ

Antarctic Polar Front Zone

CCD

Calcium carbonate compensation depth

ENSO

The El Niño Southern Oscillation

IDW

Indian deep water

IRD

Iceberg rafted debris

JRI

James Ross Island

LIA

Litle Ice Age

LGM

Last Glacial Maximum

MISI

Marine ice sheet instability

MWP

Medieval Warm Period

NADW

North Atlantic Deep Water

MS

Magnetic susceptibility

PDW

Pacific deep water

PSU

Practical salinity unit

SAM

Southern Annular Mode

STD

Standard deviation

SST

Sea surface temperature

SWW

Southern Westerly Winds

THC

Thermohaline circulation